Tracing Sveconorwegian magmatic provinces in the Nordfjord region, western Norway:

A Zircon U-Pb geochronological and petrological study

Master of Science Thesis in Geoscience

Lise Mikkelsen

Department of Earth Science

University of Bergen

December 2020

Abstract

The Western gneiss region in Norway preserves important information about the geological development of the Baltican basement. The Baltic basement reveals magmatic and metamorphic evidence for three main orogenic events: Gothian-Telemarkian orogeny (1.66-1.48 Ga), the Sveconorwegian orogeny (1.15.0.9Ga), and the Caledonian orogeny (480-405 Ma). So far, the Western Gneiss region shows mostly Gothian protolith ages and Caledonian metamorphic overprint evidence. The Sveconorwegian related rocks are primarily studied in southern Norway. We aim to trace the Sveconorwegian magmatic provinces further north, to the Nordfjord region in western Norway. In this study, new SIMS U-Pb geochronology and petrological evidence are revealed from eight samples within the Nordfjord area in the region.

Three of the samples reveal Gothian magmatic ages at ca. 1651-1625 Ma, where two of them show evidence from a Sveconorwegian metamorphic overprint at around 1040±100 Ma. The extent of this metamorphic event is unsure. Five samples show Sveconorwegian magmatic ages ranging from ca. 963-904 Ma with a younging and more felsic composition towards the west. The Sveconorwegian magmatism correlates to the ages of the Hornblende-Biotite-Granite rocks in southern Norway. Still, the samples show some differences in composition, revealing that they may have crystallized from another source. The two youngest of the Sveconorwegian protoliths show evidence of a Caledonian metamorphic overprint around 400 Ma. One of these is related to the Nordfjord UHP-HP domain, while the other correlates to the Caledonian Orogeny's exhumation.

While Gothian protolith ages and Caledonian metamorphic evidence is well studied in the WGR, this study shows that widespread magmatism related to the Sveconorwegian orogeny has also affected the area to a significant degree.

Acknowledgements

This master thesis marks the end of five and a half year with studies in geosciences at the University of Bergen. After working on this thesis, I have several people I would like to thank.

First, I would like to thank my supervisors. I want to thank my main supervisor Prof. Joachim Jacobs (UiB), for giving me the opportunity to work on this exciting master project. The guidance, feedback, and constructive comments are highly appreciated, and I am grateful that he always was available for my questions. I want to thank my co-supervisor PhD Åse Hestnes for all the help and guidance during this project. I am grateful for the help in the field, at the lab, discussions, for always being available for questions, and for the feedback. I also want to thank my other co-supervisor Prof. Deta Gasser (HVL, Sogndal) for help in the field and for good feedback on the thesis.

Second, I would like to thank Andreas Beinlich and Leif-Erik Pedersen for their help identifying difficult minerals.

Furthermore, I would like to thank all my fellow students for several good years together at the University of Bergen. A special thanks to Laura Då for working with me and encouraging me. I highly appreciate the breakfast meeting during the periods of home office.

Lastly, I want to give a big thanks to all my friend and family for their endless support and encouragements. Especially my boyfriend, Marius Overaa Eide for always cheering me on.

Lise Mikkelsen

Bergen, December 2020

Contents

Chapter 1: Introduction 1

Chapter 2: Regional Geology 4

2.1 The formation of Baltica 4

2.1.1 Fennoscandia 6

2.1.2 Crustal growth at the SW margin of Fennoscandia 6

2.1.3 The Sveconorwegian orogeny 11

2.1.4 From the Sveconorwegian to the Caledonian orogeny: Neoproterozoic to Cambrian 15

2.2 The Caledonian orogeny 16

2.3 Geology of the study area and previous work 18

2.3.1 The Western gneiss region 18

2.3.2 The study area 22

Chapter 3: Principles of zircon U-Pb geochronology 24

Chapter 4: Methods 27

4.1 Fieldwork and sampling 27

4.2 Map construction 27

4.3 Sample preparation 28

4.4 SIMS analysis 29

4.5 RAMAN and SEM analysis 29

4.6 Data processing 30

Chapter 5: Results 32

5.1 Field observations from Måløy area 32

5.1.1 Petrology 34

5.1.2 Lithological contacts and structural results 45

5.2 U-Pb geochronological and petrological characteristics 48

5.2.1 Sample VAH48, granitic augen gneiss, Honningsvåg 50

5.2.3 Sample MLM134, quartz-monzonitic augen gneiss, Måløy 55

5.2.2 VAH78, granitic augen gneiss, Hornindal 58

5.2.4 Sample VAH04, monzonitic augen gneiss, Oldedalen 61

5.2.5 Sample VAH11, monzonitic augen gneiss, Loen 65

5.2.6 Sample VAH23, granitic banded augen gneiss, Florø 67

5.2.8 Sample VAH31, muscovite-granitic gneiss, Hyen 71

5.2.7 Sample VAH44, granitic augen gneiss, Maurstad 74

Summary 78

Chapter 6: Discussion 79

6.1 Comparing the U-Pb datasets and samples to each other 79

6.1.1 Gothian magmatism 80

6.1.2 Sveconorwegian metamorphism 82

6.1.3 Sveconorwegian magmatism 82

6.1.4 Caledonian metamorphism 84

6.2 Age relations on Måløy 85

6.3 Implications for the Sveconorwegian orogeny 88

Chapter 7: Conclusion 90

Reference list: 91

Appendix 1: U-Pb geochronological results 97

Appendix 2: List of outcrops 99

Appendix 3: Map of outcrops 101

Appendix4: SEM EDS analysis 102

Chapter 1: Introduction

This thesis aims to give a better understanding of the magmatic and metamorphic evolution of the Baltican basement in western Norway, which holds evidence of three orogenic events; the Gothian-Telemarkian orogeny (1.66-1.48 Ga), the Sveconorwegian orogeny (1.15-0.9Ga), and the Caledonian orogeny (480-400 Ma). The contribution from this work gives new insight and better understanding of the magmatic and metamorphic evolution for all three orogenic events.

The evolution of the Sveconorwegian orogeny is today debated. Two main theories for the evolution dominate; the four-phase continent-continent collision model (Bingen et al., 2008c) and the accretionary orogenic evolution model (Slagstad et al., 2013,2018). These studies focused their work in southern Norway.

Further north, in the Western Gneiss Region (WGR) (Fig.1), little work has been done to map the extent of the Sveconorwegian orogeny. This region is regarded as a basement window with Telemarkian-Gothian protolith ages affected by strong Caledonian reworking, and is mostly studied based for its Caledonian development (e.g. Hacker et al., 2010; Fossen, 2010; Kylander-Clark et al., 2007; Wiest et al., 2018;). Skår and Pedersen (2003) worked in the southern WGR, were they showed how granitoid magmatism and migmatization is related by using U-Pb geochronological studies. Both Gothian-Telemarkian and Sveconorwegian protolith ages were retrieved in this study. Investigating and mapping the Sveconorwegian orogeny's extension further north, in the western-central part of the WGR, has been the main goal for this thesis.

The study area is in the Nordfjord region, in western Norway, which is a part of the WGR (Fig.1). Here, several deformed monzonitic and granitic bodies have been mapped (Bryhni, 1966; Gjeldsvik and Gleditsch, 1951; Skilbrei and Kihle, 1998), and geochronological work has been done (Corfu et al., 2014b; Corfu and Andersen, 2016; Kylander-Clark and Hacker, 2014). The U-Pb geochronology from these studies so far gave Gothian protolith ages of some larger bodies, and Gothian and Sveconorwegian protolith ages of some pegmatitic dike intrusions. Later, the Caledonian orogeny caused a reworking of the basement under up to ultra-high-pressure conditions (Hacker et al., 2010; Kylander-Clark et al.,2008).

Eight samples were collected for zircon U-Pb geochronological and petrological studies in the Nordfjord region, targeting deformed monzonitic and granitic bodies to see if they can be linked to the Sveconorwegian provinces studied further south (Fig.1). The zircon U-Pb geochronology was used to determine the magmatic and metamorphic ages of the targeted bodies. This was supported with petrological studies to determine the type of rock and potential index minerals to reveal the type of metamorphism.

Måløy, in the outer part of Nordfjord, was chosen for detailed field mapping (Fig.1). The aim was to investigate the relationships between a large monzonitic body surrounded by granitic to granodioritic basement rocks. One sample, MLM134, was taken from that monzonitic body for geochronological studies. Additionally, samples for thin sections helped study both the microscopic differences between the monzonitic body and the surrounding basement, and within the monzonitic body.

To understand and reconstruct the evolution of the Baltican shield, regional correlations are necessary. The magmatic crystallization ages and timing of metamorphic overprints provided in this study, can be related to magmatic events in the Gothian and Sveconorwegian orogenic period, and metamorphic events in the Sveconorwegian and Caledonian orogenic periods.

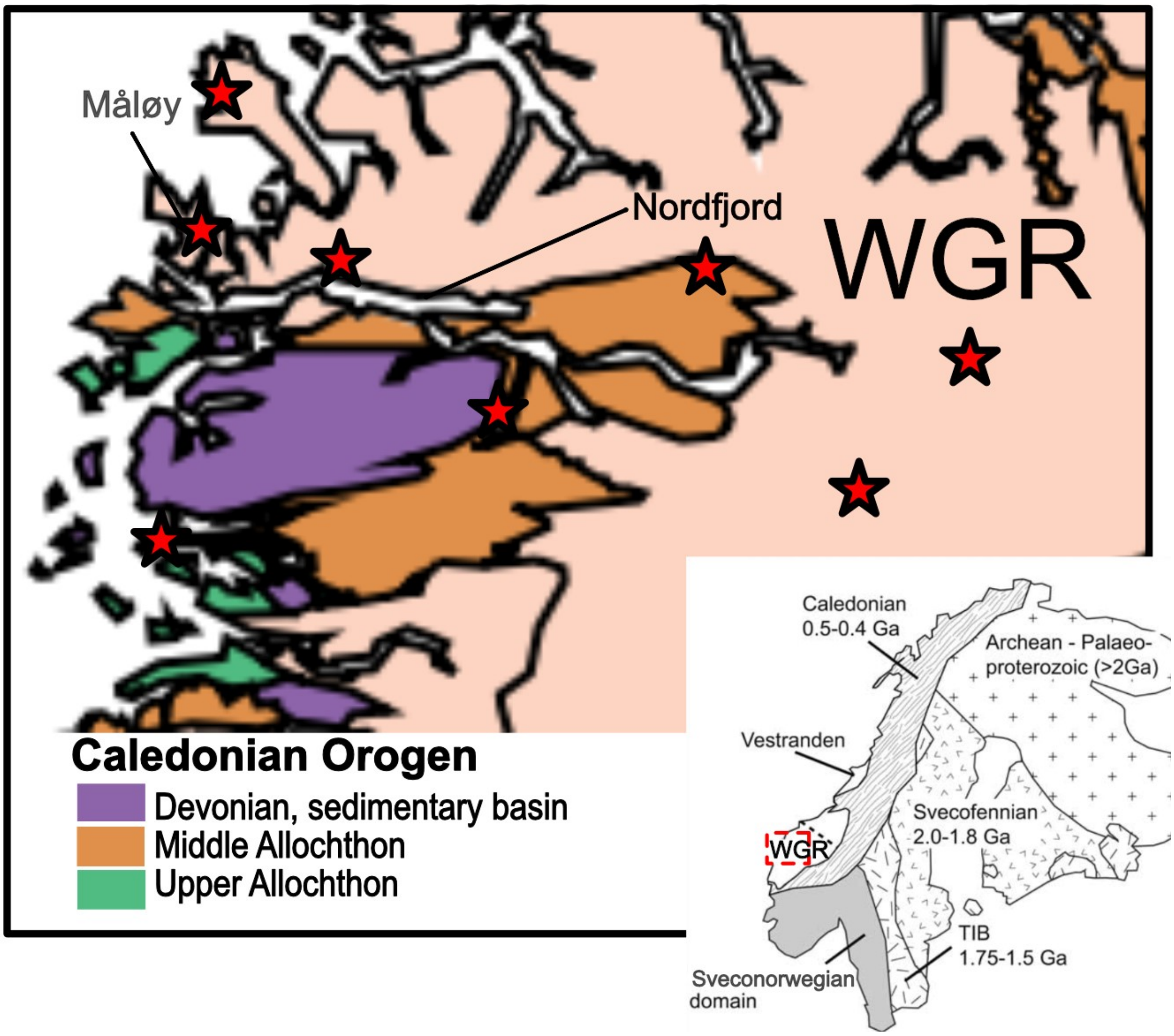

Figure 1: Map over Scandinavia showing the main geological domains. The study area is in the Nordfjord region which is part of the WGR. A zoom in the WGR shows the different Caledonian domains within the region. The stars represent the eight samples targeted for zircon U-Pb geochronology. Detailed mapping was carried out on Måløy. Modified from Slagstad et al., 2014 and Austrheim et al., 2003.

Chapter 2: Regional Geology

The geology of Norway reveals a long and complicated history. Here we find examples from Archean crust to post-glacial rebound in Neogene (Torsvik and Cocks, 2005). The oldest part of Norway's crust has been part of the formation and break-up of several supercontinents, including multiple orogenic magmatic and metamorphic episodes. In this chapter, the magmatic and metamorphic evolution of the Baltican basement will be in focus. The chapter consist of three parts. First, the formation of Baltica will be described based on four phases; 1) the development of proto-Fennoscandia, 2) the major crustal growth phases that make up the majority of Baltica, 3) the Sveconorwegian orogeny, 4) from the Sveconorwegian to the Caledonian orogeny. Second, the reworking of the Baltican basement during the development of the Caledonian orogeny will be given. Lastly, the lithological trends and previously research will be presented, first for the Western gneiss region (WGR), followed for the study area for this thesis.

2.1 The formation of Baltica

Baltica, as an independent continent, formed in the Late Neoproterozoic. As part of the Baltican shield we find some rocks from the Archean, but most of the shield was formed during the Great Proterozoic Accretionary Orogeny (1.9-0.9 Ga). During this orogeny, new crust formed on the SW part of Fennoscandia in distinct episodes (Roberts and Slagstad, 2015). The crustal formation represented in the Baltic shield, reflects the basement's accretionary history with a trend getting younger from NE to SW (Fig.2.1). In the following, the Baltic basement features will be described from NE to SW (Fig.2.1B).

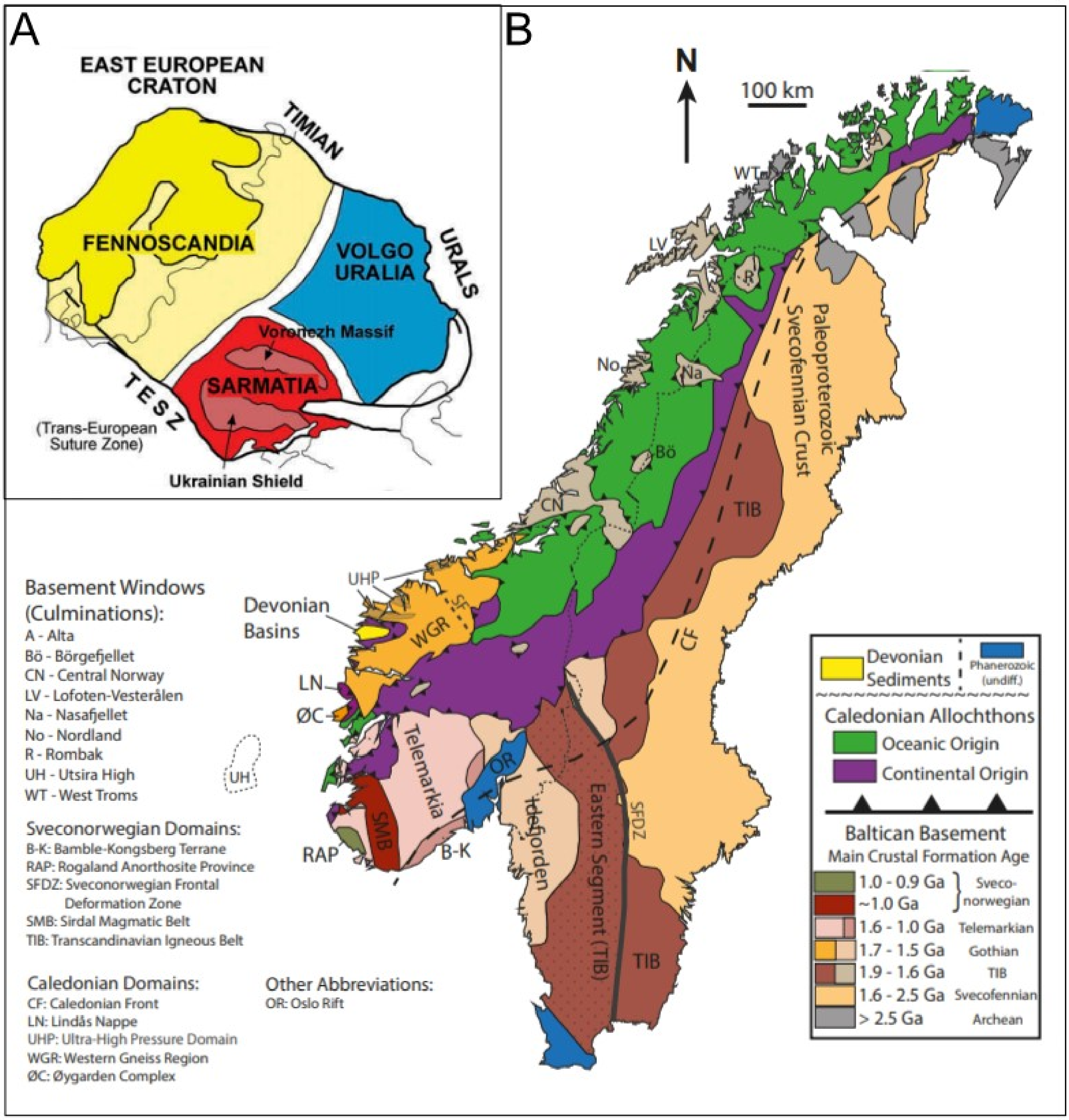

Figure 2.1: (A) Simplified geological map of the East European Craton consisting of the Fennoscandia, the Volgo-Uralia and the Sarmatia cratons that collided around 1.8 Ga. From Roberts and Slagstad, 2015 (B) A simplified geological map over Norway and Sweden divided into important Baltican domains. The crustal formation represented in the Baltic shield, reflects the basement's accretionary history with a trend getting younger from NE to SW. From Wiest,2016.

2.1.1 Fennoscandia

Fennoscandia was formed as a continental fragment during the Svecofennian orogenic period from 2.0 Ga to-1.8 Ga (Bingen et al., 2008a; Roberts and Slagstad, 2015), and represents the NW part of Baltica (Fig.2.1A). At this time, Fennoscandia consisted of Archean cratons in the NE, and Paleoproterozoic arc accretionary growth towards the SW (Bingen et al., 2008a; Åhall and Connelly, 2008). Around 1.8 Ga, Fennoscandia collided with Volgo-Uralia and Sarmatia to form the East European craton (Fig.2.1A). The Volga-Uralia and Sarmatia cratons also represent the Archean core surrounded by Paleoproterozoic domains (Bogdanova et al.,2008). Fennoscandia continued crustal growth towards the SW, and later towards the W, dominated by a long-lived subduction-related magmatic event (Åhall and Connelly, 2008).

2.1.2 Crustal growth at the SW margin of Fennoscandia

Growth of the Fennoscandian margin can be divided into three domains; The Transcandinavian Igneous Belt, the Gothian domain, and the Telemarkian domain. This growth happened on the SW margin of Fennoscandia.

The Transcandinavian Igneous Belt (TIB) (Fig.2.2) is an important transition zone on Baltica. Here, we find rocks from the Svecofennian accretionary period in the NE and the Gothian-Telemarkian accretionary period in the SW (Fig.2.1B) (Roberts and Slagstad, 2015). TIB rocks formed between 1.86-1.66 Ga. Today, TIB rocks are found on the NW part of the Norwegian coast, extending to the SE part of the Swedish coastline (Fig.2.1B) (Robert and Slagstad, 2015). This belt mainly consists of granitoids of alkali-calcic type (Hogdahl et al., 2004; Roberts and Slagstad, 2015) and are formed by episodic magmatism (Bingen and Solli, 2009). The TIB has been divided into three pulses; 1.86-1.84 Ga (TIB-0 rocks), continental arc magmatism at 1.81-1.77 Ga (TIB-1 rocks) and 1.72-1.66 (TIV-2/3 rocks). The latter resulted in large batholitic domains (Åhall and Connelly, 2008; Åhall and Larsson, 2000). Bingen et al. (2005) described an Eastern segment (Fig.2.1B) and interpreted it as a part of the TIB that was reworked during the Sveconorwegian orogeny. There is no clear transition from TIB to Gothian orogeny (Roberts and Slagstad, 2015).

The Gothian domain (Fig.2.2) represents arc magmatism ranging between 1.66-1.52 Ga and defines the Idefjorden terrane. This terrane can be seen in southern Norway and Sweden today (Fig.2.1B), (Roberts and Slagstad, 2015; Åhall and Connelly, 2008). The nature of the domain is generally considered to have formed in an overall accretionary setting, with switching in tectonics alternating between island arc- and continental arc formation, accompanied by rifting (Roberts and Slagstad, 2015). Brewer et al. (1998) suggest three distinct units based on geochemistry, together with field and age constraints. The units represent different settings in the overall subduction zone (Roberts and Slagstad, 2015). These include the Horred formation (1.66 Ga), Island arc environment; the Åmål formation (1.61 Ga), continental arc environment; the Stora Le-Marstrand (SLM) formation (1.60-1.59 Ga), oceanic arc or back-arc setting (Brewer et al. 1998). These stages were then later developed further by Åhall and Connelly (2008) into four stages:

1) The Horred formation (1.66 Ga) include Dacitic volcanic and volcaniclastic rocks of mostly intermediate composition. The rocks are affected by amphibolite facies metamorphism and show few primary features.
2) The Goteborg-Åmål belt (GAB) (1.63-1.59) combine the volcano and sedimentary rock dominating Åmål formation and the granitoid consisting Goteborg suit. The GAB rocks show a general intermediate composition and contain both gabbroic and dioritic lenses. The rocks are affected by greenschist and amphibolite facies metamorphism.
3) The granitoid Hissinger suit (1.58-1.52 Ga) is a newer discovered unit that consists mostly of intermediate granitoid intrusions as well as both mafic- and felsic bodies.
4) The Store Le-Marstrand (SLM) formation was subdivided into two units; SLM 1 rocks (1.59 Ga) and SLM 2 rocks (ca. 1.57-1.55 Ga). Both units consist of greywacke deposits with intercalated metabasalts and are affected by amphibolite facies metamorphism. The SLM 1 rocks formed in the south, while the SLM 2 rocks formed further north.

Roffeis and Corfu (2014) have correlated the Idefjorden terrane with the protolith ages of the Western Gneiss Region (WGR). The WGR represents a part of the Baltic basement that was highly reworked during the Caledonian orogeny. The Gothian rocks can be correlated to the Upper Jotun, Lindås, Dalsfjord, Upper Finse, and the Kvitenut nappes (Roffeis and Corfu, 2014). While the Eikefjord, Espedalen, Hallingskarvet, and Dyrskard nappes can be correlated to the Telemarkian domain (Roffeis and Corfu, 2014).

The Telemarkian domain (Fig.2.2) records significant continental growth between 1.52-1.48 Ga where both volcanic and plutonic complexes were formed (Bingen et al., 2005). Four sectors make up the Telemarkian domain; the Telemark sector, the Hardangervidda sector, the Suldal sector, and the Rogaland-Vest Agder sector (Bingen et al. 2005;2008b; Roberts and Slagstad, 2015). These sectors have a shared record of volcanism from this period but show both distinct lithologies and metamorphic overprint (Bingen at al 2005,2008b; Roberts and Slagstad, 2015):

1) The Telemark and Suldal sectors are affected by greenschist- to epidote-amphibolite facies metamorphism accompanied by plutonic rocks.
2) The Hardangervidda consists of gneisses with general E-W structural grains that have been affected by amphibolite-facies metamorphism.
3) The Rogaland-Vest Agder sector consists of gneisses affected by amphibolite- to granulite facies metamorphism (Bingen et al. 2008a).

The geochemistry for the magmatism occurring in the Telemarkian period is poorly constrained. One exception is the Rjukan group described by Bingen et al (2008a), and Roberts and Slagstad (2015). The Rjukan group shows a continental rifting signature accompanied by felsic volcanism and dominates the central to eastern part of the Telemarkian domain (Bingen et al. 2008a; Roberts and Slagstad 2015). Overall, the Telemarkian domain show formation and accretion of juvenile crust in an outboard arc and or continental ribbons, accompanied by continental rifting within (Roberts and Slagstad, 2015). The Telemarkian domain is considered an independent terrane regarding that no magmatic rocks older than 1.52 Ga have been positively identified (Bingen et al. 2008c). The Gothian and Telemarkian domains can be considered as one convergent margin that moved away from the craton (Roberts and Slagstad, 2015).

The Bamble-Kongsberg domain

The Bamble-Kongsberg domain can be linked to both the Gothian and Telemarkian domains (Bingen et al., 2005). The Idefjorden terrane and the Bamble-Kongsberg domain share a calk-alkaline suite at 1.57-1.52 Ga, accompanied by greywacke metasedimentary rocks. In contrast, the Telemarkian and the Bamble-Kongsberg domain share the granitic plutonism occurring between 1.52.1.46 Ga. The Bamble-Kongsberg domain is interpreted as an early Sveconorwegian collision zone between the Idefjorden terrane and the Telemarkian terrane (Bingen et al., 2005).

An interorogenic period (1.48-1.15 Ga)

The period between 1.48-1.15 Ga is traditionally considered an interorogenic period but includes both the Hallandian-Danopolonian orogeny (1.47-1.38 Ga), and a crustal growth and reworking period (1.38-1.15 Ga) (Roberts and Slagstad, 2015) (Fig.2.2). A reorganization of the subduction-zone and continental domains is reflected by the Hallandian-Danopolonian orogeny and includes the switch from E to N dipping subduction. The following crustal growth and reworking period were presumably occurring in an extensional environment. It involved intrusive suits and contemporaneous mafic underplating, as well as the formation of several sedimentary basins. "The tectonic setting during this time is inferred to be inboard of a convergent margin, indicating that the accretionary orogen was continuous from the TIB to the Sveconorwegian period" (Roberts and Slagstad, 2015). The Sveconorwegian orogeny marks the end of this interorogenic period.

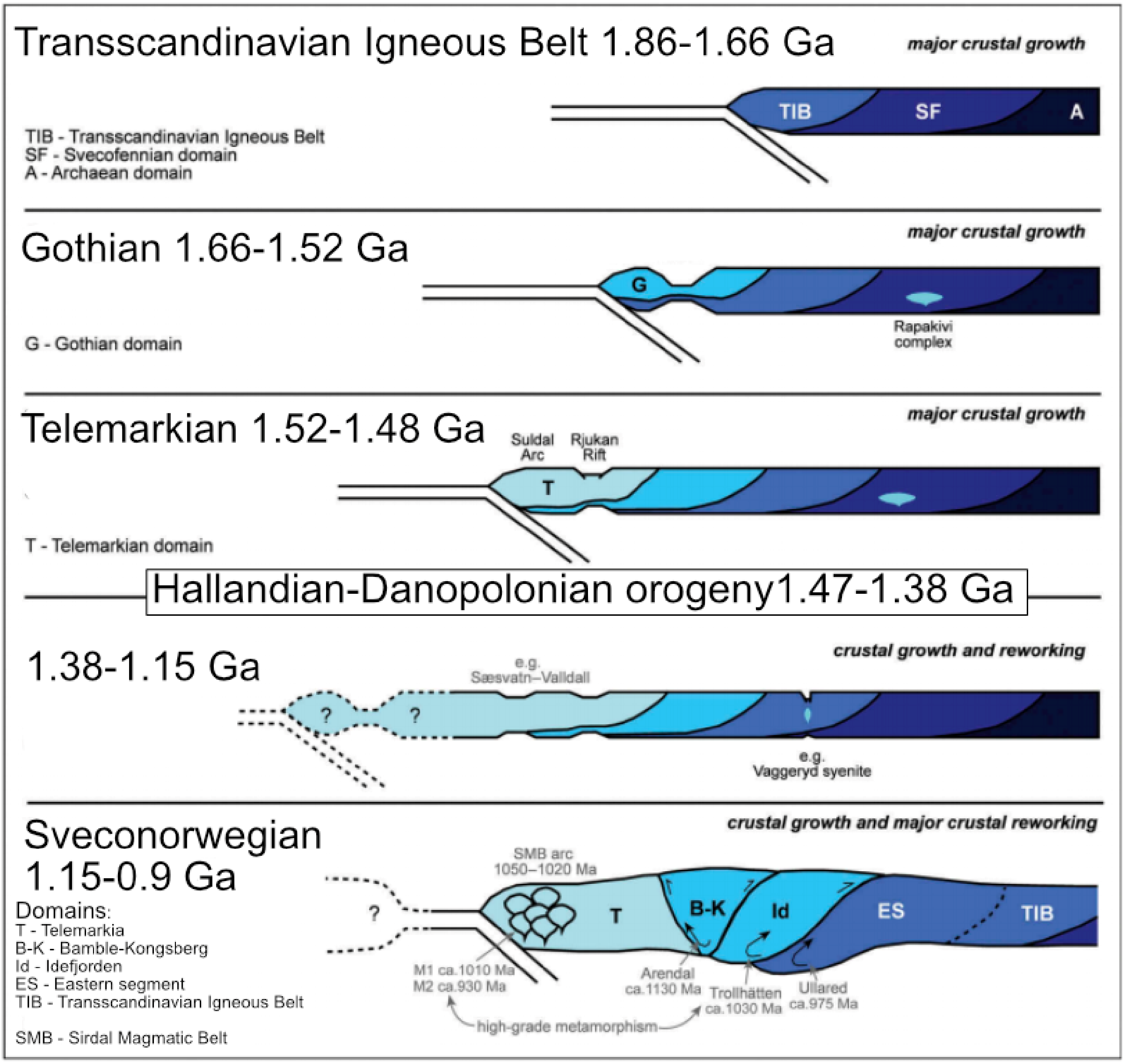

Figure 2.2: Cartoon tectonic cross-section of the major crustal growth and reworking events that occurred on the active SW margin of Fennoscandia in middle Proterozoic. Modified from Roberts and Slagstad, 2015.

2.1.3 The Sveconorwegian orogeny

The formation of the supercontinent Rodinia involved the development of the Grenvillian orogeny (1.3-1.0 Ga). This is one of the largest orogenic events through time that represents a significant time of crustal formation (e.g. Rino et al., 2008; Wiest et al., 2018). The Sveconorwegian orogeny (1.15-0.9 Ga), (Fig.2.2) overlaps in time with the Grenvillian orogeny. It has long been believed that the Sveconorwegian orogeny was an extension of the Grenvillian orogeny and a four-phase collision model was introduced (Bingen et al., 2008c). This interpretation was later challenged by Slagstad et al. (2013). Here it was suggested that the Sveconorwegian orogeny could rather be explained as a long-lived accretionary orogenic event. The debate of the Sveconorwegian orogeny and its origin is still ongoing. Below, the two theories are described in more detail.

The classical four-phase collision model

Bingen et al. (2008c) interpreted the Sveconorwegian orogeny as a continent-continent collisional orogenic event. They divided the Sveconorwegian belt into five units (Fig.2.3); the Paleoproterozoic Eastern Segment, and four Mesoproterozoic terranes: the Idefjorden, the Telemarkia, the Bamble, and the Kongsberg terrane. The units are divided by shear zones. A four-phase model is presented for the development of the Sveconorwegian orogeny (Bingen et al., 2008c):

1) During the Arendal phase (1140-1080 Ma) the Telemarkia and Idefjorden terrane collided, resulting in the Bamble and Kongsberg tectonic wedges. This event involved crustal thickening and metamorphism that peaked in granulate facies conditions.
2) The Agder phase (1050-980 Ma) represents the main continent-continent collision, involving crustal thickening in the central part of the orogen, and deformation, metamorphism, and magmatism in the Idefjorden and Telemarkian terrane. At 1050 Ma, the Idefjorden terrane experienced high pressure of amphibolite to granulite facies conditions due to underthrusting and burial. At 1035 Ma, significant crustal thickening and medium-pressure metamorphism affected the Telemarkian terrane. Between 1035-980 Ma, a peak in granulite facies metamorphism was associated with widespread syn-collisional granitic plutonism.

3) The Falkenberg phase (980-970 Ma) is seen as the transition between convergence and divergence conditions. The Eastern segments show evidence for eclogite conditions.
4) The Dalene phase (970-900 Ma) represents a gravitational collapse that marks the end of the Sveconorwegian orogeny. Voluminous post-collisional magmatism, formation of gneiss dome and core complexes, and low pressure, high-temperature metamorphism conditions occurred in this phase.

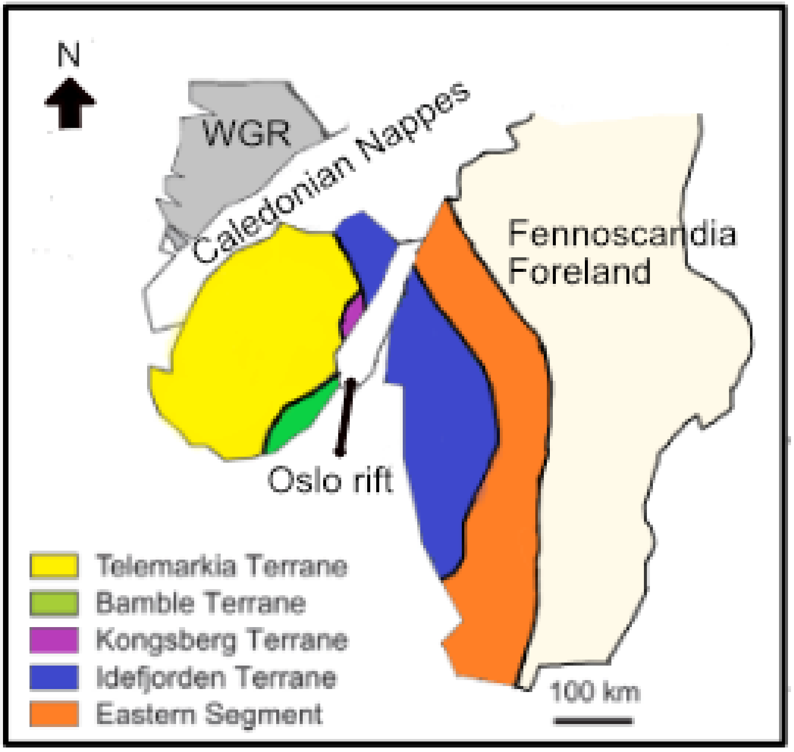

Figure 2.3: Simplified tectonic domain map over SW Scandinavia showing the Sveconorwegian belt divided into five units; the Eastern Segment, the Idefjorden terrane, the Telemarkia terrane, the Bamble terrane and the Kongsberg terrane. These units are divided by shear zones. Modified from Bingen et al., 2008c.

The accretionary model

Slagstad et al. (2013) later proposed a non-collisional, accretionary Sveconorwegian orogeny. They based their theory on voluminous subduction-related magmatism (1050-1020 Ma), absence of high-grade metamorphism between 1035-970 Ma, and a 990-920 Ma ferroan magmatism. Important for this theory is the Sirdal Magmatic Belt (SMB). The SMB was first recognized by Slagstad et al. (2013), and later studied in detail by Coint et al. (2015). The SMB is a large, commonly undeformed, and unmetamorphosed granitoid batholith that stretches as a ca. 200 km x 50 km magmatic belt (Fig.2.1B; Fig.2.4). The magmatism from this belt that occurred between 1060-1020 Ma (Fig.2.5) correlates with the timing of the main Sveconorwegian metamorphic events. One episode of amphibolite- to granulite facies conditions has been identified. Nevertheless, the preservation of igneous textures and the absence of widespread metamorphic overprint indicate preferably local metamorphism occurring after 1020 Ma instead of a regional one in the SW of Norway (Coint et al., 2015). After the SMB magmatism (1070-1010 Ma) ceased, widespread bimodal magmatism followed. This magmatism is represented by the ferroan hornblende-biotite granites (HBG, 1000-920 Ma), the Rogaland Igneous Complex (poorly constrained to 950-920 Ma) and several intervals of mafic magmatism (Fig.2.4; Fig.2.5), (Auwera et al., 2003; Auwera et al., 2008; Slagstad et al., 2018). The Sveconorwegian orogenic evolution is explained by a series of accretionary events with a repeated extension in the orogen's SW part. It includes HT-UHT metamorphism, and mafic- and felsic magmatism between 1070 and 920 Ma (Slagstad et al., 2018).

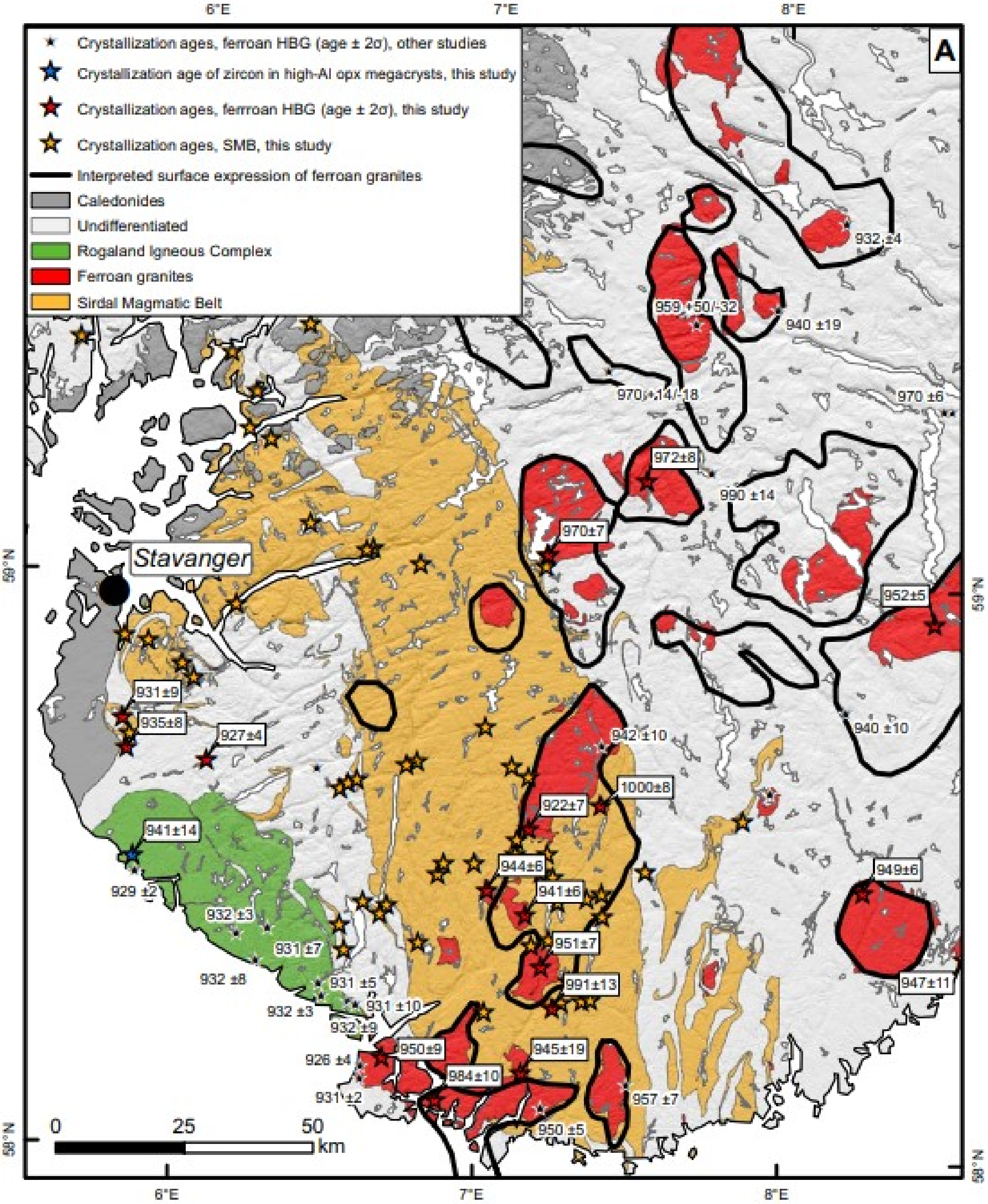

Figure 2.4: Simplified geological map by Slagstad et al., 2018. This map highlights the Sveconorwegian magmatic rocks in southern Norway divided into the Sirdal magmatic belt, the Rogaland complex and the ferroan hornblende-biotite granites.

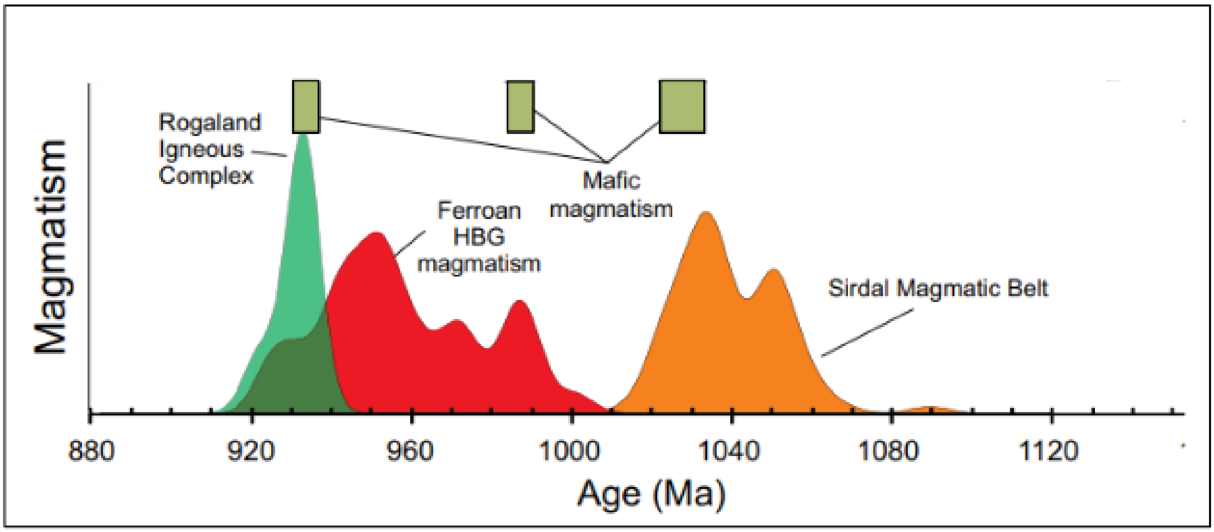

Figure 2.5: Sveconorwegian magmatism. Three intervals dominate: the Sirdal magmatic belt magmatism, the Ferroan HBG (hornblende-biotite-granite) magmatism and the Rogaland Igneous complex magmatism. They occur together with intervals of mafic magmatism. From Slagstad et al., 2018.

2.1.4 From the Sveconorwegian to the Caledonian orogeny: Neoproterozoic to Cambrian

The supercontinent Rodinia lasted for about 150 Ma after its complete assembly at ca.900 Ma (Li et al., 2008). A superplume developed underneath Rodina ca. 40 to 60 million years after the complete assembly. This resulted in widespread continental rifting between 825 and 740 Ma, together with episodic magmatic events roughly at 825 Ma, 780 Ma, and 750 Ma. Approximately between 615-570 Ma, a pulse of magmatism and rifting resulted in the Iapetus ocean's opening. At the start of the opening, Laurentia and Baltica were separated. (Li et al., 2008). The Iapetus ocean reached its largest extent around 480 Ma (Cocks and Torsvik, 2002; Torsvik and Cocks, 2005).

2.2 The Caledonian orogeny

The evolution of the Caledonian orogeny started around 480 Ma when the Iapetus ocean was at its widest (Gee et al., 2008; Wiest et al., 2018; Roberts, 2003; Torsvik and Cooks, 2005). Oblique convergence and continent-continent collision between Baltica-Avalonia and Laurentia happened during the Scandian phase, about 430-400 Ma (Corfu et al., 2014a; Gee et al., 2008; Roberts, 2003; Torsvik and Cocks, 2005; Wiest et al., 2018;). During the collision, Baltica was subducted underneath Laurentia, resulting in (U)HP eclogite facies metamorphism (Bingen et al., 2004; Corfu et al., 2014b; Hacker et al., 2010; Kylander-Clark et al., 2007).During the Devonian, an extension of the orogen occurred that resulted in thinning of the orogenic crust, formation of large sedimentary basins, and also rapid exhumation of the eclogite facies rocks in the WGR that resulted in amphibolite-facies retrogression (Corfu et al., 2014a; Fossen, 2010, Kylander-Clark et al., 2007, Hacker et al., 2010). Dominating Caledonian extensional structures formed between ca. 402-380 Ma and includes low angle thrusts and hinterland-dipping shear zones (Fossen, 2010). Traditionally the Caledonian nappes are grouped as Lower, Middle, Upper, and Uppermost Allochthons (Roberts, 2003) (Fig.2.6). The Lower and Middle are of Baltica origin, the Upper is a Iapetus-derived oceanic unit, and the Uppermost has a Laurentia origin. This terminology is still used, but detailed work in recent years have shown that the Caledonian evolution is more complicated (Corfu et al., 2014a).

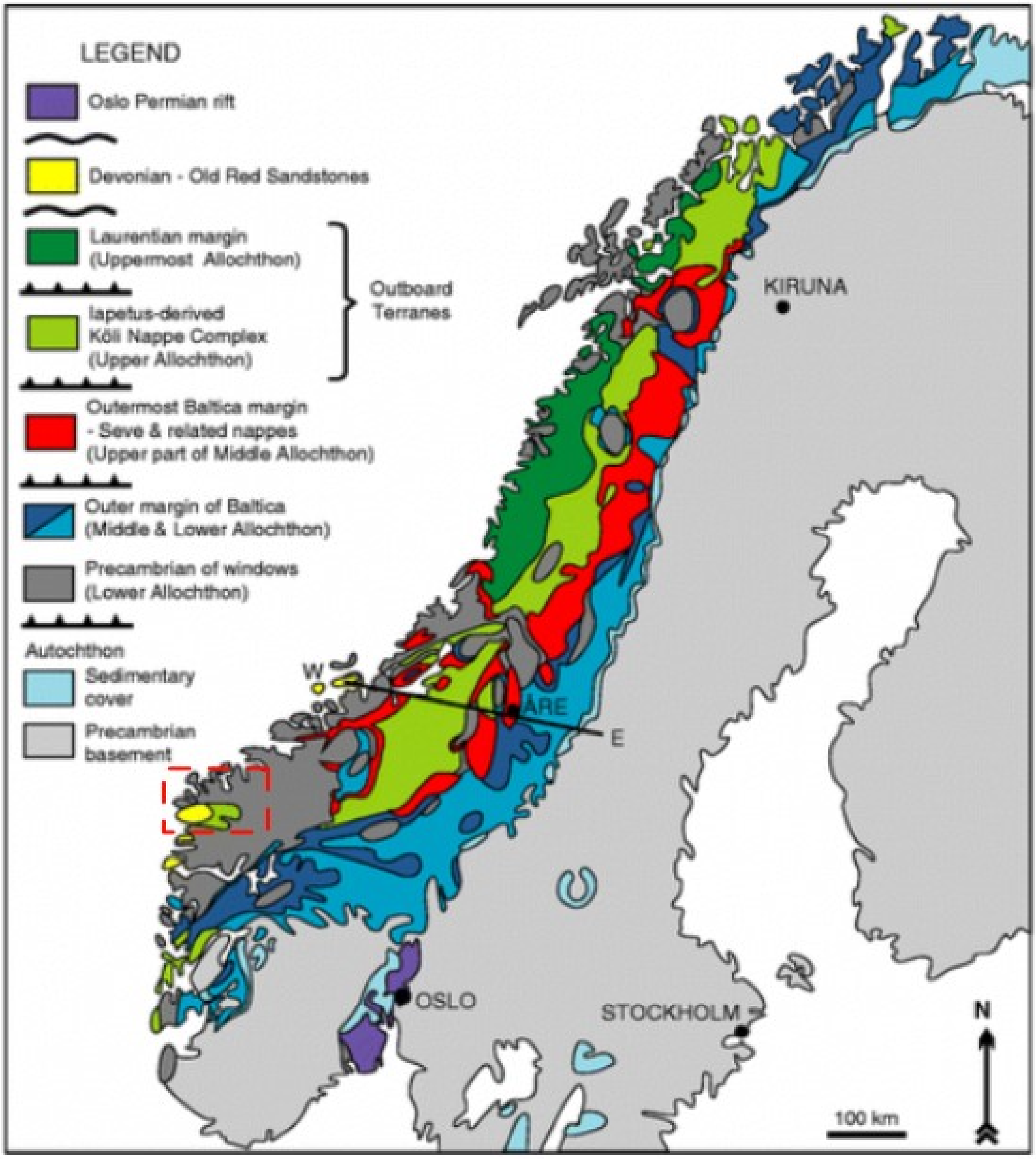

Figure 2.6: A tectonic map of the oceanic and continental allochthons placed during the Caledonian orogeny and the Precambrian basement (autochthon). The red box marks the study area for this thesis, see figure 2.10. Modified from Gee et al., 2010.

2.3 Geology of the study area and previous work

2.3.1 The Western gneiss region

The Western gneiss region (WGR) represents a more than 25 000 km^2 basement window of western Norway that stretches from Bergen to Trondheim (Austrheim et al., 2003). The basement represents a reworked part of the Fennoscandia crust partly overlain by continental and oceanic allochthons placed during the Caledonian orogeny (Austrheim et al., 2003; Corfu et al., 2014b) (Fig. 2.6; Fig.2.7). Three main tectonothermal episodes can be recognized in the WGR; two rock-forming events at 1750-1500 Ma (Gothian) and 1250-900 Ma (Sveconorwegian), and a metamorphic and tectonic overprint during the main Caledonian orogenic event (Kullerud et al., 1986; Skår et al., 1994; Skår, 2000). The three events will be described shortly in the following.

Gothian dioritic and granitic protoliths represent a significant part of the WGR (Skår, 2000; Skår and Pedersen, 2003). These orthogneisses were intruded by mafic dikes at 1470-1450 Ma and 1260-1250 Ma (Austrheim et al., 2003; Corfu et al., 2014b). Figure 2.7 gives an overview of U-Pb geochronology of the protoliths.

Previous studies show little Sveconorwegian metamorphic and magmatic findings. An amphibolite- to granulite-facies metamorphism at ca. 950 Ma (Fig.2.8) is correlated to ca. 1% of the WGR, and is more common in the continental allochthons thrusted over Baltica during the Caledonian orogeny (Hacker et al., 2010; Jolivet et al., 2005). This metamorphic event reached peak conditions of ca. 800-900 °C and 1.0 GPa due to an associated extensive plutonism (e.g. Hacker at al., 2010; Krabbendam et al., 2000; Skår and Pedersen, 2003; Wain et al., 2001). Most of these granulite-facies enclaves are found in the Nordfjord area (Bryhni, 1966; Hacker et al., 2010; Krabbendam et al., 2000; Wain et al., 2001). Low H_2O activity, coarse-grain size, and lack of deformation contribute to the local survival of these granulite-facies assemblages during the Caledonian orogeny (Hacker et al., 2010; Austrheim, 1987; Krabbendam et al., 2000). Previous work has shown that the Sveconorwegian magmatism mainly has affected the southern part of the WGR (Skår and Pedersen, 2003). Intrusion of granitic plutons, dikes and migmatites took place during this period (Tucker et al., 1990; Skår and Pedersen, 2003). The migmatites are associated with the amphibolite- to granulite-facies metamorphism (Hacker et al., 2010) (Fig.2.8).

During the Scandian phase of the Caledonian orogeny, the WGR was subducted to more than 100 km depth (Hacker at el., 2010). That resulted in (U)HP metamorphism in the WGR (Hacker et al., 2010) (Fig.2.8). The peak pressure and temperatures show an increase westward that reflects the down-to-west movement of the WGR during the subduction underneath Laurentia (Kylander-Clark et al., 2008) (Fig.2.9).

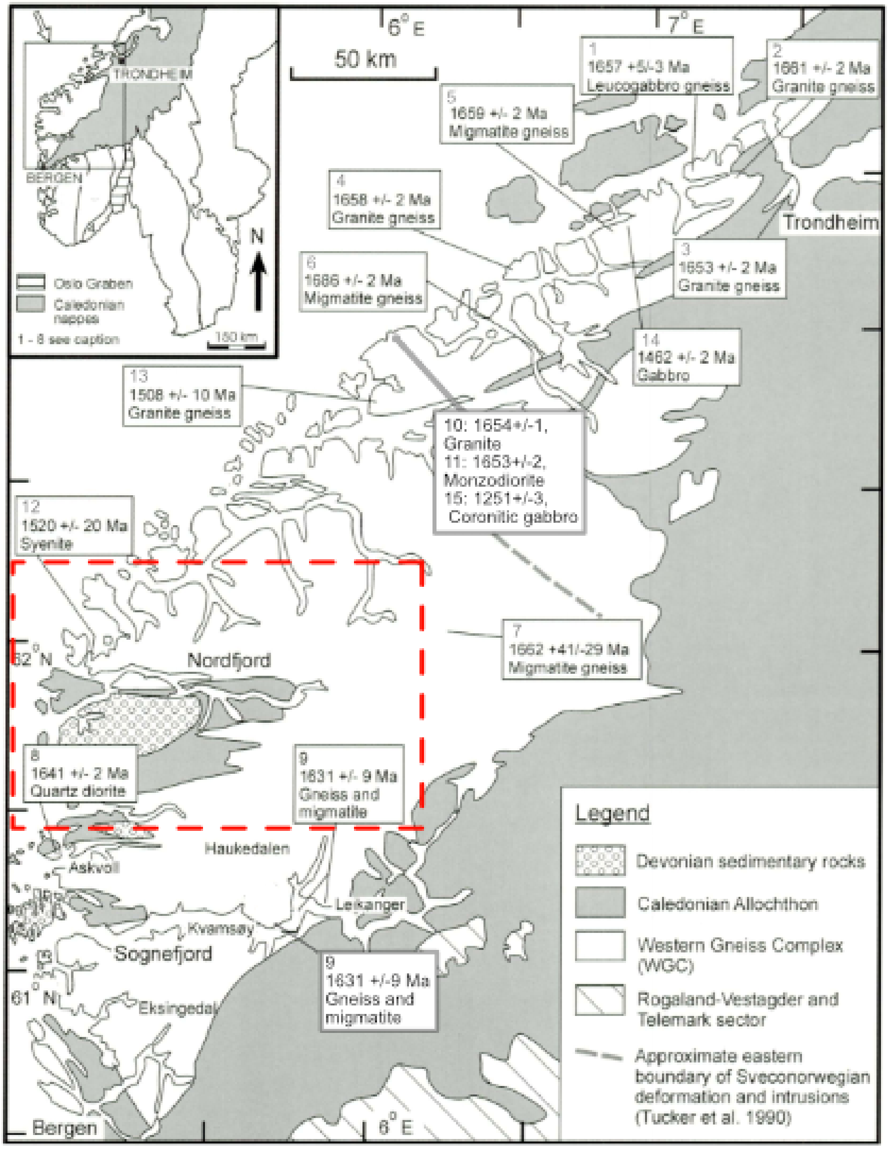

	Lithology	Age (Ma)	Locality	Reference
1	Leucogabbro gneiss	1657±5	Damvatn	a
2	Granitic gneiss	1661±2	Sagfjord	a
3	Granitic gneiss	1653±2	Ingdal	a
4	Granitic gneiss	1658±2	Frei	a
5	Migmatitic gneiss	1659±2	Åstfjord	a
6	Migmatitic gneiss	1686±2	Tingvoll	a
7	Migmatitic gneiss	1662±41	Breidalsvatn	a
8	Quartz diorite	1641±2	Atløy	b
9	Gneiss and migmatite	1631±9	Kvamsøy	c
10	Granite	1654±1	Hustad	d
11	Monzodiorite	1653±2	Hustad	d
12	Syenite	1520±20	Flaktraket	e
13	Granitic gneiss	1598±10	Molde	a
14	Coronitic gabbro	1462±2	Selsnes	a
15	Coronitic gabbro	1251±3	Hustad	d

Figure 2.7: Geological map of the Western gneiss region (WGR), together with published dating of pre Sveconorwegian rocks. The red box marks the study area for this thesis, see figure 2.10. Modified from Skår, 2000; Austrheim et al., 2003. The geochronological data are from: Tucker et al., 1990 (a); Skår et al, 1994 (b); Skår, 2000 (c); Austrheim et al., 2003 (d); Lappin et al., 1979 (e).

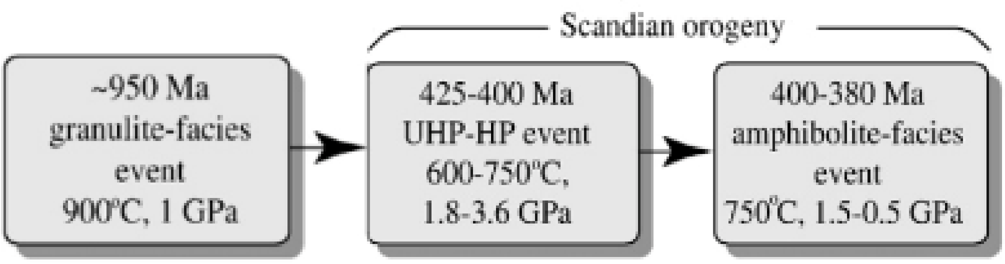

Figure 2.8: The Western gneiss region experienced several metamorphic events. Precambrian granulite-facies, Scandian UHP events and, Scandian amphibolite-facies metamorphic and deformation events. From Hacker et al., 2010.

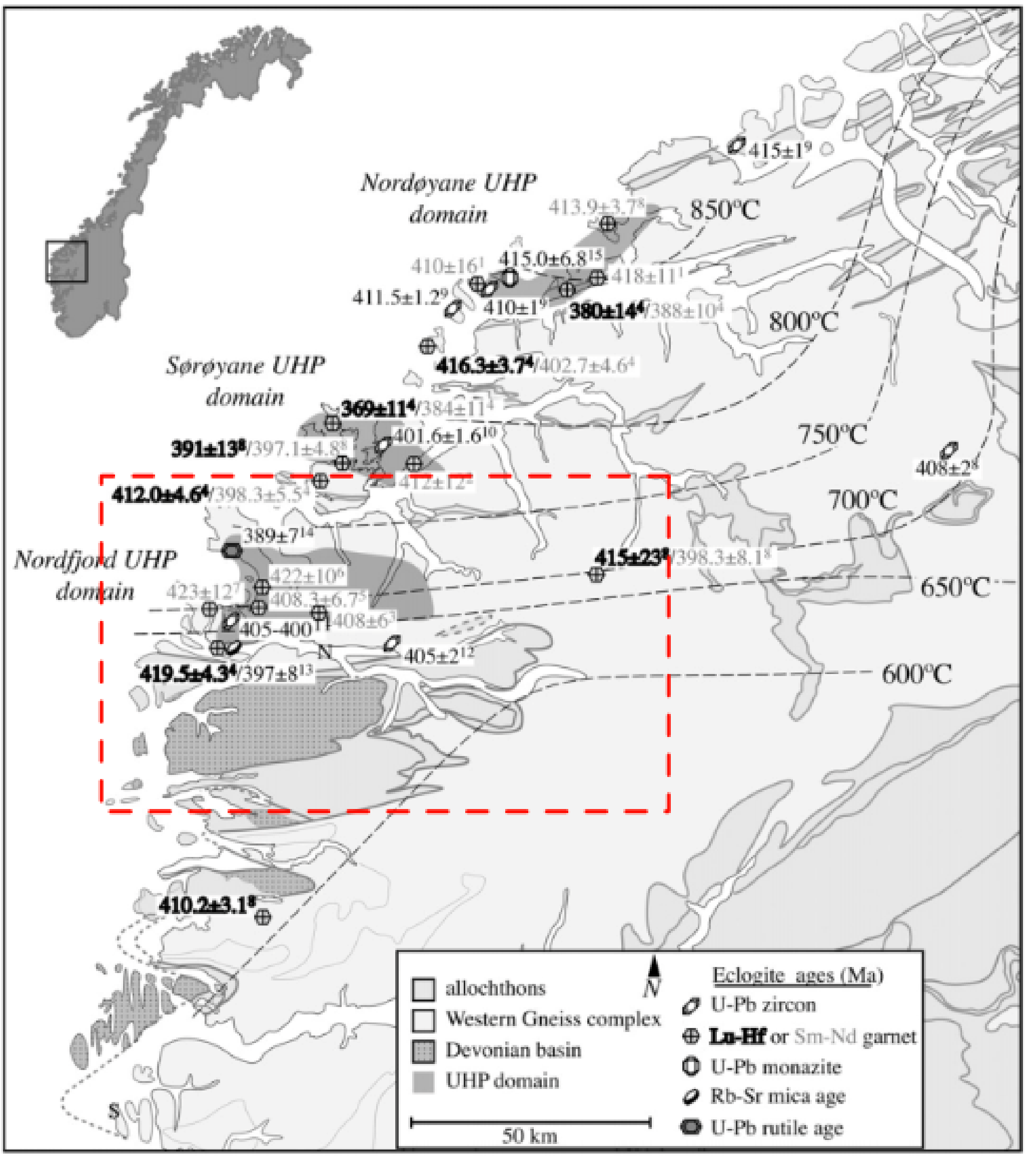

Figure 2.9: Map over the Western gneiss region showing the peak temperatures and following Eclogite ages. The red box marks the study area for this thesis (Fig.2.10). The UHP affected parts of the study area. Modified from Kylander-Clark et al., 2008.

2.3.2 The study area

The study area located around the Nordfjord (Fig.2.10), is a part of the WGR. This area has, in large parts, been mapped by Bryhni (1966), Gjeldsvik and Gleditsch (1951) and, Skilbrei and Kihle (1998). North of Nordfjord, granodioritic gneisses and some granitic augen gneisses dominate, together with mafic lenses of dunite, saxonite, and serpentinite and a few gabbroic bodies (Gjeldsvik and Gleditsch, 1951). The outer Nordfjord area is mainly dominated by banded biotite- granodioritic gneisses with interlayered local augen gneisses, feldspathic quartzite, quartz-mica-schist, and granitic gneisses overprinted by UHP metamorphism (Bryhni, 1966). The UHP zone of the outer Nordfjord (Fig.2.9) includes several eclogite and amphibolite bodies (Kylander-Clark et al., 2008). In the far western most part of the outer Nordfjord area, mangeritic rocks, syenogabbroic to monzonitic clinopyroxene-garnet-plagioclase-microperthite occur (Bryhni, 1966). A wide distribution of ultrabasite, eclogite, and anorthosite inclusions are found (Bryhni, 1966). South of Nordfjord, the Hornelen basin with Devonian sediments, covers a large area, and in the south-east part of the study area, some large monzonitic bodies are mapped (Fig.2.10) together with Caledonian nappes (Fig.2.7).

Earlier U-Pb geochronological work in the Nordfjord area comprise Austrheim and Corfu (2009), Corfu et al. (2014b), Kylander-Clark and Hacker (2014), and Corfu and Andersen (2016) (Fig.2.10). Corfu et al (2014b) studied bodies with pre- Sveconorwegian protolith ages, including the dating of the Flakraket mangerite. The Flakraket mangerite has previously been studied by Lappin et al (1979). Kylander-Clark and Hacker (2014) studied felsic dikes from the WGR that resulted in both Proterozoic dikes and Scandian igneous rocks. The Proterozoic discordant dikes represent an emplacement during the Sveconorwegian orogeny while the concordant/deformed dikes record the ca. 1650-930 Ma igneous and metamorphic activity throughout the WGR. Excepts for some Sveconorwegian dikes, there are no previous U-Pb dating of Sveconorwegian crystalline ages in the study area.

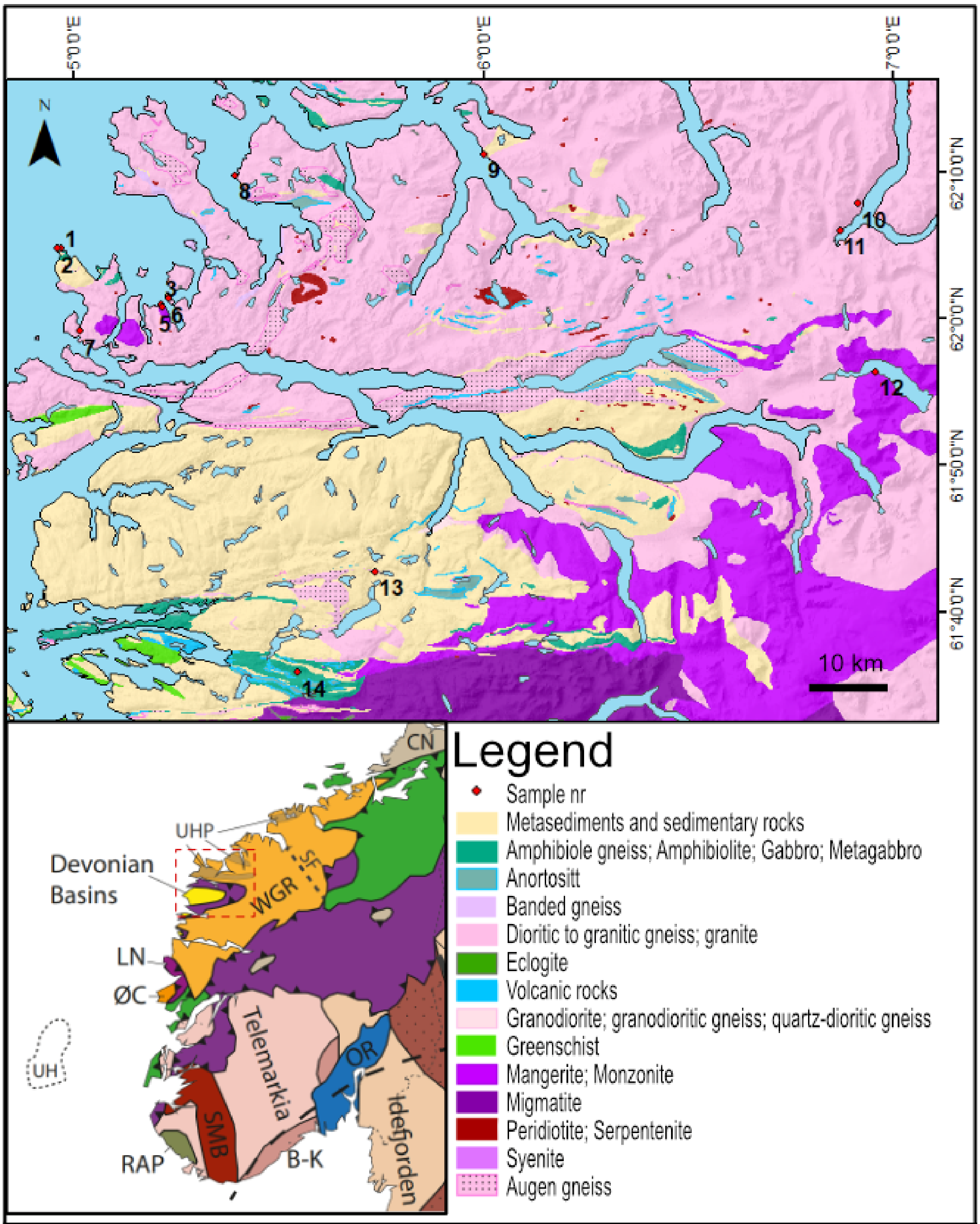

	Lithology	Upper intercept (Ma)	Lower intersept (Ma)	Locality	Reference
1	Megacrystic granite	1650		Kråkeneset Complex, Solveggen	a
2	Gabbro	1255±8	455±68	Kråkeneset Complex, Lighthouse	a
3	Quartz Monzonite	1641±5	1093±8	Flaktraket Complex	a
4	Sheared quartz monzonite	1653±7	981±29	Flaktraket Complex	a
5	Granulite	1678±9	1108±12	Flaktraket Complex	a
6	Granitic pegmatite in deformed gneiss	1581±16	962.8±9.4	Venøya	b
7	Undeformed granitic pegmatite dike		389.1±1.5	Vågsvåg	b
8	Undeformed granitic pegmatite dike	923±14		Flugevågen	b
9	Undeformed garnet-bearing aplite dike	812±81	402.3±2	Ørsta	b
10	Garnet-bearing leucosome	956±13		Hellesylt	b
11	Granitic pegmatite in gneiss	402.5±1.2		Hellesylt	b
12	Grantic pegmatite in monzonite	923±16		Djupvatnet	b
13	Amphibiolite gneiss	1514±51	990±3	Røyrvik	c
14	Metagabbro, sheared pegmatitic leucocratin vein	1507±4		Svarthumlevatnet	d

Figure: 2.10. Simplified geological map together with earlier U-Pb geochronological samples from within the study area. The Sveconorwegian ages are from felsic dikes. The geochronological data are from: Corfu et al., 2014b (a); Kylander-Clark and Hacker, 2014 (b); Corfu and Andersen, 2016 (c); Austrheim and Corfu, 2009(d). The overview map is from Wiest, 2016. For legend see figure 2.1B.

Chapter 3: Principles of zircon U-Pb geochronology

The U-Pb system is the most widely used system for dating magmatic and metamorphic rocks (Schaltegger, et al. 2015). The system consists of two isotopes of U, with close to identical chemical behavior, that decay to two Pb isotopes at different rates (Dickin, 2005). ^{238}U decay to ^{206}Pb with a half-life at 4470 million years, and ^{235}U decay to ^{207}Pb with a half-life at 707 million years (Dickin, 2005). A Concordia diagram (Fig.3) are obtained by plotting ^{206}Pb/^{238}U against ^{207}Pb/^{235}U. These are proportional to time. In a non-disturbed and closed system, the ages of these two will agree correspond, giving concordant ages. However, when the system is disturbed, the ^{206}Pb/^{238}U and ^{207}Pb/^{235}U ages will give discordant ages (Dickin, 2005). An example for such a disturbance can be a metamorphic event resulting in lead loss or uranium loss (not as common).

These two U-Pb isotope chains, that decay at different rates gives the system its geochronological power, making it so that the correct age information can be obtained even from a disturbed system. Where the discordia line intersects the Concordia curve, we get the information of the sample ages. The upper intersection represents the time of formation of the mineral. The lower intersection represents the age of the thermal event that resulted in the disturbed system and lead loss (or uranium loss) of the mineral. This means that the formation age of the mineral can be obtained even in a disturbed system, and also the timing of the thermal event that disturbed the system can be obtained.

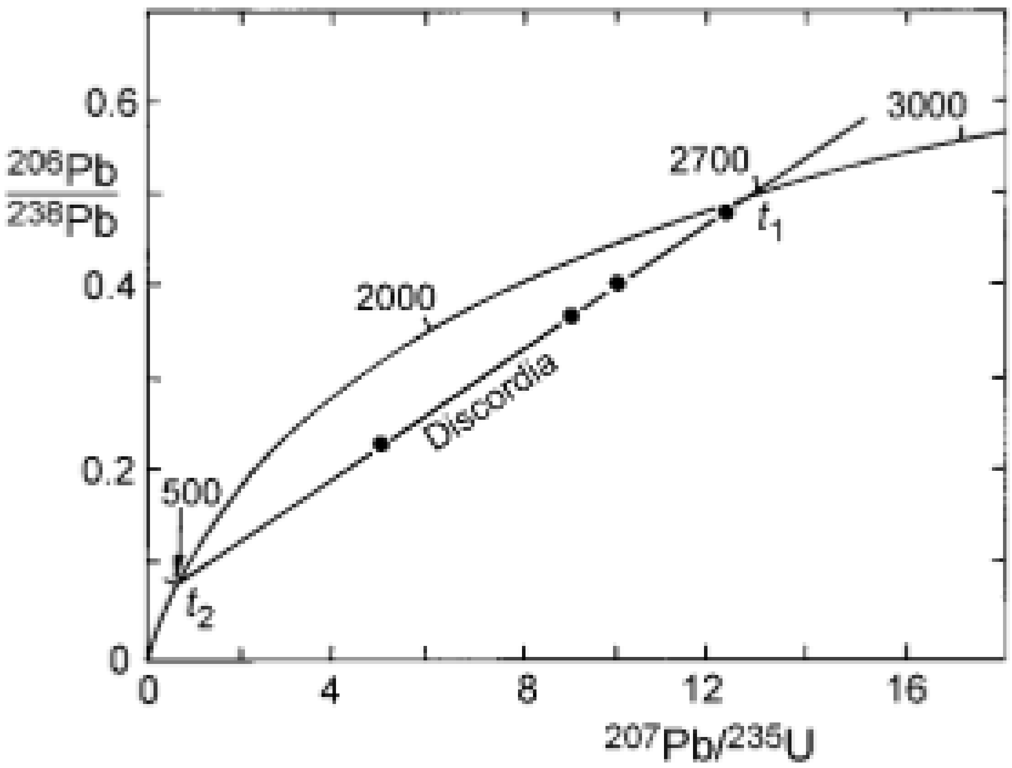

Figure 3: Figure shows a Concordia diagram with the Concordia curve and Discordia line. T1 (700 ma) represents the magmatic age of a mineral while t2 (500 ma) represent the metamorphic age. The Discordia line is here due to Pb loss. If the disturbed system has led to uranium loss, the Discordia line would be plotted closer to the top left corner compared to the Concordia curve (Dickin, 2005).

Zircon as a U-Pb chronometer

Zircon is the principal material used in U-Pb dating for several reasons:

1) At the time of formation, zircon strongly incorporates uranium, while rejecting lead (Dickin, 2005). This means that there will be no initial or common lead when zircon first start to crystallize and that the lead represented in zircon is only radiogenic lead (Dickin, 2005), making zircon the "perfect" clock.
2) Zircon is the oldest mineral on earth due to its hardness and chemically resistant, doing it possible to find the mineral in the oldest rocks.
3) The closure temperature of U-Pb diffusion in zircon is above 900 $°C$ (Schoene, et al. 2017). This is higher than other minerals such as monazite (above 800 $°C$) and titanite (600 to 800 $°C$) which also are U-Pb chronometers (Schoene et al., 2017) One U-Pb chronometer with the same closure temperature as zircon is Baddeleyite (Schoene et al., 2017), but this is a rare zirconium oxide mineral and therefore not often used.

To understand the dates obtained for U-Pb geochronology we need information about the petrographic characteristics of zircon. Zircons show a large variety in shapes and internal textures, which reflects magmatic and metamorphic events of crystallization and recrystallization (Corfu et al., 2003). The more complex zircons can give information about more than just the magmatic crystallization ages. During a thermal event, zircons may be overgrown by new zircon crystal instead of recrystallizing (Dickin, 2005), leading a zircon to have multiple zones of different ages. Commonly, the core represents the magmatic crystallization age while the rime of overgrowth represents the thermal event/metamorphic crystallization age.

Chapter 4: Methods

4.1 Fieldwork and sampling

The data gathering for this thesis was carried out during three weeks in June and July, 2019, together with the PhD project by Åse Hestnes. During the first two weeks the focus of the fieldwork was to collect samples from the Nordfjord area for U-Pb geochronology.

Detailed geological fieldwork was carried out during the last four days of the fieldwork, at Måløy, located at Vågsvåg, northwest of Nordfjord. The field area was revisited over two days in July 2020 for more mapping. Standard mapping techniques were used, including colour pencils, black and white topographic map, geological hammer, geological compass, (Fieldmove clino) and "Norgeskart friluftliv" app for coordinate extraction. A total of 167 outcrops were mapped, also collecting structural measurements for planar fabrics and linear fabrics.

A total of eight samples from the Nordfjord area were selected for SIMS, zircon U-Pb geochronology. Sample VAH04 and VAH11 were collected during a previous fieldwork during the fall of 2018 related to the PhD project by Åse Hestnes. All eight samples were crushed to pebbles size in the field by geological hammer and sledge hammer. This crushing was done on surface of the same lithology as the collected sample to avoid contamination.

Thin sections were made of all eight samples used for geochronological studies. In addition, thin sections were made of seven samples from Måløy to better study the petrological, and microtextural differences in the mapping area. The thin sections were prepared at the University of Bergen by Andreas Viken.

4.2 Map construction

ArcMap 10.7.1 was used to construct an overview map of the study area with sample localities and a map of Måløy. The lithological background map is based on data from NGU.

4.3 Sample preparation

Mineral separation

Further preparation of the samples was carried out at the University of Bergen together with Åse Hestnes. The eight samples were crushed to < 315 µm grainsize with a Fritch Pulverisette 13 discmill (Fig.4A). Sieves were used to remove > 315 µm particles.

To separate the zircons from the other minerals, we depend on the density differences and magnetic properties. Zircon is a relatively heavy mineral of 4.6-4.8 g/cm^3 and non-magnetic (Guo et al., 2012). First, the Holman-Wilfley shaking table (Fig.4B) was used to do a first order separation of the <315 µm material. The heavier fraction was dried before a hand magnet was used to remove the strong ferromagnetic minerals. Thereafter a magnetic separation was carried out with a Franz Ferromagnetic separator (Fig.4C). The separator was used to separate the weakly ferromagnetic minerals from the stronger ferromagnetic mineral. The material was run through the Franz Ferromagnetic separator two times with 0.3 V and with 0.6 V, and a dip on 15° and 17°. The non-magnetic fraction of the samples were further separated by two different types of heavy liquids. The first liquid, LST (low toxicity sodium heterpolytungstates) with a 2.9 g/ mL density, was used to separate quartz and feldspar from the heavier minerals. The second liquid, DIM (Dilodomethane) with a 3.3 g/mL density was used to separate the titanite and apatite from the zircons. The samples were then rinsed with acetone and dried. Åse Hestnes did the separation with the Franz Ferromagnetic separator for most of the samples. The heavy liquid separation was carried out by Åse Hestnes for all the samples.

Three of the samples (Vah23, VAH78 and VAH44) contained a high amount of pyrite. To remove the pyrite, the sample was put in a mix of 90 ml HLC and 30 ml of HNO_3 that was heated up to ca. 100 °C to dissolve the pyrite. The samples were then put in a 12-15 mikron filter and dried.

In the end, the samples VAH44, VAH31 and VAH04 still had a lot of unwanted minerals. To remove more of the unwanted minerals, they were put through the Franz Ferromagnetic separator a second time with 1.0 V.

Mount preparation

Zircons from all eight samples were placed on the same mount (Fig.4D). An average of 50-60 zircons grains were picked for each sample and placed on the mount by using a tweezer. This process was done using a Zeiss Microscope. After picking, the mount was sent to the Nordsim laboratory in Stockholm for further mount preparations. At Nordsim, standard material was added, and the mount was polished.

Zircon imaging

When the mount preparation executed at the Nordsim facility was finished, a gold-coated mount was sent back to the University of Bergen. Three different images of the zircons were taken. First, transmitted and reflected light images were taken to reveal fractures and inclusions in the zircons grains. Then cathodoluminescence (CL) images were taken to see the texture within the zircon grains. For the CL-imaging a Zeiss supra 55VP scanning electron microscope (SEM) (Fig.4D) was used. These pictures together were used together to select individual spots for analysis. Ca 20 spots were selected per sample for dating analysis. The mount and the pictures with the marked spots for analysis were then sent back to the Nordsim facility to complete SIMS analysis.

4.4 SIMS analysis

At Nordsim facility in Stockholm a Cameca IMS 1280 instrument was used to perform U-Th-Pb analysis of the zircons. The geochronological analysis follows the protocol described by Whitehouse et al. (1999) and Whitehouse and Kamber (2005). SIMS analysis of the mount was done by Cheng-Cheng Wang. The SIMS data is reported in appendix 1.

4.5 RAMAN and SEM analysis

In order to get more information to determine those few minerals that showed unusual properties in the optical microscope, Raman spectroscopy and a Scanning Electron microscope (SEM) at the University of Bergen were used. The Raman system used is a Horiba LabRam. Spectra “fingerprints” of the chemical structure is collected by the Raman. These fingerprints are than matched with known material in the ruff database. The SEM microscope used at UIB is a Zeiss supra 55VP field emission machine (Fig.4D). Before, the thin sections were coated with a thin layer of carbon (Fig.4F). The SEM was used to collect images by using backscattered electrons (BSE) and EDS analysis to get element analysis on the wanted spots (Fig.4G).

4.6 Data processing

To process the SIMS data, Isoplot version 4.15 was used to calculate both Concordia and Discordia ages. The Isoplot manual from Ludwig (2012) was used as a guide. The data were plotted in Terra-Wasserburg Concordia diagram. Both common 204Pb- corrected and uncorrected were used. The Concordia ages were plotted with 1σ error ellipses, and the presented ages were plotted with 2σ ellipses. The mean square of weighted deviated (MSWD) and the probability values used are of both concordance and equivalence. When possible, mean ages for the concordant ages were calculated.

For the Raman analysis the data processing was done by using Crystal Sleuth software. Here the "fingerprints" from the unknown mineral were compared with "fingerprints" from known material in the ruff database to find the best-estimated match to help identify the unknown mineral.

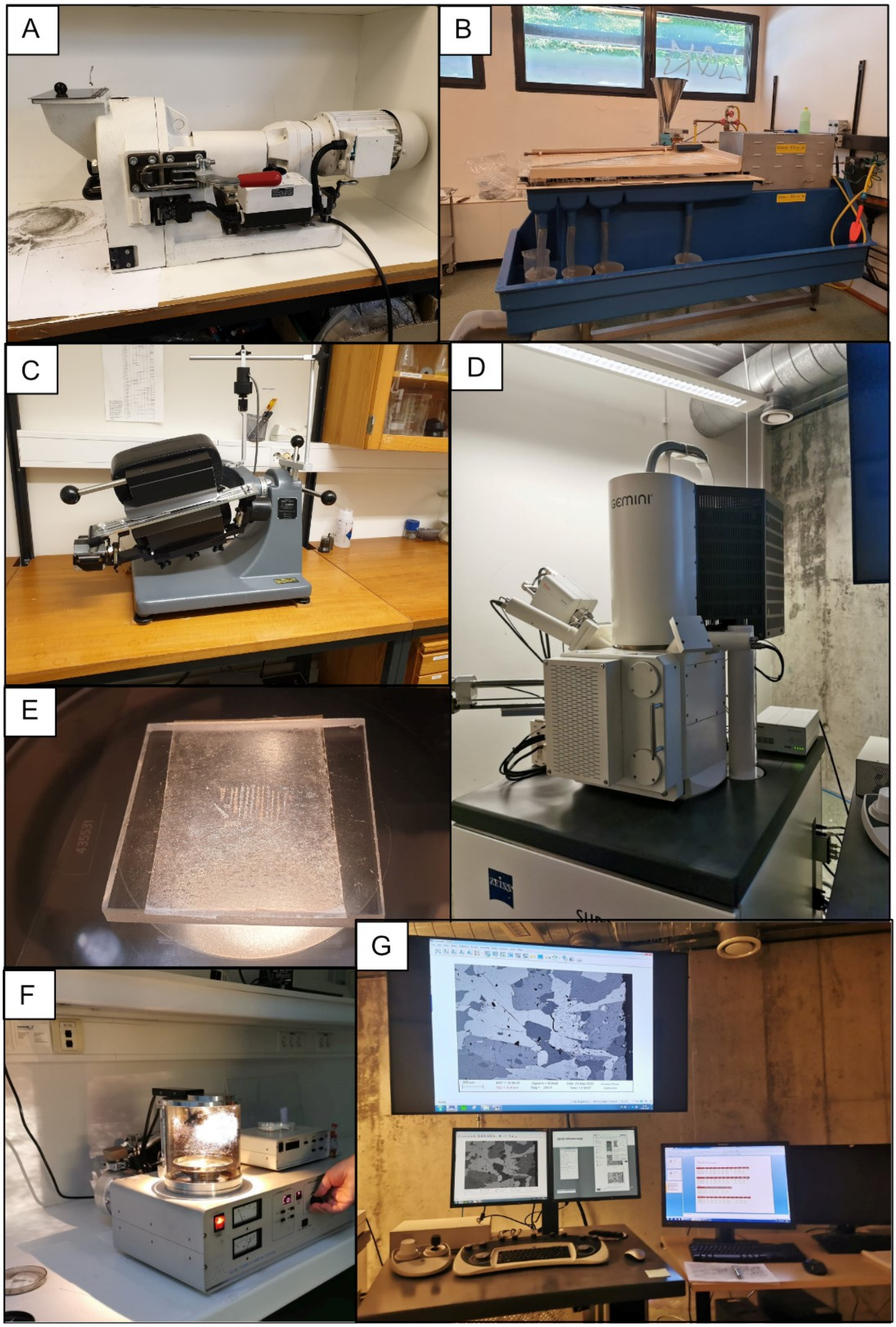

Figure 4: (A) Fritch Pulverisett 13 discmill. (B) Holman-Wifley shaking table. (C) Franz Ferromagnetic separator. (D) Zeiss Supra 55VP Scanning Electron Microscope. This was used for both CL-imaging and SEM analysis to extract EDS data. (F) Here the thins sections are coated with carbon. (G) BSE picture and EDS data from one of the samples analysed.

Chapter 5: Results

This chapter is divided into two main parts. The first part describes the field results from Måløy, while the second part presents the geochronological data and petrology for the eight collected samples in the Nordfjord region.

5.1 Field observations from Måløy area

The lithologies observed in the Måløy area include monzonitic gneiss, granitic to granodioritic gneiss, metagabbro, dioritic dikes, eclogite, amphibolite and feldspar lenses and dikes. One major garnet-bearing monzonitic body dominates the centre of the field area and is surrounded by a granitic to granodioritic gneiss. A geological map is shown in Fig.5.1.1. These are a result of detailed field mapping. Appendix 2 and 3 show a list of outcrops and a map of localities.

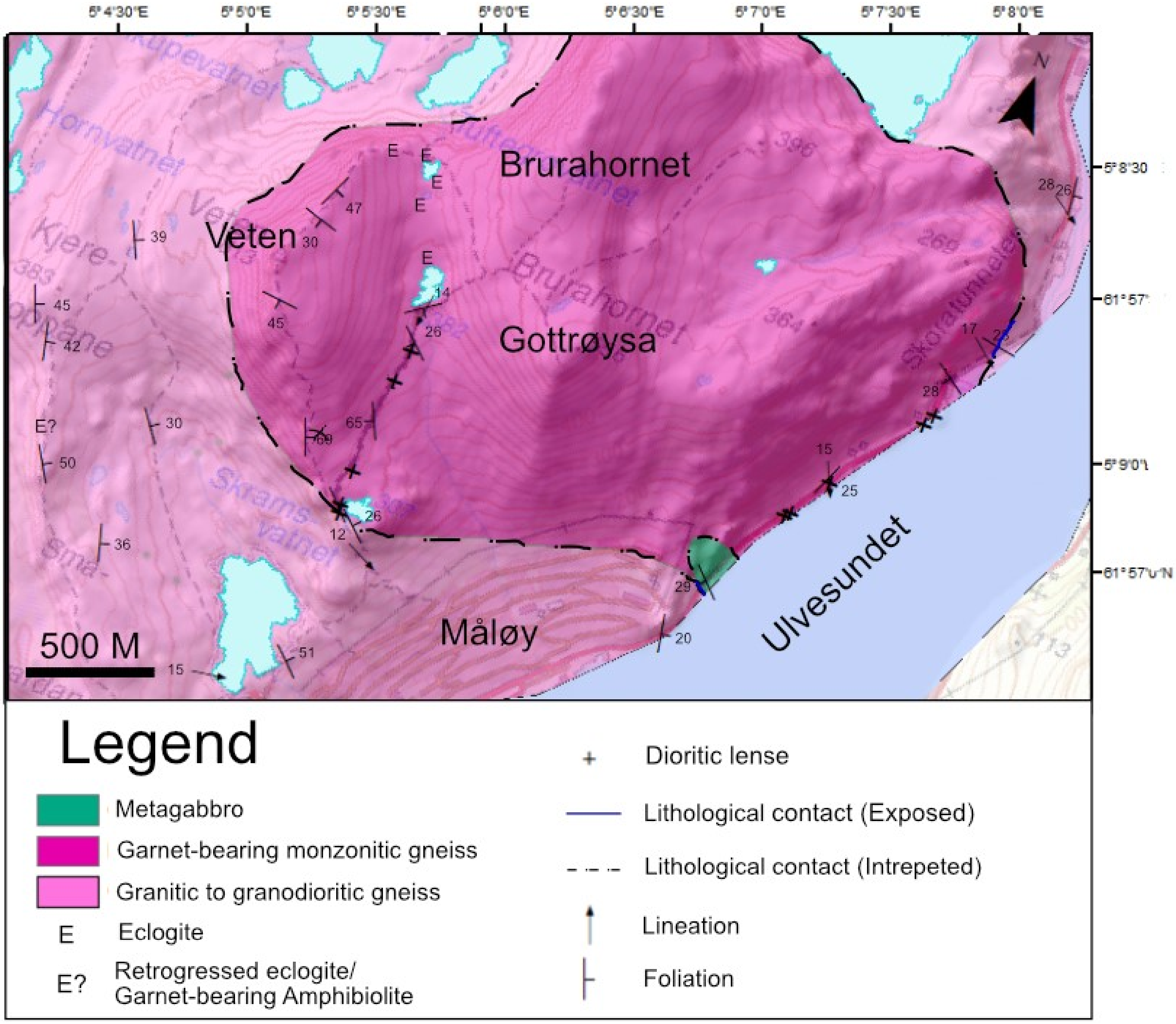

Figure 5.1.1: Geological map of the Måløy area. Representative foliations and lineations are added to the map. The full extent of structural measurements is found in appendix 2.

5.1.1 Petrology

Garnet-bearing Monzonitic gneiss

One large body of garnet-bearing monzonitic gneiss is located in the central part of the study area (Fig.5.1.1). The rock is well exposed and occupies topographic highs (Fig.5.1.2A-C). Vegetation partly covers the rock. The rock has a speckled appearance between white, dark grey, and brown, with a dark grey weathering skin. The unit is heterogenous with a general more felsic appearance towards the NNE. There is some alternating between augen texture and no augen texture. Garnet-bearing monzonitic describes the general composition, but a more syenite and dioritic composition can be observed with gradual transitions. In the mountain valley, between Mt. Veten and Mt.Gottrøysa, several feldspar lenses of different sizes are located. These are coarse-grained, dominated by K-feldspar and plagioclase, and contain a few mafic minerals. The lenses have diffuse transitions to the garnet-bearing monzonitic gneiss. The boundaries with the larger lenses are parallel to the foliation.

The garnet-bearing monzonitic gneiss is dominated by K-feldspar, plagioclase, biotite, garnet, amphibole, epidote and mineral-x* (Fig.5.1.2D-G). A smaller amount of quartz is present (Fig.5.1.2D-G). Accessory minerals are opaques, apatite and zircons. The plagioclase, biotite and amphibole are mostly recrystalized, and the quartz appears as ribbons in small pockets (Fig.5.1.2D-G). The rock is highly altered. The plagioclase is retrogressing to clinozoisite, the garnet and accessory minerals often have reaction rims, and chlorite is present.

The rock is strongly foliated and shows some folding. Towards the NNE boundary to the granitic-dioritic gneiss, there is a change in the texture of the rock. The K-feldspar starts to appear as bands and augen (Fig.5.1.2H), and right next to the boundary, all the K-feldspars show augen texture, and is surrounded by a fine-grained matrix. Sample MLM134 is taken from here. This sample shows K-feldspar augen surrounded by a fine-grained matrix dominated by recrystalized and highly altered plagioclase, biotite, and ribbon quartz (for pictures and more details see chapter 5.2.3).

*Mineral x shows some characteristic that makes it difficult to distinguish. It is yellow with a high refractive index and show low birefringence. Some grains even appear isotropic due to the low birefringence. This mineral is usually found surrounded by an epidote rim. RAMAN spectrometry gave no results, indicating that the mineral might not be crystalline anymore. The SEM gave EDS data revealing that the clinozoisite show similar chemical composition, with some difference in Fe content (Appendix 4, sample MLM37 as an example). The mineral is best identified as a clinozoisite core that is zoned towards epidote. Throughout the thesis, this mineral will therefore be referred to as clinozoizite[1] when it is present.

Figure 5.1.2: Field photographs and thin section pictures of the garnet-bearing monzonitic gneiss. (A) Photograph of Måløy with Mt. Veten and Mt. Gottrøysa. Both mountain tops consist of the garnet-bearing monzonitic gneiss. (B) Outcrops surrounding locality MLM54. (C) Outcrops on top of Mt. Veten. Photo taken by Åse Hestnes. (D-G) Thin section pictures of sample MLM47 (D-E) MLM55 (F-G). Recrystallized and altered plagioclase, biotite, epidote, and ribbon quartz in PPL(D) and XPL(E). Recrystalized and altered plagioclase, garnet, and ribbon quartz in PPL(F) and XPL(G). (H) K-feldspar augen and bands close to the boundary to the granitic-granodioritic gneiss.

Granitic to granodioritic gneiss

Another dominating unit is the granitic to granodioritic gneiss. The rock crops out in both the western part and eastern part of the study area (Fig.5.1.1). The unit is well exposed and mostly seen in large outcrops at several meters in both height and width (Fig.5.1.3A-B). It is massive, heterogeneous, grey with a dark grey and brownish weathering skin, and has an equigranular texture. Alternation between medium-grained light and dark bands, and a varying quantity of pink augen and sigma clasts occur. The composition varies between granitic and granodioritic with gradual transitions. In general, the granodioritic composition is more dominating towards the garnet-bearing monzonitic gneiss. Here a reduction in grain size is also observed. Even though the amount of quartz, K-feldspar and plagioclase varies throughout the unit, large amount of biotite are always present (Fig.5.1.3C-F). Muscovite is present and substantial in some areas. Sample MLM37 reveals plagioclase with albite twinning and some sericitization, recrystallized quartz with polygonal to lobate grain boundaries, large epidotes (Fig.5.1.3C-F) and the presence of rutile. The epidote grains are often found as rims around clinozoisite[1] grains (Fig.5.1.3E-F). In the granitic to granodioritic rock, secondary quartz is found as small lenses and veins in varying sizes, as well as secondary K-feldspar and epidote. The unit is foliated, folded and shows a L-S texture. The folds are horizontal, asymmetric and isocline folds (Fig.5.1.4 A-B). Small heart sheet folds, and tendencies to migmatization can be seen (Fig.5.1.4C-D). In the SE part of the field area, the granitic to granodioritic gneiss is found next to a gabbroic body.

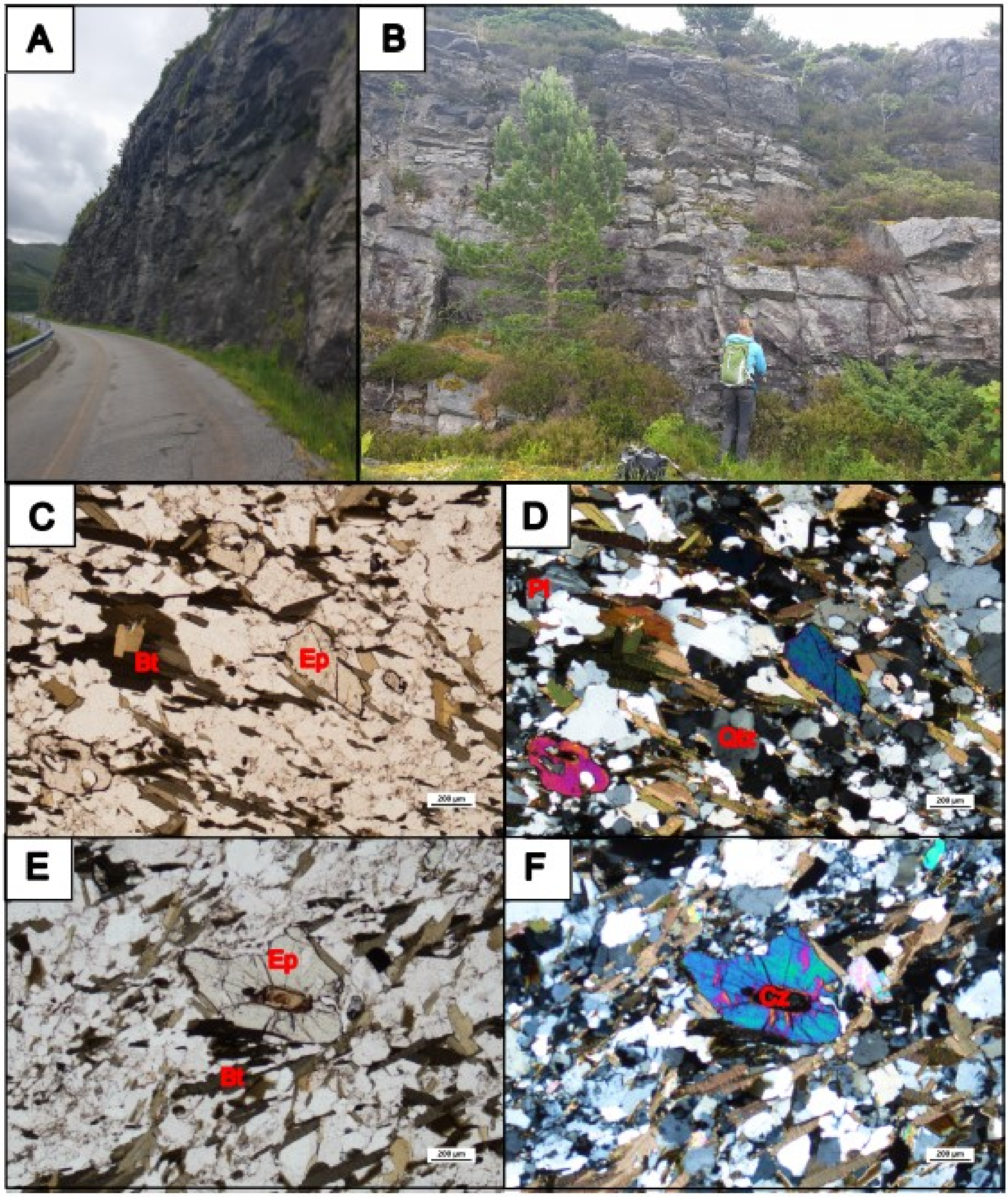

Figure 5.1.3: Field photographs and thin section pictures of the granitic to granodioritic gneiss. The granitic to granodioritic gneiss is found as large outcrops of several meters in both height and width. (A) In the NE part of the field area, the rock crops out all the way along the road at 10s of meters in height. Picture is taken between locality MLM8 and MLM9. (B) At locality MLM28 one large outcrop is located. (C-F) Thin section pictures of sample MLM37. (C)Green-beige biotite and epidote in PPL. (D) Plagioclase with albite twinning, quartz, biotite and epidote in XPL. Clinozoizite[1] surrounded by epidote in PPL(E) and XPL (F).

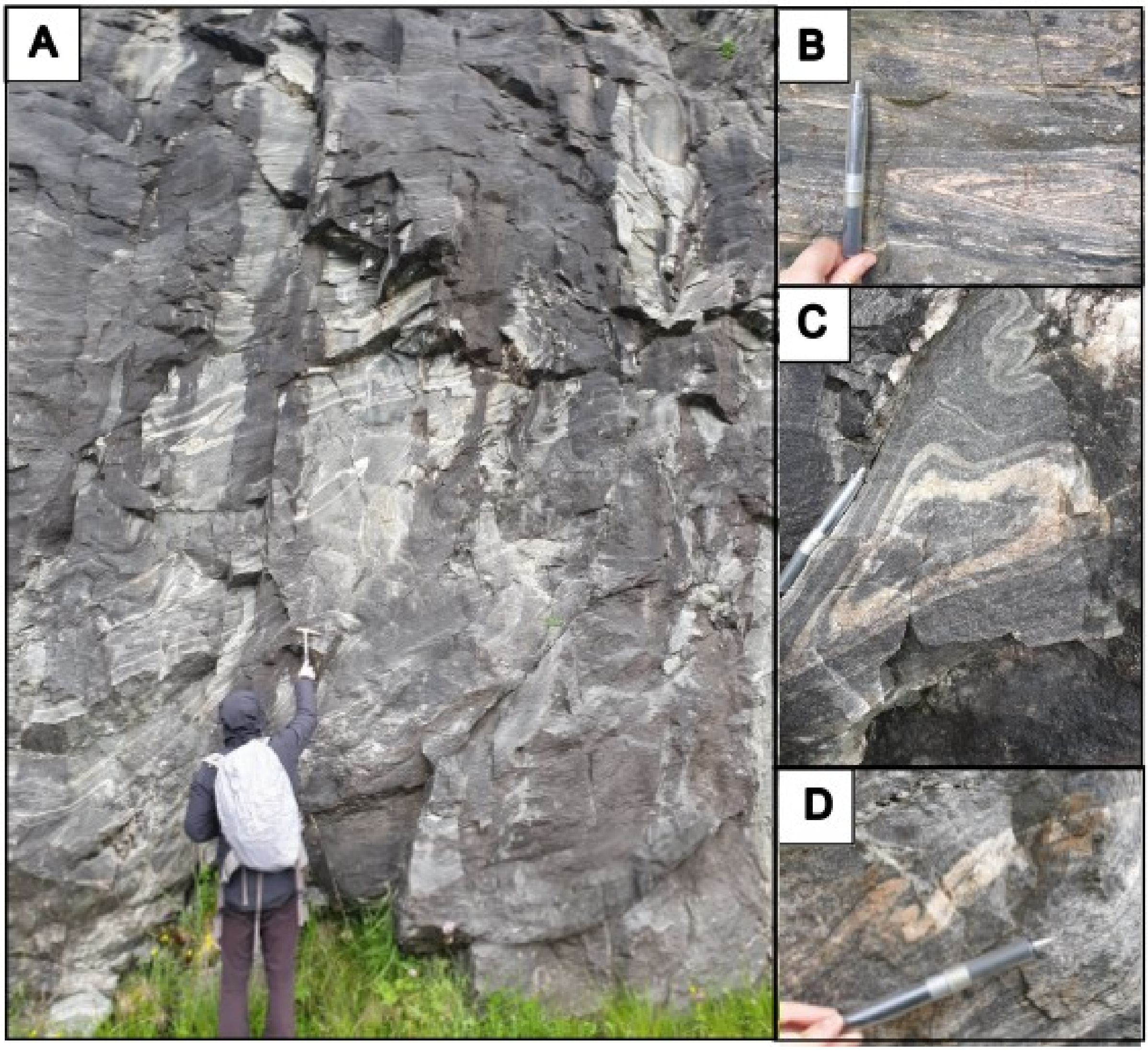

Figure 5.1.4: Field photographs of the granitic to granodioritic gneiss. (A) Locality MLM8 with a lot of asymmetric, isocline, and horizontal folds. (B) Fold at locality MLM22. (C) A heart-formed sheet fold at locality MLM8. (D) Some migmatization tendencies at locality MLM8.

Metagabbro

A gabbroic body, of at least 15 m in height and 150 m in width (Fig.5.1.5A), is found in the S part of the garnet-bearing monzonitic gneiss, with the granitic to granodioritic gneiss on the other side (Fig.5.1.1). This body consists of a mafic matrix (Fig.5.1.5B) together with large, felsic, irregular melt patches and dikes. The melt patches (Fig.5.1.5C-D) consist of medium-grained cm-big K-feldspars and plagioclase, K-feldspar and plagioclase crystals, and a smaller amount of mafic minerals (mostly biotite). The feldspar dikes cut across the SW dipping foliation of the gabbroic body in different directions (Fig.5.1.5A).

The matrix has a speckled appearance, shows strong deformation and highly altered minerals. Plagioclase, green-blue amphibole, brown biotite, garnet, clinopyroxene, epidote and clinozoizite[1] dominate the matrix (Fig.5.1.5E-H). Smaller amounts of quartz and rutile are present (Fig.5.1.5G-H). Biotite, amphibole, garnet, and clinopyroxene are usually found together. The clinopyroxene is of the sodic-calcic group (Appendix 4: MLM138, Nr1). The garnet is a mix of the end members pyrope (Mg-rich), almandine (Fe-rich), and ugrandite (Na-rich), with Mg most dominating (Appendix 4, MLM138, Nr 2). Recrystalized quartz appears in pockets of ribbon-like shape, has polygonal to lobate boundaries and shows undulose extinction (Fig.5.1.5H). The biotite, amphibole and plagioclase are recrystalized, and the plagioclase has partly regressed to clinozoisite (Fig.5.1.5F-H). Both the clinopyroxene, and the garnet are altered and surrounded by rims of amphibole, biotite, and chlorite. This indicates a partly regression. A large amount of chlorite is present, and veins consisting of epidote aggregates occur.

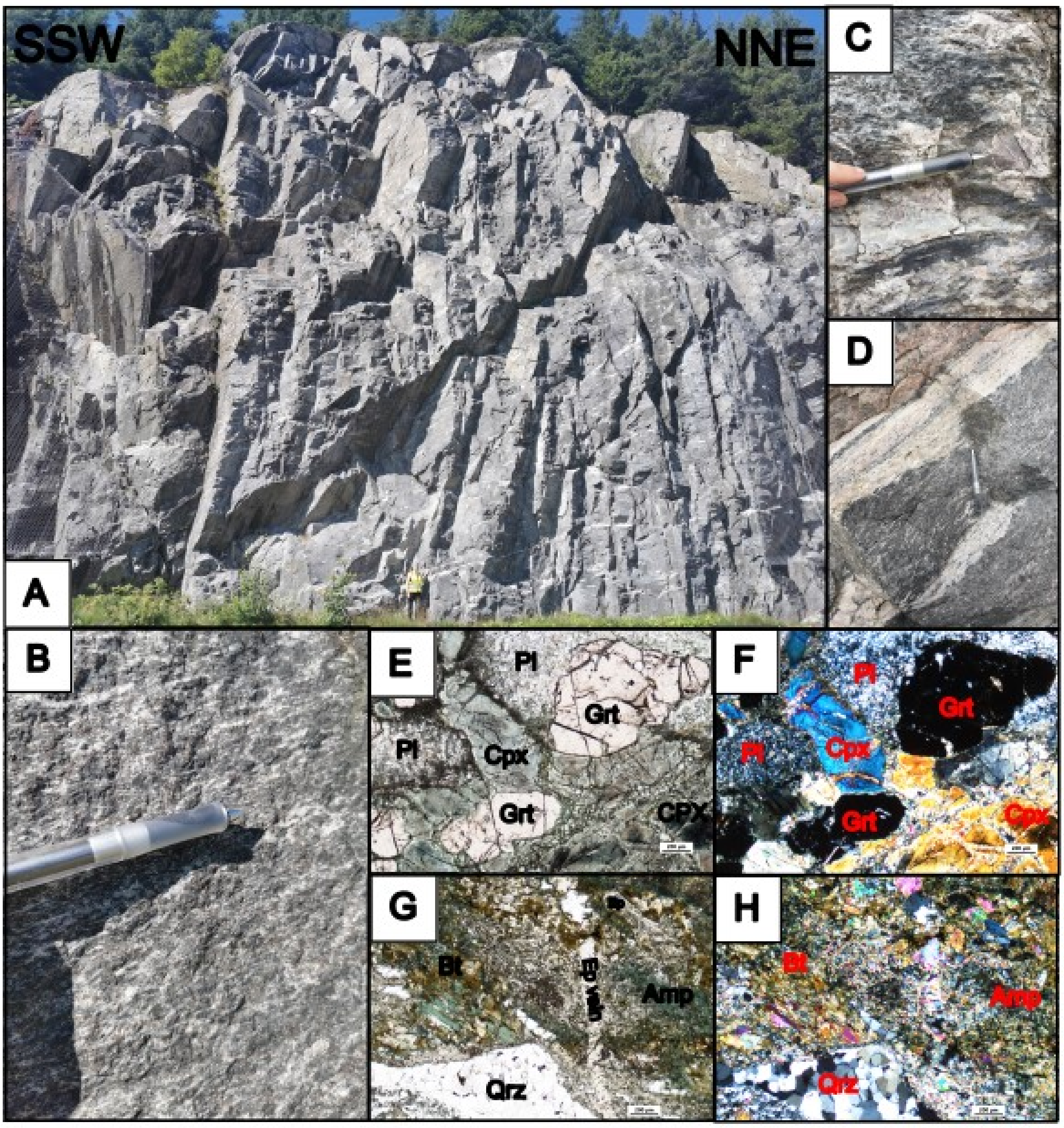

Figure 5.1.5: Field photographs and thin section pictures of the gabbroic body. (A) Part of the big gabbroic outcrop. (Photo was taken by Marius Eide). (B) Close up of the mafic matrix at locality MLM138. (C-D) Irregular and felsic melt patches consisting of K-feldspar and plagioclase. (E-H) Thin section pictures of sample MLM138. Garnet, clinopyroxene, and plagioclase in PPL (E) and XPL (F). The plagioclase is highly recrystallized and has partly retrogressed to clinozoisite. Brown-beige biotite, blue-green amphibole in PPL (G) and XPL (H). The biotite, amphibole and quartz are highly recrystallized. The quartz occurs in pockets. Several epidote veins occur.

Eclogite and Amphibolite

Eclogite and amphibolite are found as both lenses (cm-scale) and larger bodies (on several meters) in both the garnet-bearing monzonitic gneiss and the granitic to granodioritic gneiss units. The largest portion of the eclogite is found in the valley between Mt. Veten, Mt. Gottrøysa, and Mt. Brurahornet (Fig.5.1.1). The eclogite is fine-grained, brown-red and green, and with a brown-red weathering skin (Fig,5.1.6A-C). Garnet and clinopyroxene (Fig.5.1.6D-G) dominate the rock. The clinopyroxene is of the sodic-calcic group (Appendix 4: MLM59, Nr1). This together with Raman analyses (Fig.5.1.6H) indicate the clinopyroxene to be of omphacite type. The garnet is a mix of the end members pyrope (Mg-rich), almandine (Fe-rich), and ugrandite (Na-rich), with Mg and Ca dominating (Appendix 4, MLM59, Nr 2). Other minerals present are biotite, muscovite and rutile (Fig.5.1.6D-G, J-K). Thin veins filled with amphibole are seen in sample MLM59 (Fig.5.1.6J-K). The rock has a high density, is foliated and folded (open folds) (Fig.5.1.6A). The amphibolite is mostly found as lenses and is more dominating in the granitic to granodioritic unit. It is fine-grained, green, and with a dark green weathering skin. The larger amphibolite is folded (Fig.5.1.6L). Some of the bodies contain altered plagioclase (Fig.5.1.6M). This can indicate partly retrogressed eclogite or garnet-bearing amphibolite and further analysis would be needed to find the answer. There are diffuse transitions between the eclogite and amphibolite bodies to the garnet-bearing monzonitic gneiss and granitic to granodioritic gneiss.

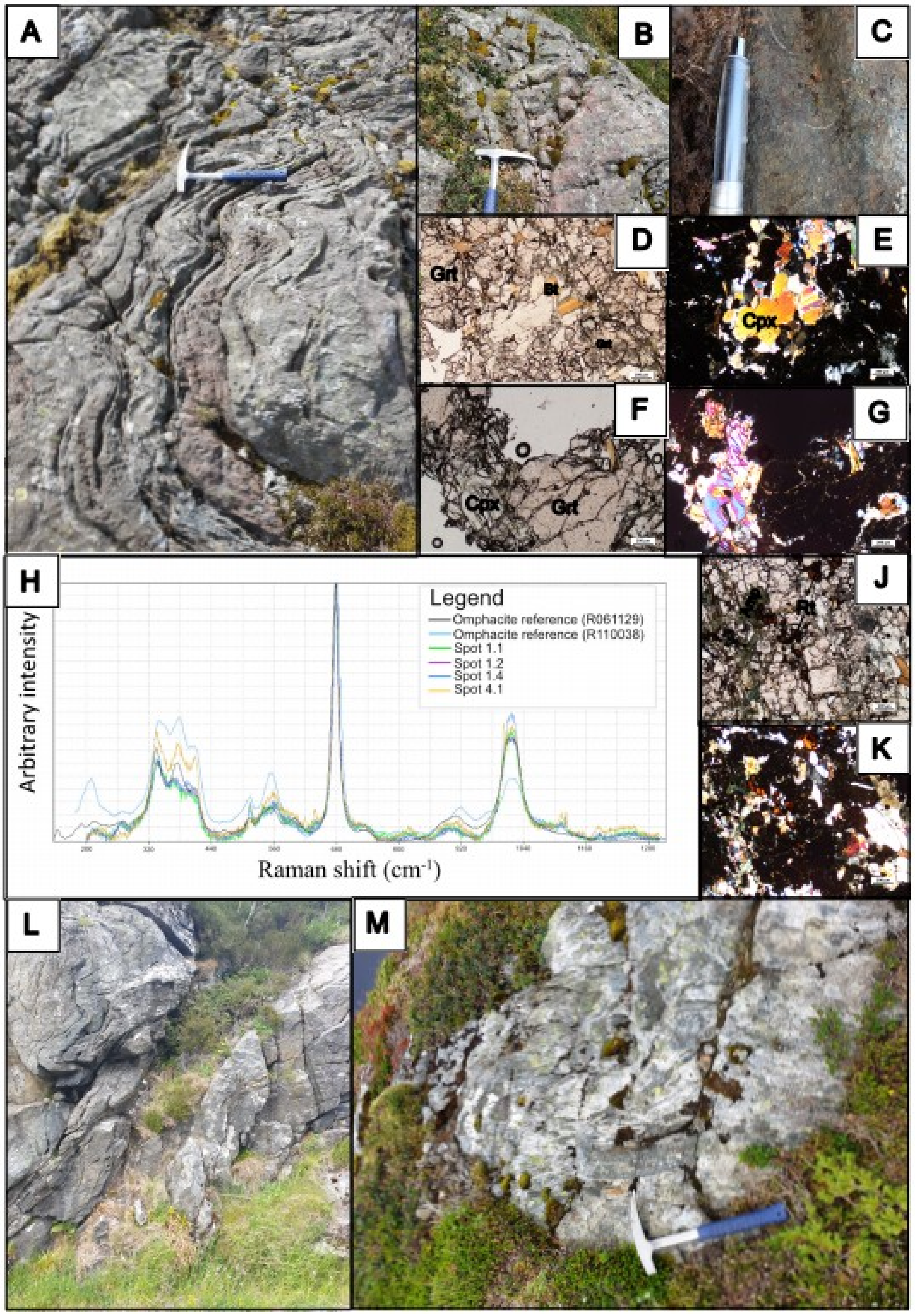

Figure 5.1.6: Field photographs of the eclogite and amphibolite, and thin section pictures of sample MLM59 (from one of the eclogite bodies). (A) Field photographs of eclogite bodies from locality MLM57. (B) Field photograph from locality MLM65. (C) Field photograph from locality MLM 47b. (D-G, J-K) Thin section pictures from sample MLM59. Garnet, clinopyroxene (omphacite) and biotite in PPL (D, F) and XPL (E, G). Amphibole vein and rutile in PPL (J) and XPL(K). (H) Raman analyses for different clinopyroxene in sample MLM59 compared to two omphacite references. (L) Field photograph of amphibolite from locality MLM10. (M) Field photograph of a partly retrogressed eclogite/garnet-bearing amphibolite from locality MLM69.

Dioritic lenses

Dioritic lenses are seen in the SW and SE part of the garnet-bearing monzonite. The lenses are deformed and highly altered. They have a speckled appearance between white, dark grey, and a hint of red, and show a light grey weathering skin (Fig.5.1.7A-B) The rock is medium- to coarse-grained and are dominated by plagioclase, brown-beige biotite, blue-green amphibole, epidote, and a varying amount of garnet (Fig.5.1.7C-F). Smaller amounts of quartz occur (Fig.5.1.7E-F), and a few K-feldspar grains are seen. Accessory minerals are rutile, opaques, clinozoisite, chlorite, and titanite (Fig.5.1.7E-F). The biotite, amphibole, and epidote often cluster together. The recrystallized quartz shows polygonal boundaries and undulose extinction. The plagioclase is recrystallized with the old boundaries still partly visible and strongly retrogressed to clinozoisite. Rutile and opaques are mostly found surrounded by titanite reaction rims. In a few places, the rutile surrounded by titanites rims have opaque inclusions in the middle. The rock is foliated, shows a L-S texture and has diffuse transitions to the garnet-bearing monzonitic gneiss.

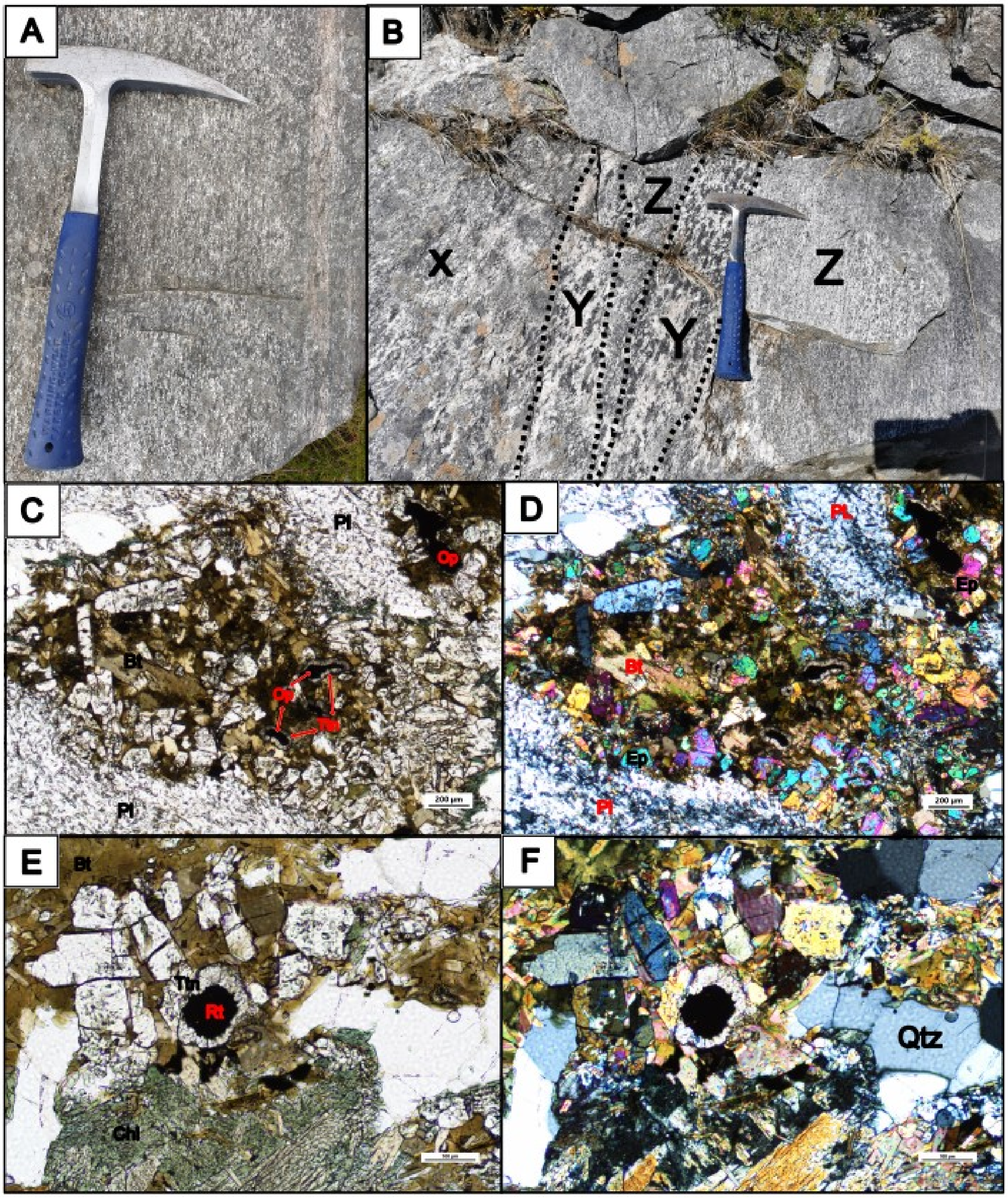

Figure 5.1.7: Field photographs and thin section pictures of the dioritic lenses. (A) Field photograph from locality MLM19b. (B) Field photograph from locality MLM167. Here the medium-grained diorite, x, coarse-grained diorite, Y, and the garnet-bearing monzonitic gneiss is seen, Z. (C-F) Thin section pictures of sample MLM19b. Plagioclase, biotite, epidote aggregates, and opaques with titanite rims in PPL(C) and XPL(D). Biotite, chlorite, amphibole, rutile with titanite rim, and quartz in PPL(E) and XPL(F).

5.1.2 Lithological contacts and structural results

All the units show a trend of stronger deformation towards the boundaries. The boundary between the garnet-bearing monzonite and the gabbroic body is covered by vegetation. Between the gabbroic body and the granitic to granodioritic gneiss, a possible tectonic contact is found (Fig.5.1.8A). No clear indications for how the blocks have moved relative toward each other are found. Between the garnet-bearing monzonitic gneiss and the granitic to granodioritic gneiss, one clear shear zone is located in the N (Fig.5.1.8B). This boundary is sharp and strongly sheared which can indicate a primary contact that has developed into a shear zone. In the NE part the contact is covered by vegetation. All the units described above are metamorphosed and show linear and planar fabrics. They all show L-S fabrics, formed by stretching and recrystallization of quartz. The granitic to granodioritic gneiss also shows stretching of K-feldspar and biotite, while the garnet-bearing monzonitic gneiss shows recrystallization and stretching of the plagioclase, biotite and amphibole as well. The foliation is clearly different in the garnet-bearing monzonitic gneiss unit and the granitic to granodioritic gneiss unit. The garnet-bearing monzonitic gneiss shows a pronounced foliation dipping towards S (Fig.5.1.9A), while the granitic to granodioritic gneiss shows a foliation with dip direction towards NE (Fig.5.1.9B).

Garnet, clinopyroxene and plagioclase in the metagabbro indicate a peak in high-pressure granulite-facies metamorphism. Plagioclase, amphibole, garnet, epidote indicate a possible amphibolite facies metamorphism in the garnet-bearing monzonitic gneiss and dioritic lenses. The amphiboles may have retrogressed from pyroxene, indication a peak in granulite facies metamorphism predating the amphibolite facies metamorphism. Based on the presence of eclogite and amphibolite lenses, the rocks have been overprinted by amphibolite and eclogite facies metamorphism. The granitic to granodioritic gneiss show no evidence for a granulite-facies metamorphic event, but only for amphibolite-facies metamorphism. All the rocks have a high content of epidote and chlorite, indicating partly retrogression to greenschist- facies metamorphism.

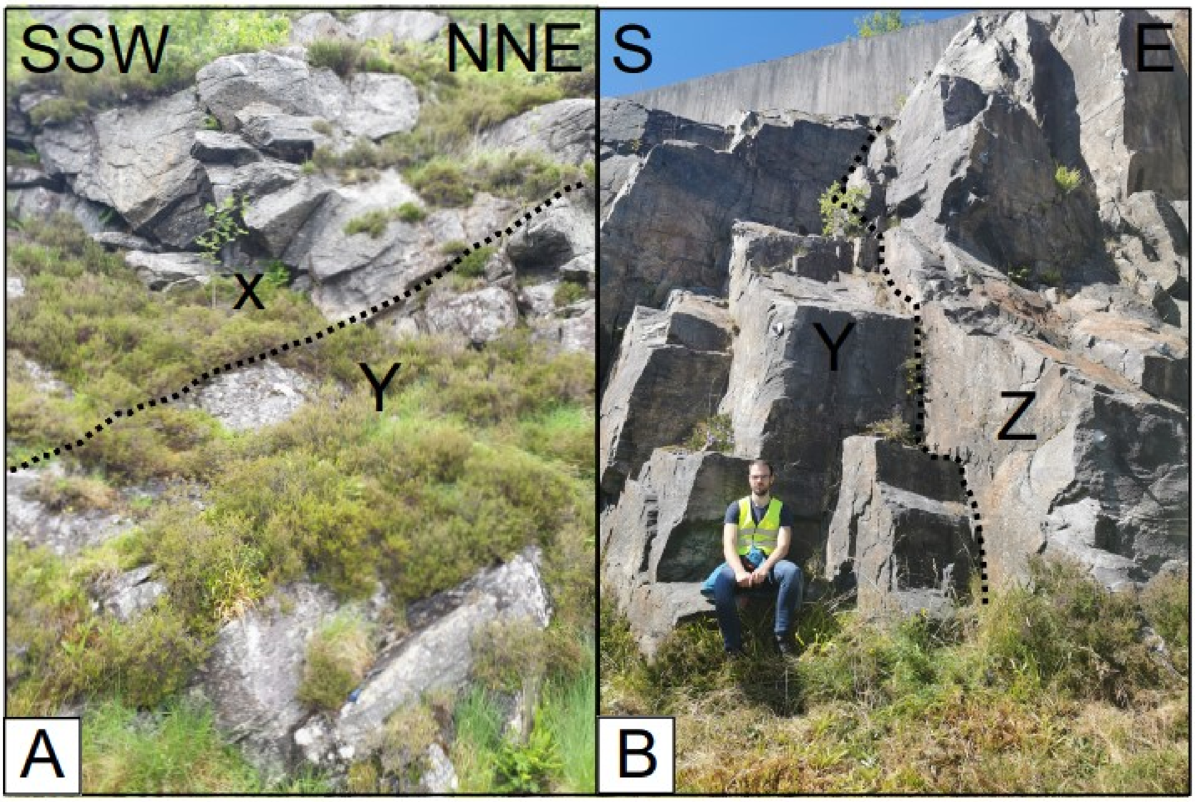

Figure 5.1.8: Field photographs of lithological contacts. (A) A shear zone boundary between the garnet-bearing monzonitic gneiss, x, and the granitic to dioritic gneiss, y. There are no clear indications of the direction of movement along the shear zone separating the two lithologies. (B) A tectonic contact between the granitic to granodioritic gneiss, y, and the metagabbro, z. There are no clear indications of the direction of movement between the granitic to granodioritic gneiss and the metagabbro.

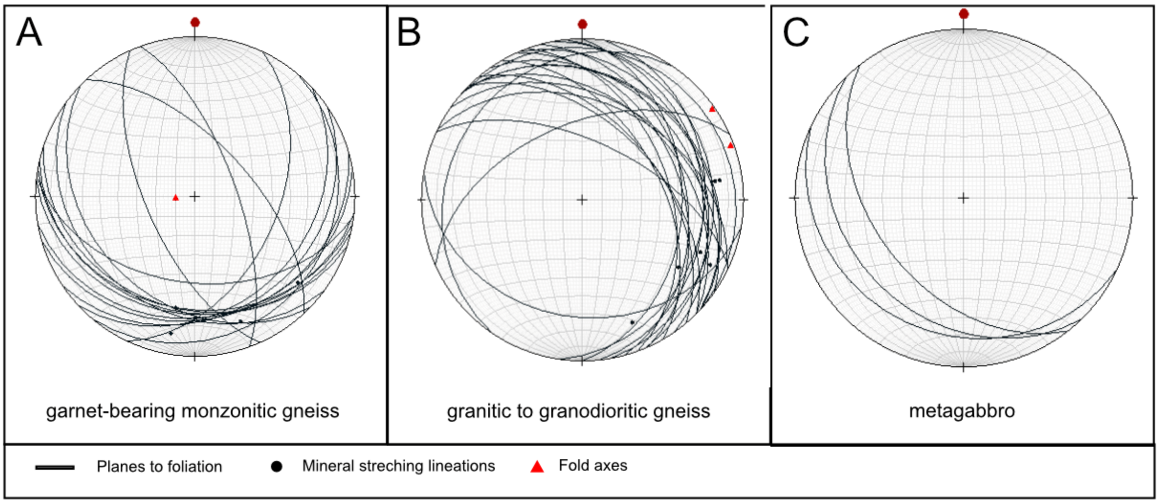

Figure 5.1.9. Stereographic projection of foliation and lineation measurements in the different units. A few fold axes are also measured. (A) The garnet-bearing monzonitic gneiss shows a foliation trend dipping towards SW to SE, except for a few outliers. (B) The granitic to granodioritic gneiss shows foliation trend dipping towards NE. A few measurements differ from this. (C) The metagabbro shows a foliation trend that dips towards SW.

Shear zones

A few shear zones are observed in the field area. One larger shear zone is observed as the boundary between the garnet-bearing monzonitic gneiss and the granitic to granodioritic gneiss (Fig.5.1.10A). In the SE part of the granitic to granodioritic gneiss, three shear zones with quartz monzonitic bodies in the granitic to granodioritic gneisses is observed. The zones are foliation parallel zones. The monzonitic bodies are strongly deformed, consisting of a medium- to fine-grained matrix that show some banding and sigma clasts consisting of K-feldspar with some mafic inclusions. A top to the NW movement is indicated by the sigma clasts (Fig.5.1.19B-C).

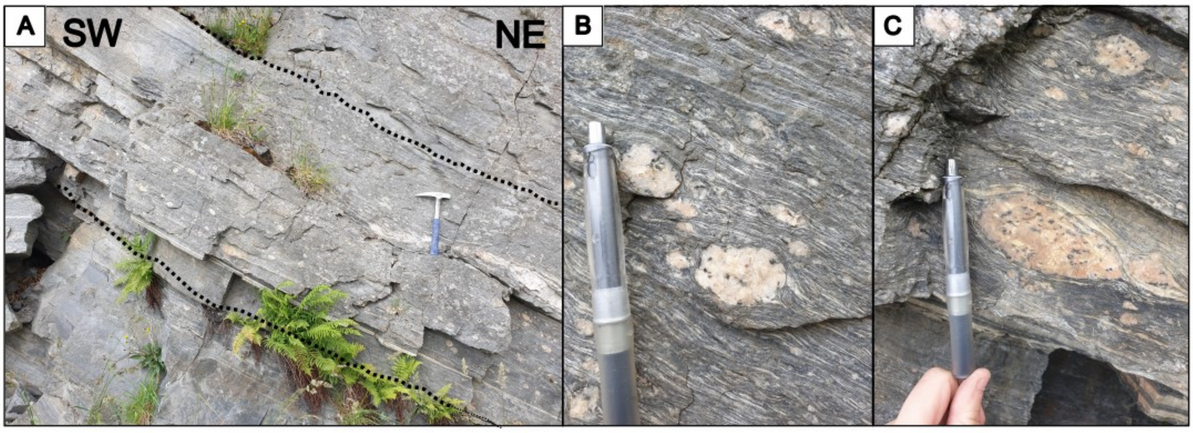

Figure 5.1.10: (A) Field photograph of a Shear zone consisting of monzonitic gneiss in the granitic to granodioritic gneiss at locality MLM27. The shear zone dips towards NE like the foliation of the granitic to granodioritic rock. (B and C) sigma clasts, in the highly deformed monzonitic body, consisting of K-feldspar with some mafic inclusions. They indicate a top to NW movement.

5.2 U-Pb geochronological and petrological characteristics

This chapter will present petrological and U-Pb geochronological characteristics for a total of eight samples. The results are shown in Table 1. Petrological characteristics, sample localities, internal texture of the zircons and, the geochronological results will be described. The description of the internal textures of the zircons are based on Corfu et al. (2003). Fig.5.2.1 and table 1 presents the samples localities, and Fig 5.2.2 shows legend for geochronological date used in the Terra-Wasserburg diagrams. The samples are displayed in order based on the crystallization age from oldest to youngest.

Figure 5.2.1: Map over Nordfjord region in western Norway. Red stars represent the eight samples for zircon U-Pb geochronological and petrological studies.

Table 1: List of sample localities and geochronological results listed from oldest to youngest.

Samples	Lithology	Coordinates	Outcrop description	Igneous crystallization age (Ma)	Metamorphic age (Ma)
VAH48	Granitic augen gneiss	62°11′55.3″N 005°11′4.3″E	Roadcut, Honningsvåg	1651±7	
MLM134	Quartz-Monzonitic augen gneiss	61°57′20.2″N 005°8′26.7″E	Roadcut, Måløy	1627±18	1050±110
VAH78	Granitic augen gneiss	61°56′19.4″N 005°29′34.3″E	Roadcut, Hornindal	1625±16	1032±100
VAH04	Monzonitic augen gneiss	61°39′47.5″N 006°49′17.7″E	Oldedalen	963±7	
VAH11	Monzonitic augen gneiss	61°50′55.7″N 006°57′45.1″E	Along hiking trail, Mount Skåla, Loen	958±7	
VAH23	Granitic banded augen gneiss	61°35′20.8″N 005°2′34.8″E	Roadcut, Florø	942±9	
VAH31	Granitic augen gneiss	61°44′58.4″N 005°56′25.4″E	Backroad, Hyen	928±44	400±10
VAH44	Granitic augen gneiss	61°55′38.7″N 005°27′31.1″E	Roadcut, Maurstad	904±21	408±9

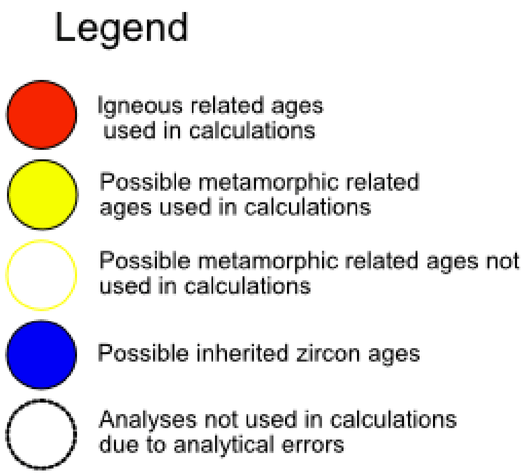

Figure 5.2.2: Legend illustration used for the geochronological data that are presented in the Terra-Wasserburg diagrams.

5.2.1 Sample VAH48, granitic augen gneiss, Honningsvåg

This granitic augen-gneiss was sampled at Honningsvåg (Fig.5.2.1). It is found at the south-east side of a well-exposed outcrop by the road (Fig.5.2.3A). On the north-west side of the outcrop, the rock gradually transitions into a more amphibole rich rock. The rock is found together with pegmatitic dikes that are 10-15 cm wide. The granitic augen-gneiss shows a porphyritic texture (Fig.5.2.3B). It contains coarse-grained K-feldspar augen and bands that are surrounded by a fine-grained matrix. Green-beige biotite, plagioclase, quartz, K-feldspar, scapolite, epidote aggregates, and muscovite dominate the matrix. Accessory minerals are titanites (dominates), relatively large zircons, apatite, and clinozoizite[1]. Albite twinning is shown in the plagioclase and, myrmekitic texture is typically present in the smaller K-feldspar grains. Biotite, titanite and epidote often occur together (Fig.5.2.3C-D). A few of the titanites show the characteristic diamond shape, while the dominating portion of them are more rounded at the edges. Distinctive harlequin colours are seen in many of the epidotes. The scapolite (Fig.5.2.3E-F) appears as large grains compared to the rest of the matrix. They show unusual high interference colours, but, partly inconclusive RAMAN spectrometry (Fig.5.2.4), and EDS data support the identification (Appendix.4, VAH48). The scapolite has typically alterated from plagioclase (Deer et al., 2013). Scapolite and epidotes are often surrounded by muscovite. The zircons are found with the feldspar, the quartz, and the biotites. Polygonal till lobate boundaries, and undulose extinction are shown in the recrystallized quartz. The feldspar shows sericitization and saussuritization, indicating retrogression of the rock in a hydrothermal environment.

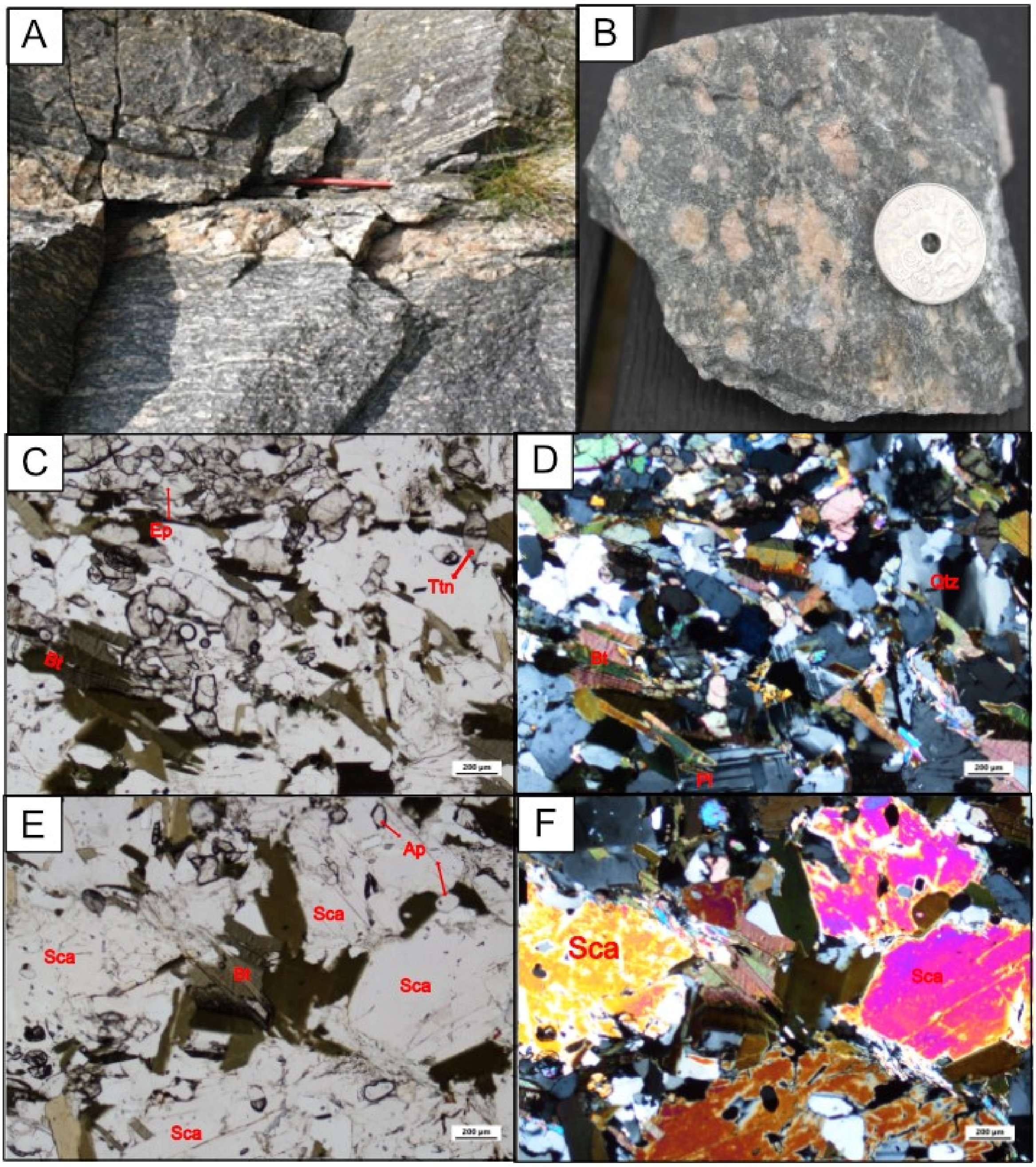

Figure 5.2.3: (A) Field photograph of locality VAH48. The granitic augen-gneiss with a pegmatitic dike. (B) Sample VAH48. (C) Biotite, titanite and epidote in PPL. The white minerals are feldspar and quartz. (D) Biotite, titanite, epidote, quartz and feldspar in XPL. Distinctive albite twinning in the plagioclase. (E) Biotite, scapolite, and apatite in PPL. (F) The biotite, apatite and, the large scapolite with distinctive interference colour in XPL.

*The scapolites show unusual high interference colours, making them difficult to determine as scapolite's. The RAMAN spectrometry analysis reveals the endmembers of scapolite, meionite and marialite, as the best fit (Fig.5.2.4).

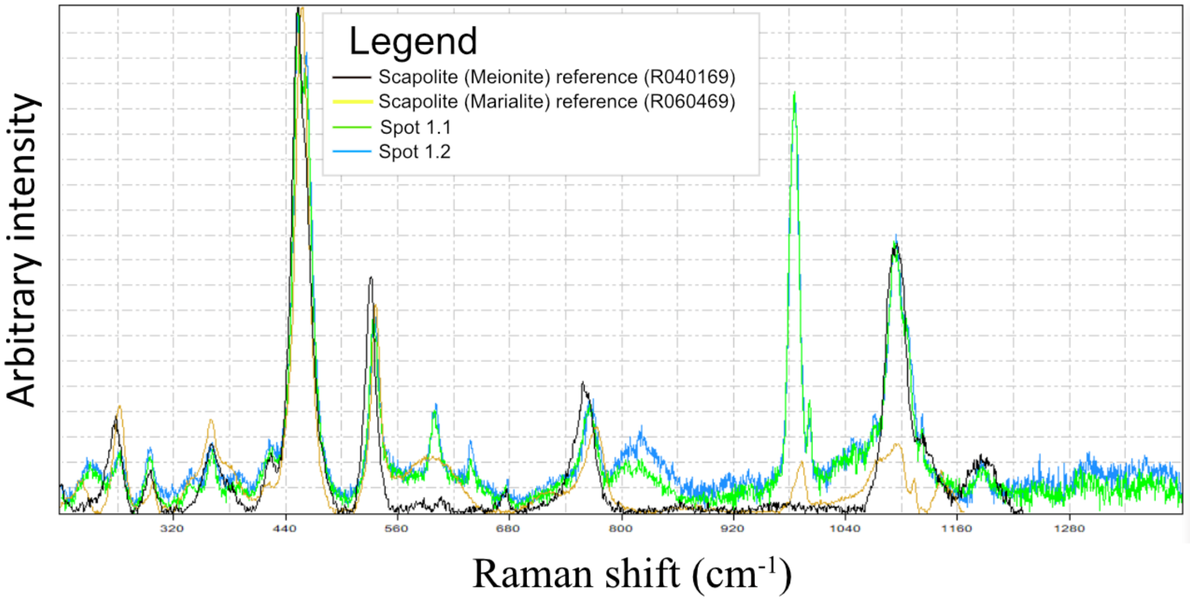

Figure 5.2.4: RAMAN spectrometry analyses of different scapolite's in sample VAH48 compared to references of the two endmembers of scapolite, meionite and marialite. The analyses do not give a perfect match, one of the large peaks of the scapolite's from sample VAH48 is not seen in the references. Even though the RAMAN analysis did not give a clear answer to the type of mineral this is, the scapolite references gave the best estimated fit. The mineral is therefore referred to as a scapolite.

The zircons from this sample are subhedral and consist of elongated crystals. They range from 100-300µm in size with an aspect ratio ranging between 2 and 3.5. The crystals are either clear or light brown. Many of the zircons are rich in inclusions, a few have fractures, and a few fragments occur. In CL imaging, the zircons are dominated by partly oscillatory zoned, convolute zoned, and blurred cores that are surrounded by oscillatory zoned domains (Fig.5.2.5A). Some of the zircons are oscillatory zoned throughout the grains. Additional characteristics are thin, irregular, high luminescence rims, most of which are too thin to be analyzed. Fourteen spots were analyzed on thirteen different grains. Twelve of these analyses were done on oscillatory zoned domains, while two were done on highly luminescent rims (spots 9.2 and 10.1). For the oscillatory zoned domains, the U concentration range between 106-315 ppm (average=208 ppm) (Appendix 1), and the Th/U ratio vary between 0.16 and 0.94 (average=0.60). For the two rim domain (spot 9.2 and 10.1), the U concentration are 285 ppm and 603 ppm, and the Th/U ratios are 0.17 and 0.20 respectively. Two analyses (spot 9.1 and 10.1) were excluded from further calculation due to high reverse discordance, while two other analyses (spot 4.1 and 6.1) were excluded due to Pb-loss. One analysis (spot 9.2, Fig 5.2.5 A-B) does not fit the remaining analyses but fall slightly outside. The analysis (spot 9.2) is partly overlapping two different domains (Fig.5.2.5A) but mainly appear in the rim domain. There is no clear indication that this analysis represents a metamorphic domain; it can be considered as either a magmatic overgrowth or a metamorphic rim. The remaining nine analyses give a common Concordia age of 1651±7 Ma (Fig.5.2.5B) and a weighted mean $^{207}Pb/^{206}Pb$ age at 1649±11 Ma (Fig.5.2.5C). The ages are identical within the error limits and are interpreted as the best estimated igneous crystallization age of this granitic augen-gneiss protolith.

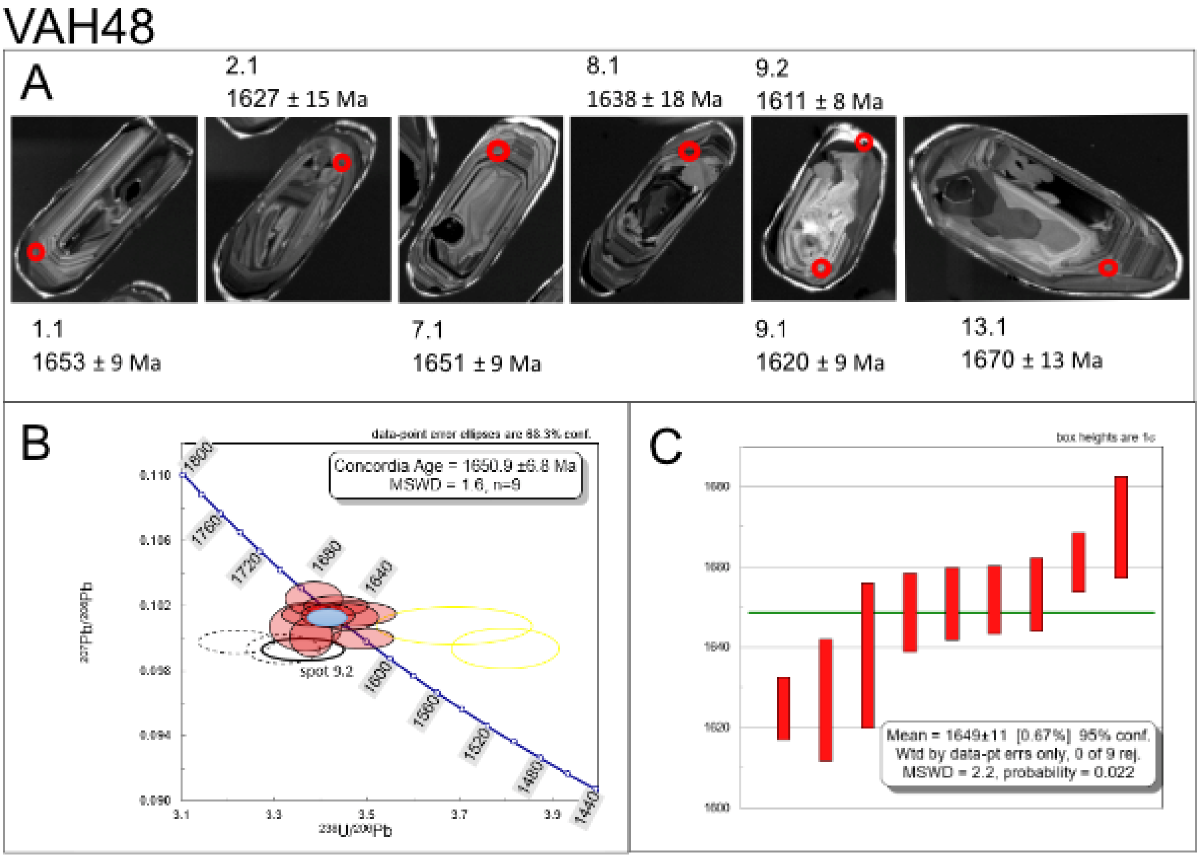

Figure 5.2.5: Results of sample VAH48: (A) Representative CL-images with 207Pb/206Pb ages of the analyzed zircons. Red circles mark the analyzed spot with a diameter of ca. 20µm. (B) A Terra-Wasserburg plot of all analyses. All analyses are corrected data, and the error ellipses are plotted at the 1σ level. The Concordia age (blue) is given with 2σ errors. Spot 9.2, representing a highly luminescent rim, is marked in a black, unfilled circle. (C) Weighted mean $^{207}Pb/^{206}Pb$ of the concordant ages (n=9). Box hight at 1σ.

5.2.3 Sample MLM134, quartz-monzonitic augen gneiss, Måløy

This monzonitic gneiss was sampled from Måløy (Fig.5.2.1), on the south-west side of a shear zone. Coarse-grained K-feldspar augen are surrounded by a fine-grained matrix (Fig.5.2.6A). In the matrix, there are alternating quartz bands, plagioclase bands, and bands with biotite, clinozoisite, and epidote. Accessory minerals are zircons, opaques, apatite, garnet aggregates, and clinozoizite[1] (Fig.5.2.6D-F). They are often found together in the biotite, clinozoisite, and epidote bands. The biotite rich bands often form eye-like shapes (Fig.5.2.6B-C). K-feldspar eyes are characterized by cross-hatch twinning, indicating microcline. The twinning is strongly deformed. The recrystallized quartz appears as ribbon quartz (Fig.5.2.6C), typically for rocks affected by high-T shearing. Undulose extinction often occurs in the quartz grains. Strong saussuritization and recrystallization affected the plagioclase (Fig.5.2.6C). The primary grain boundaries for the plagioclase are some places still visible.

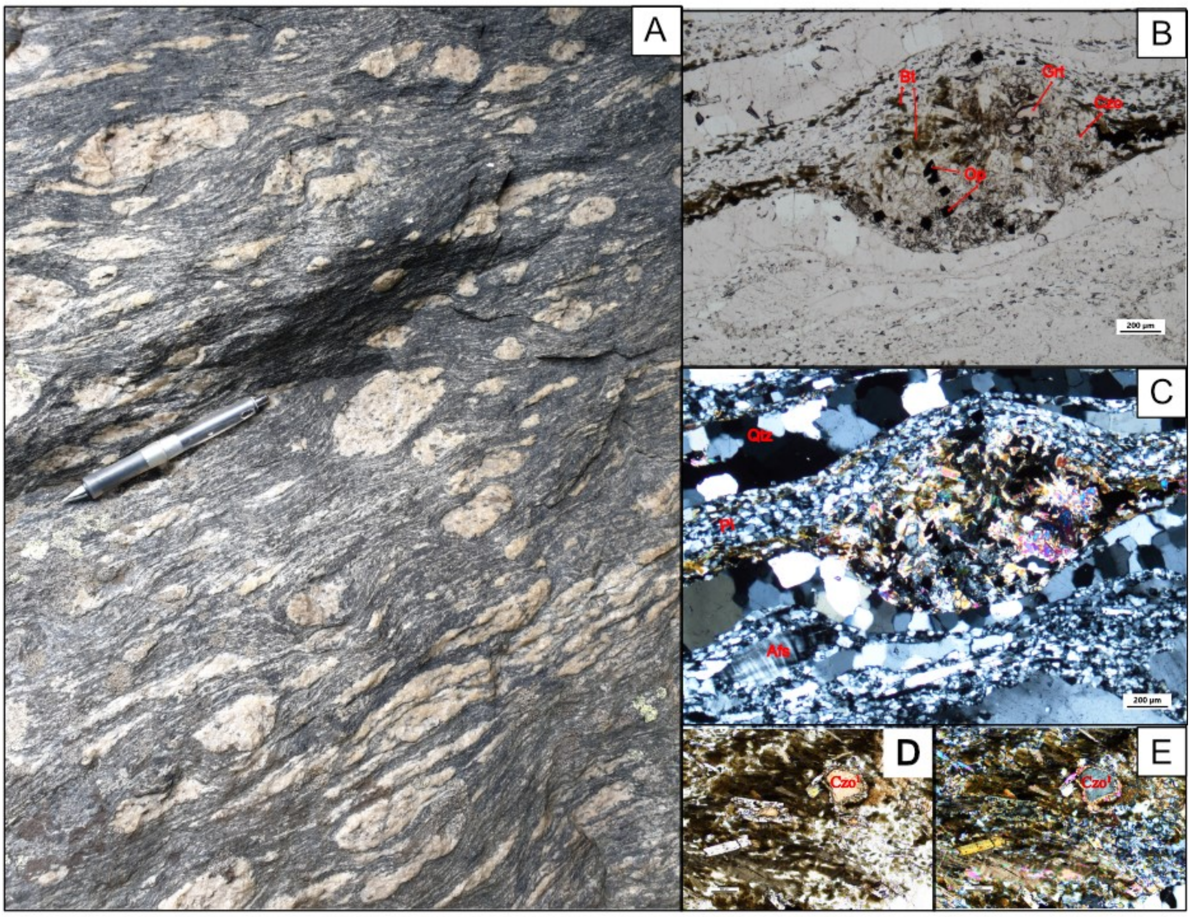

Figure 5.2.6: (A) Field photograph of sample MLM134. (B) The eye-shaped biotite rich bands. Including clinozoisite, epidote, opaques, and garnet aggregates. The white minerals are quartz feldspar. (C) The eye shape in XPL. Around are the strongly saussuritization and recrystallized plagioclase and the ribbon quartz. A K-feldspar with cross-hatch twinning is also seen here. (D) Clinozoizite[1] with epidote rim in PPL together with biotite. (E) Clinozoizite[1] with epidote rim in XPL together with biotite.

The zircons from this sample are subhedral with rounded edges and consist of relatively stubby grains. They have a significant variation in length up to 250 µm with an aspect ratio between 1.4 and 2.5. The crystals are, for the most part, clear with a tint of brown. The crystals have many inclusions, and a few are fractured. In CL-imaging, there is a considerable variation in texture within the grains. One of the characteristics are dark, oscillatory zoned domains (spot 4.1, Fig.5.2.7A). Some show oscillatory zoned cores surrounded by texture-less or smudged overgrowths (spot 1.1 and 10.1, Fig.5.2.7A). Other domains are patchy and messy, and some are sector zoned, while others are partly oscillatory zoned. Convolute zoning occurs in some of the grains. Fifteen spots were analyzed on fifteen different grains. Twelve analyses were done on oscillatory zoned domains, two on high luminescence, structureless domain, and one on low luminescence, structureless domain. The U concentration for the oscillatory zoned domains range between 118-583 ppm (average=323ppm) (Appendix 1), while the Th/U ratio vary between 0.16 and 0.89 (average=0.48). The U concentration for the two bright, structureless domains are 132 ppm and 139 ppm, while their Th/U ratios are at 0.71 and 0.74. For the dark, structureless domain, the U concentration is at 1152 ppm, and the Th/U ratio at 0.03, indicating a possible metamorphic domain. One analysis (spot 3.1) was excluded from further calculation due to high reverse discordance. A total of fourteen analyses give a Discordia line with an upper intercept at 1627±18 Ma and a lower intercept age at 1050±110 Ma (Fig.5.2.7B). The upper intercept age is interpreted as the best estimated igneous crystallization age for this quartz-monzonitic augen-gneiss protolith, while the lower intercept age is interpreted as the age of a metamorphic overprint.

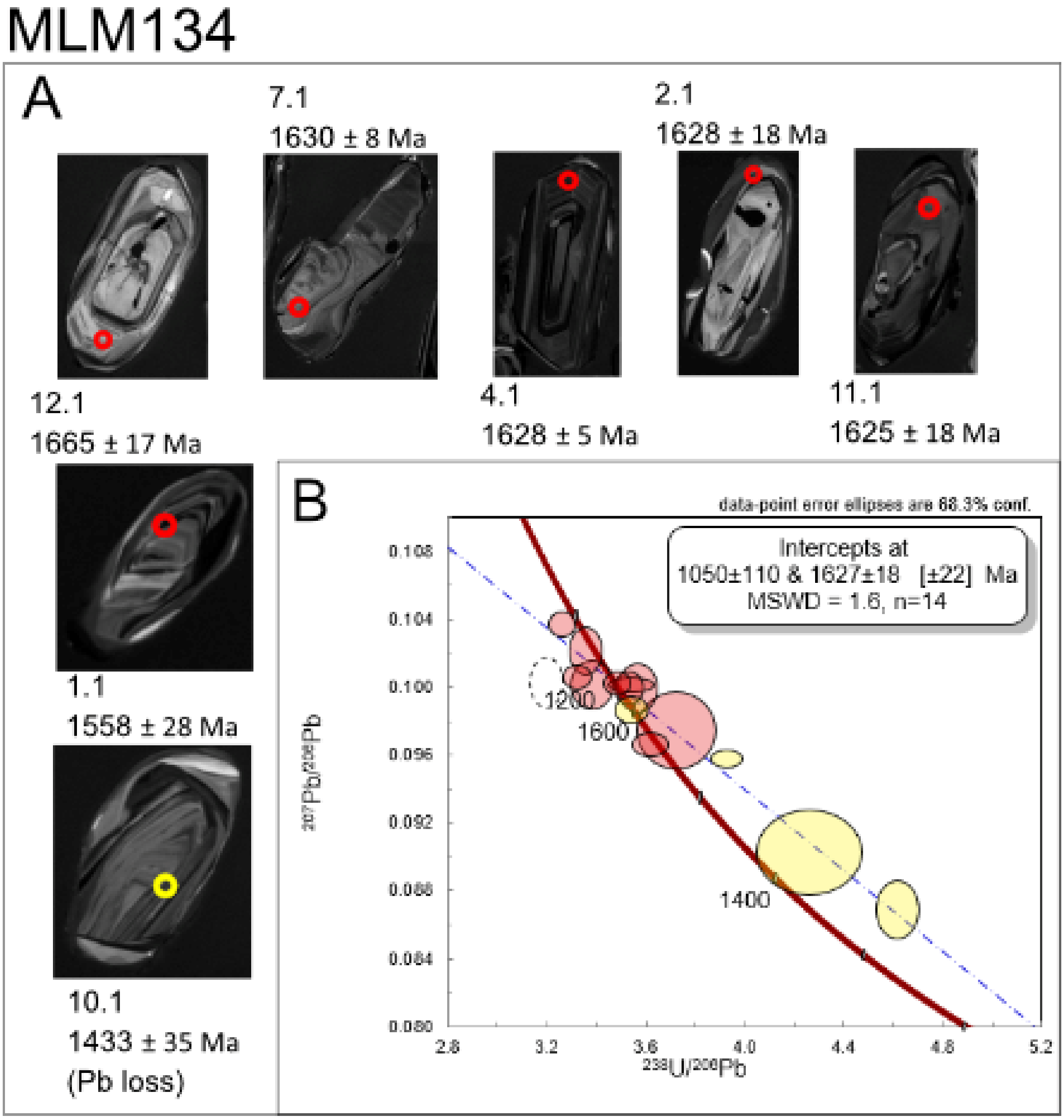

Figure 5.2.7: Results of sample MLM134: (A) Representative CL-images with 207Pb/206Pb ages of the analyzed zircons. Analyses without description are concordant analyses. Red and yellow circles mark the analyzed spot with a diameter of ca. 20µm. (B) Terra-Wasserburg plot of all the analyses. All analyses are corrected data, and the error ellipses are plotted at the 1σ level.

5.2.2 VAH78, granitic augen gneiss, Hornindal

This granitic augen-gneiss was sampled at Hornindal (Fig.5.2.1). The rock is strongly deformed and shows a porphyritic texture (Fig.5.2.8A) with white augen that consist of medium-grained K-feldspar and some quartz grains (Fig.5.2.8B). In the matrix, green-beige biotite, quartz, K-feldspar, plagioclase, muscovite, and epidote dominates (Fig.5.2.8C-D). Accessory minerals are zircons, opaques, titanites, apatite, and clinozoizite[1]. Some of the K-feldspars are characteristic by cross-hatch twinning, indicating microcline. The cross-hatch twinning is strongly deformed. Albite twinning is shown in the plagioclase (Fig.5.2.8D). The biotite, muscovite, and epidote aggregates often found together (Fig.5.2.8C-D). The recrystallized quartz shows lobate grain boundaries, undulose extinction, and often appear as ribbons. Some of the feldspars show saussuritization and sericitization. Several biotites have partly regressed to chlorite. The presence of chlorite, saussuritization and sericitization indicates retrogression of the rock in a hydrothermal environment.

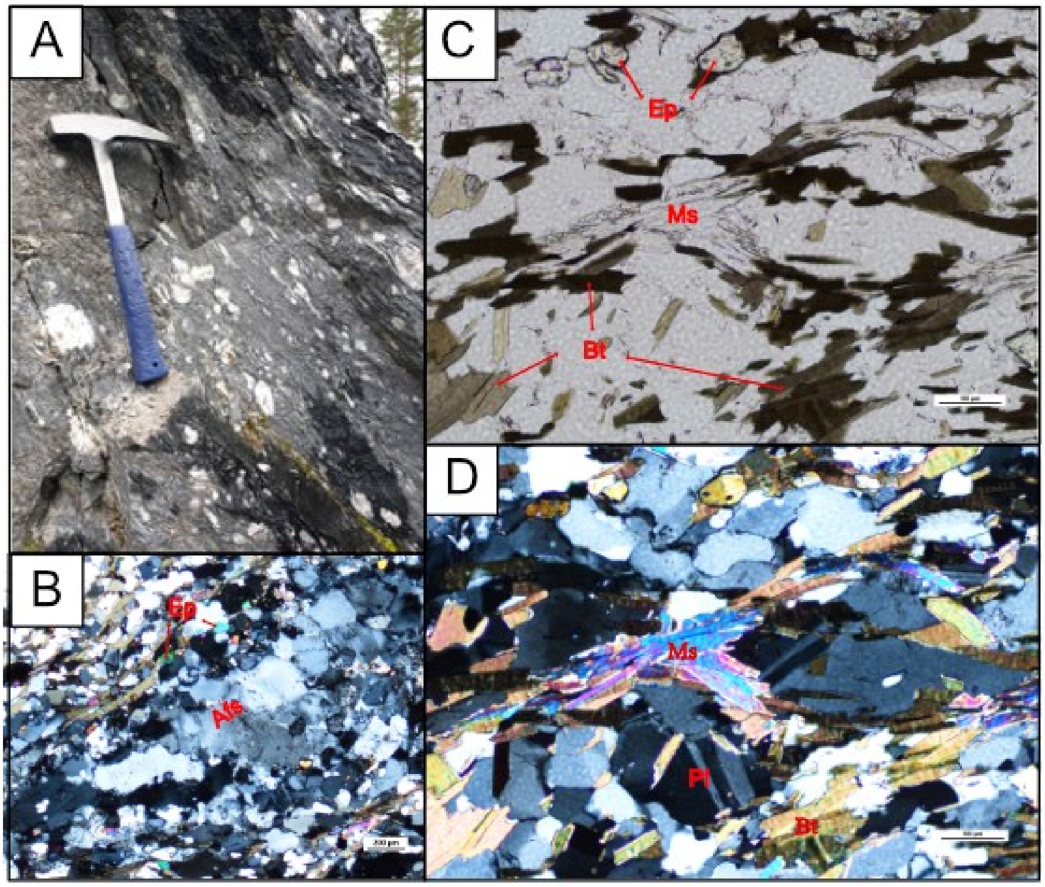

Figure 5.2.8: (A) Field photograph from locality VAH78. (B) K-feldspar augen and epidote aggregates in XPL. Sericitized K-feldspar is common. (C) Biotite, muscovite and epidote aggregates in PPL. (D) Biotite, muscovite and epidote aggregates in XPL. Albite twinning in plagioclase.

The zircons from this sample are mostly subhedral and consist of relatively stubby grains. The dominating portion vary between 100-200 µm in length with an aspect ratio from between 1.2 and 2.5. A few are smaller. The crystals are clear or brown. Inclusions often occur in the zircons, and a few show fracturing. In CL imaging, the zircons are dominated by dark, oscillatory domains with thin, irregular, highly luminescent rims (Fig. 5.2.9A). Some show structureless or partly oscillatory zoned cores. A few zircons show some convolute zoning (Fig.5.2.9A). One zircon shows a partly oscillatory zoned core (spot 8.1) with a structureless overgrowth (spot 8.2) (Fig.5.2.9A). Nineteen spots were analyzed on fifteen different grains. Fourteen of the analyses were done on oscillatory domains, including one core (spot 13.1) surrounded by a partly convolute and oscillatory zoned overgrowth. Four analyses were done on highly luminescent rims, and one on a structureless overgrowth (spot 8.2). The fourteen oscillatory domains have U concentration that ranges between 155-1380 ppm (average=478 ppm), and the Th/U ratio vary between 0.13 and 2.55 (average=0.65), (Appendix 1). The U concentration from the rim analyses ranges between 185-1053 ppm (average=532 ppm), and the Th/U ratio vary between 0.38 and 0.04 (spot 2.1) (average=0.16). For the structureless domain, spot 8.2, the U concentration is at 665 ppm and the Th/U ratio at 0.07, indicating a possible metamorphic domain. Three analyses (spot 11.2, 6.1, and 3.2) were removed from further calculation due to significant analytical errors. One older age, spot 13.1, is likely to be an inherited age (Fig.5.2.9B). A total of fourteen analyses give a Discordia line with an upper intercept age at 1625±16 Ma and a lower intercept age at 1032±100 Ma (Fig.5.2.9B). The upper intercept age is interpreted as the best estimate for the igneous crystallization age for this granitic augen-gneiss protolith, while the lower intercept age is interpreted as the age of a metamorphic overprint.

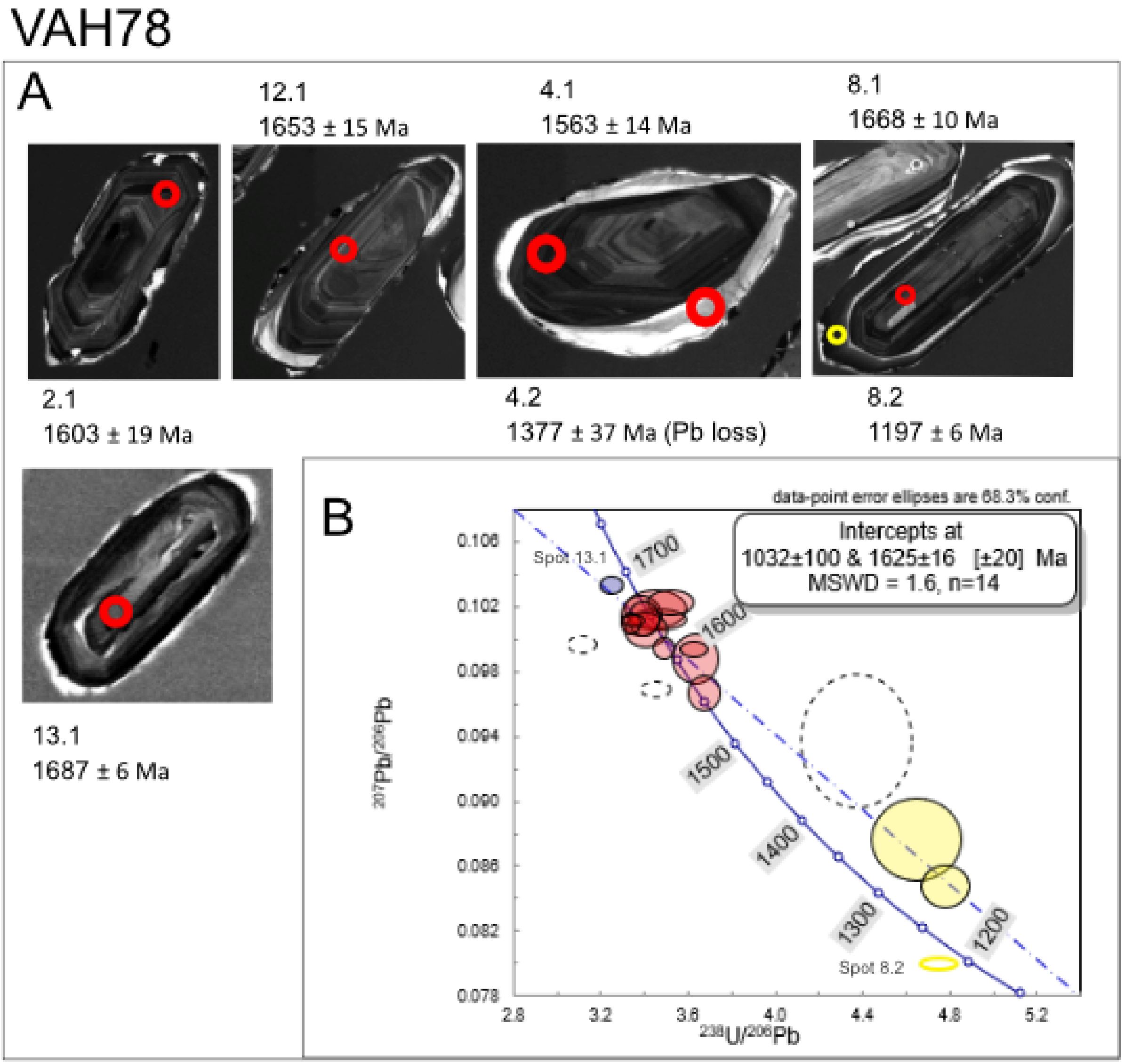

Figure 5.2.9: Results of sample VAH78: (A) Representative CL-images with $^{207}Pb/^{206}Pb$ ages of the analyzed zircons. Analyses without description are concordant analyses. Red circles mark the analyzed spots with a diameter of ca. 20µm. (B) Terra-Wasserburg plot of all the analyses. All analyses are corrected data, and the error ellipses are plotted at the 1σ level. Spot 13.1 (dark blue), most likely to be an inherited age are not included in the calculations.

5.2.4 Sample VAH04, monzonitic augen gneiss, Oldedalen

This granitic augen-gneiss (Fig.5.2.10A) was sampled at Oldedalen, the inner part of Nordfjord (Fig.5.2.1). The rock is moderately deformed and shows a porphyritic texture (Fig.5.2.10B). Coarse-grained K-feldspar augen are surrounded by a fine-grained matrix (Fig.5.2.10C-D) dominated by plagioclase, quartz, green-beige biotite, K-feldspar, and epidote. Carbonates and plagioclase are present in smaller amounts (Fig.5.2.10E). Accessory minerals are zircons, titanites (Fig.5.2.10C-D), apatite, and opaque minerals. The K-feldspar eyes have cracks, usually filled by carbonates (Fig.5.2.10E), but also sometimes smaller feldspar grains. Some of the K-feldspar are characterized by cross-hatch twinning, indicating microcline. Albite twinning is shown in some of the plagioclase. Some of the feldspars grains have perthitic (Fig.5.2.10F) and myrmekitic texture. The epidotes are usually found together with biotite, and often shows harlequin colours. A few of the carbonates show an indication of rhombohedral cleavage, indicating calcite, while the rest shows the recognizable twinkling while rotating. The recrystallized quartz shows polygonal till lobate grains boundaries and undulose extinction. The feldspars, mostly the plagioclases, show strong sericitization (Fig.5.2.10E), and some also show saussuritization. Several biotites have been retrogressed to chlorite. The sericitization and saussuritization, as well as the presence of chlorite, indicate hydrothermal alteration of the rock.

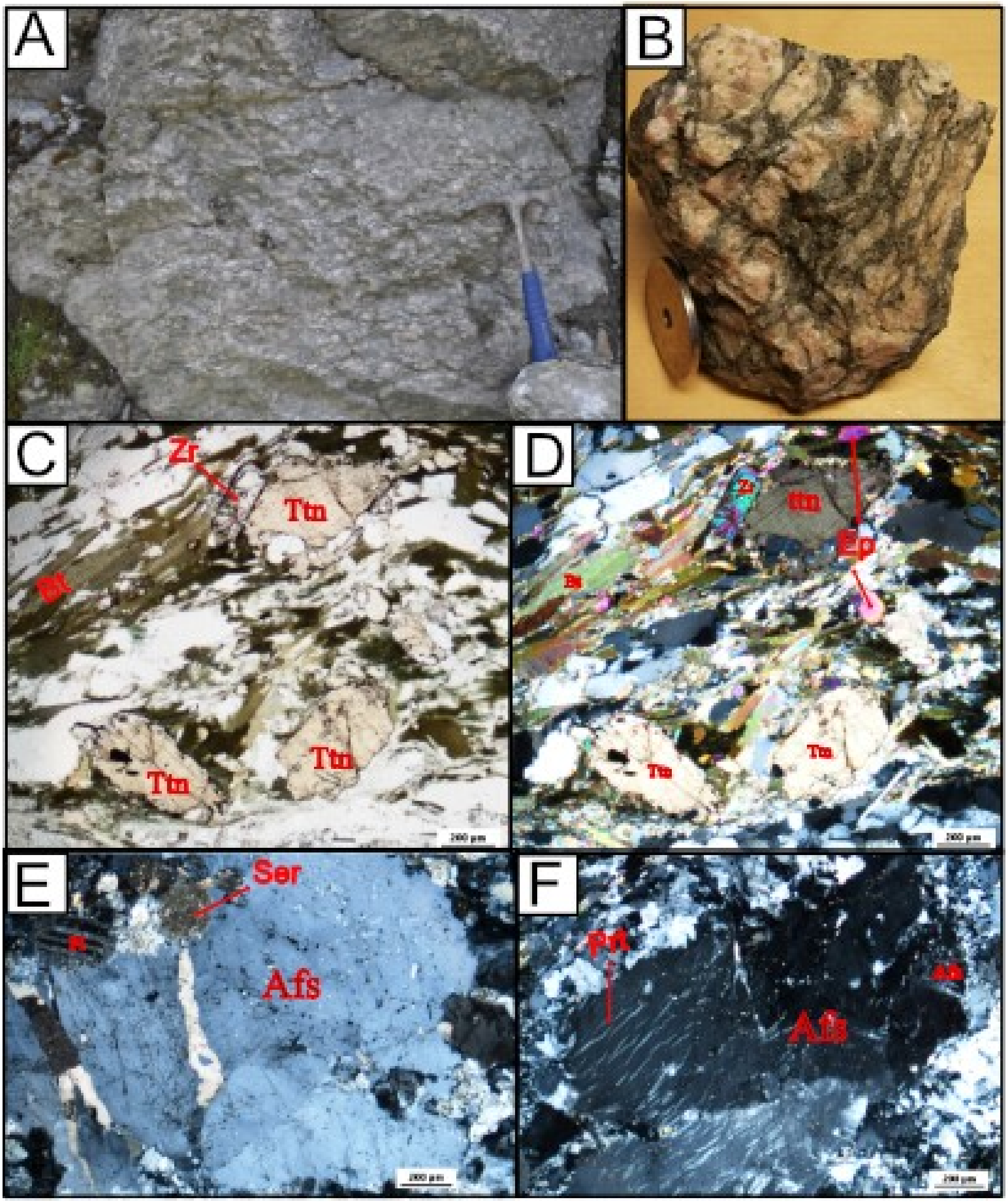

Figure 5.2.10: (A) Field photograph of locality VAH04 (Photo: Åse Hestnes). (B) Sample VAH04. (C) Titanite, biotite, and epidote commonly occur together. The white minerals are quartz and feldspar. (D) Titanite, biotite, and epidote in XPL. (E) K-feldspar augen with carbonate filled in cracks. Sericitized plagioclase and K-feldspar are common. (F) Perthitic unmixing in the K-feldspar eye. Some K-feldspars show cross-hatch twinning.

The zircons from this sample are subhedral to euhedral and consist of both elongated and some more stubby grains. They are usually around 200 µm long but vary between 100-300 µm with an aspect ratio between 2 and 3.5. The crystals are either clear or more light brown. Many of the zircons have inclusions, are fractured and some appear as fragments. In CL imaging, the zircons are dominated by oscillatory zoning (Fig.5.2.11A). Another characteristic feature, on many of the zircons, is thin, irregular, bright-coloured rims that are too thin to be analyzed (zircon 7 and 9, Fig.5.2.11A). A few zircons show convolute zoned cores (Zircon 10, Fig.5.2.11A). Twelve spots were analyzed on twelve different grains, all from oscillatory zoned domains. The U concentrations range between 62-194 ppm (average=115 ppm) (Appendix 1), and the Th/U ratios vary between 0.83 and 1.81 (Average = 1.32). Two analyses (spot 9.1 and 6.1) were excluded from further calculations due to Pb loss and high revers discordance (-14%) respectively. A total of ten analyses give a common Concordia age of 963 ±7 Ma (Fig.5.2.11B) and a weighted mean ^{206}Pb/^{238}U age at 962 ±7 Ma (Fig.5.2.11C). The ages are identical within the error limits and are interpreted as the igneous crystallization age of this monzonitic augen-gneiss protolith.

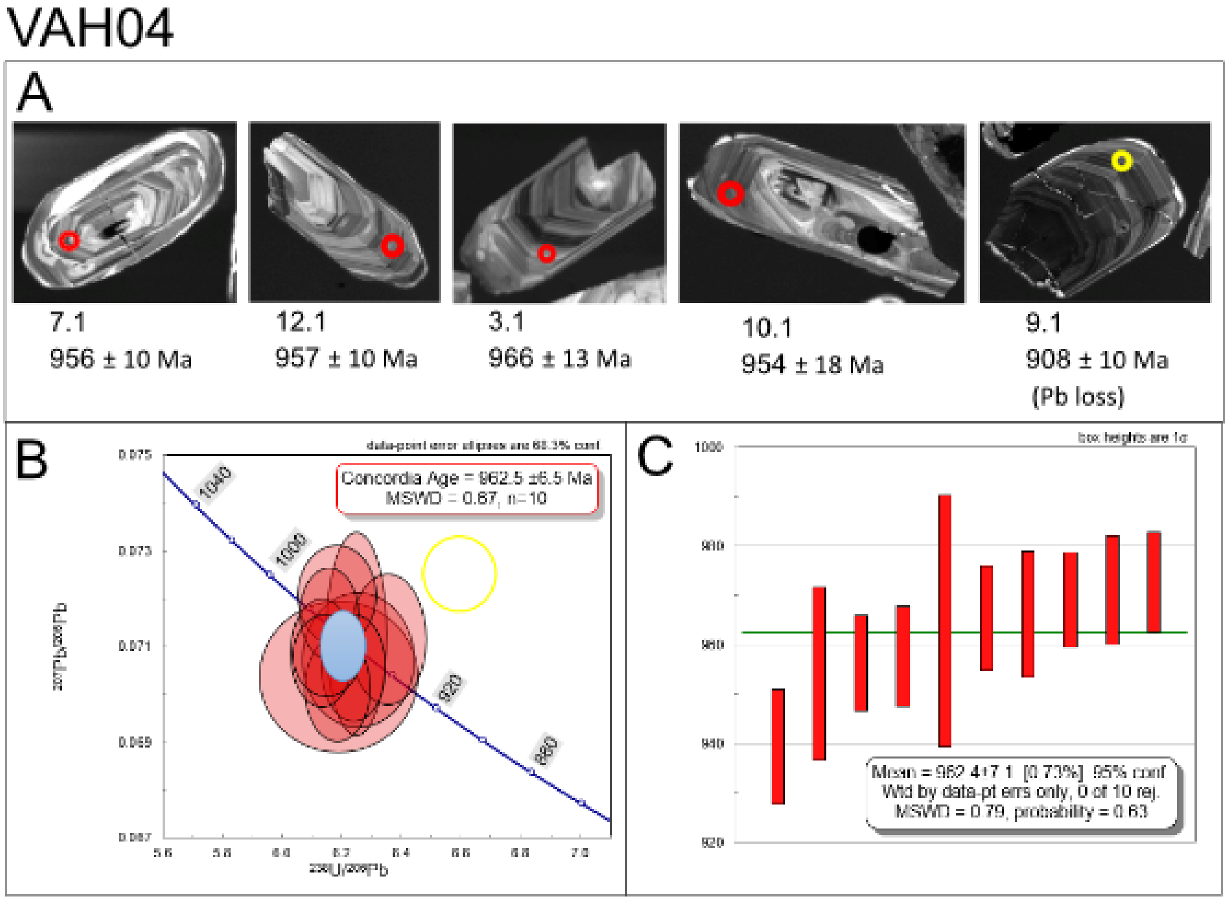

Figure 5.2.11: Results of sample VAH04: (A) Representative CL-images with ^{206}Pb/^{238}U ages of the analyzed zircons. Analyses without description are concordant analyses. Red circles mark the analyzed spot with a diameter of ca. 20 µm. (B) Terra-Wasserburg plot of all the analyses, except for one analysis (spot 6.1) which was excluded due to large analytical error. All analyses are uncorrected data and the error ellipses are plotted at 1σ the level. The Concordia age (blue) is given with 2σ errors. (C) Weighted mean ^{206}Pb/^{238}U of the concordant ages (n=10). Box hight is at 1σ.

5.2.5 Sample VAH11, monzonitic augen gneiss, Loen

This monzonitic augen-gneiss (Fig.5.2.12A) was sampled at mount Skåla in Loen (Fig.5.2.1). The rock shows a porphyritic texture with coarse-grained K-feldspar augen surrounded by a fine-grained matrix (Fig.5.2.12B). Biotite, plagioclase, quartz, epidote and K-feldspar dominates the matrix (Fig.5.2.12C-D). Accessory minerals are titanites, zircons, opaque minerals, and apatite. At the boundaries to the K-feldspar eyes, plagioclase grains with myrmekitic texture often occur, as well as some quartz grains. The epidotes are usually found together with biotite, and often show harlequin colour. The recrystallized quartz shows polygonal to lobate grain boundary and undulose extinction. The plagioclase shows strong sericitization and some saussuritization, while the K-feldspar eyes show weak sericitization. A few biotites have partly retrogressed to chlorite.

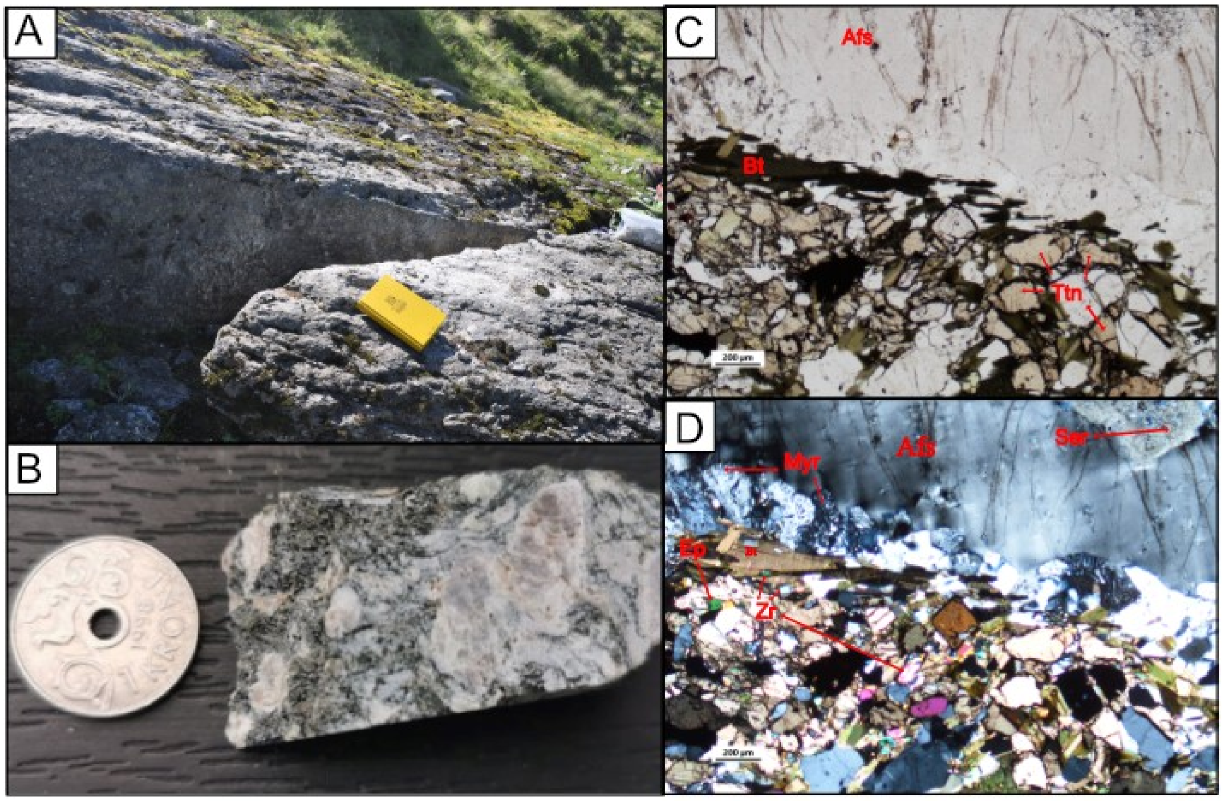

Figure 5.2.12: (A) Field photograph of locality VAH11 (photo: Åse Hestnes). (B) Sample VAH11. (C) K-feldspar augen with fine-grained matrix in PPL. Feldspar, quartz, biotite, and epidote dominates the matrix. (D) Myrmekitic texture in the feldspars that surround the K-feldspar augen.

The zircons from this sample are subhedral to euhedral and consist of mostly elongated grains. They vary in size and range up to 250 µm with an aspect ratio between 2.5 and 3. The crystals are transparent with a tint of brown. Most of the zircons have several inclusions, and few of the grains are fractured. In CL-imaging reveals mostly oscillatory zoning (Fig.5.2.13A). Thin, irregular, highly luminescent rims are another characteristic for many of the zircons. Some of the grains also show tendencies to convolute zoning within the core. Sixteen spots were analyzed on fifteen different grains, all from oscillatory zoned domains. The U-concentrations range between 47-197 ppm (average=114ppm) (Appendix 1), and the Th/U ratio vary between 0.88 and 2.14 (Average=1.28). Five analyses (spot 2.1, 3.1, 7.1, 9.1, and 14.1) were excluded from further calculation due to high reverse discordance (>5%). Two more analyses (Spot 4.1 and 4.2) were also excluded from further calculations, due to Pb loss. A total of nine analyses give a common Concordia age of 958±7 Ma (Fig.5.2.13B) and a weighted mean $^{206}Pb/^{238}U$ age at 960±7 Ma (Fig.5.2.13C). The ages are identical within the error limits and are interpreted as the best estimated igneous crystallization age of this monzonitic augen-gneiss protolith.

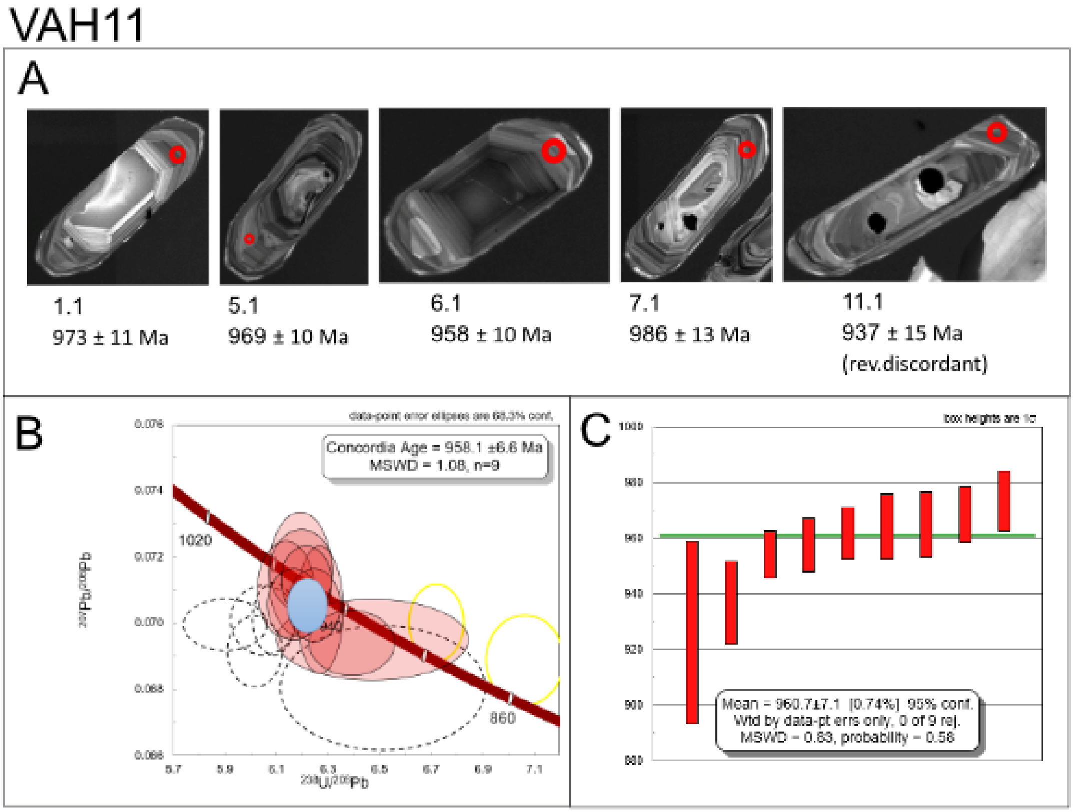

Figure 5.2.13: Results of sample VAH11: (A) Representative CL-images with $^{206}Pb/^{238}U$ ages of the analyzed zircons. Analyses without description are concordant analyses. Red circled mark the analyses spot with a diameter at ca. 20 µm. (B) Terra-Wasserburg plot of all the analyses. All analyses are corrected data, and error ellipses are plotted at the 1σ level. The Concordia age (blue) is given with 2σ errors. (C) Weighted mean $^{206}Pb/^{238}U$ of the concordant ages (n=9). Box hight is at 1σ.

5.2.6 Sample VAH23, granitic banded augen gneiss, Florø

This granitic augen-gneiss (Fig.5.2.14A) is well exposed and was sampled right by the Florø coast-museum (Fig.5.2.1). The rock is moderately deformed and consists of K-feldspar rich bands and augen. The general texture is porphyritic with medium to coarse-grained feldspar augen and a fine-grained matrix (Fig.5.2.14B). Quartz, K-feldspar, plagioclase, epidote, biotite and chlorite and/or talc dominates the matrix. (Fig.5.2.14C-D). Accessory minerals are titanites, opaque minerals and zircons (Fig.5.2.14C-D). The feldspar eyes consist of both plagioclase grains with albite twinning and K-feldspar grains with no twinning, often together in one augen (Fig.5.2.14E). The K-feldspar often show perthitic unmixing (Fig.5.2.14F). Some of the feldspars in the matrix show Carlsbad twinning, while others show no twinning (Fig.5.2.14D). Green-beige biotites, aggregates of epidotes, chlorite and/or talc, and titanites are usually found together. Recrystallized quartz shows polygonal boundaries and undulose extinction. The feldspar shows sericitization and saussuritization (Fig.5.2.14F) and many of the biotites have retrogressed to chlorite.

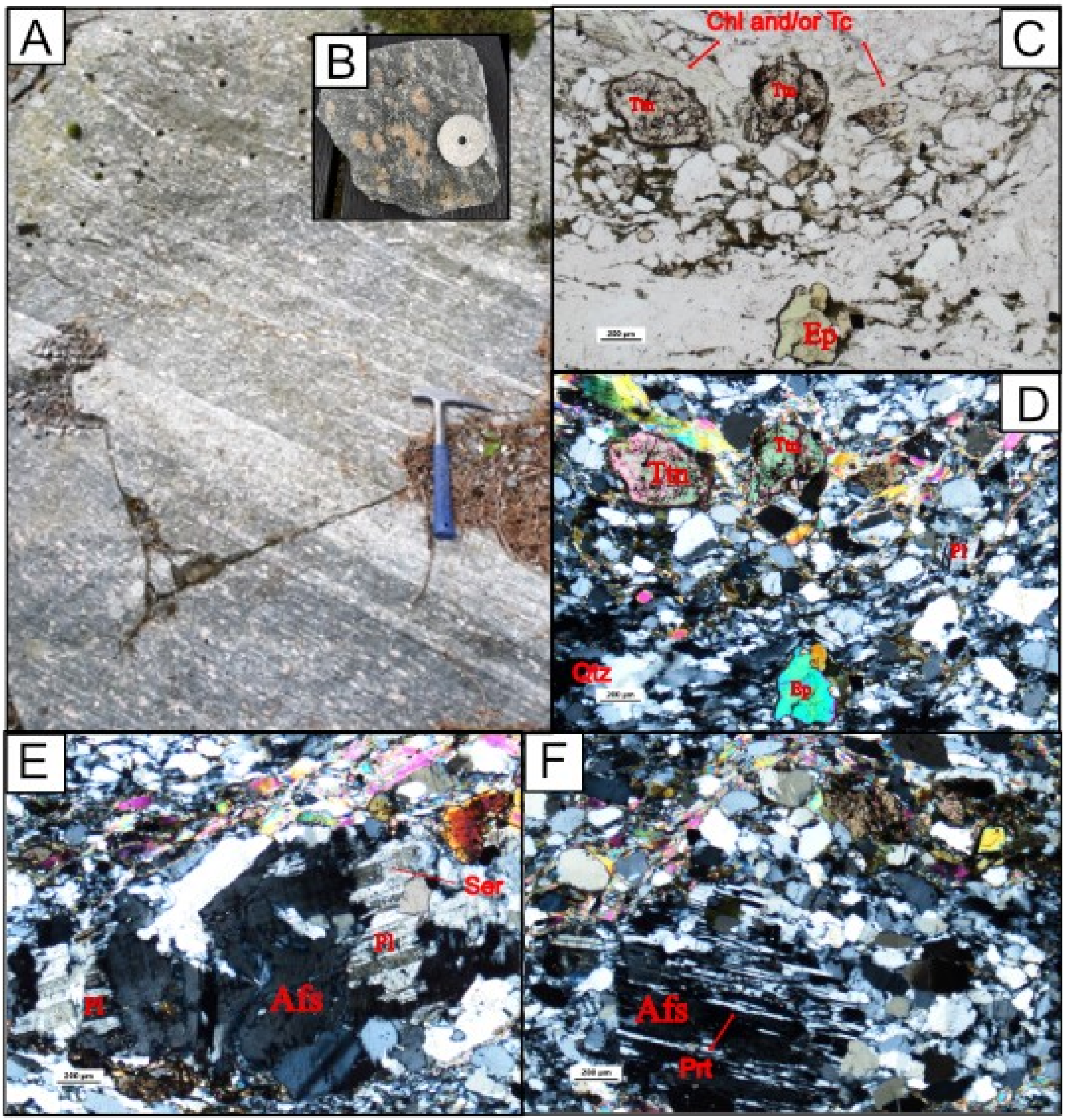

Figure 5.2.14: (A) Field photograph of locality VAH23. (B) Sample VAH23. (C) Biotite, epidote, titanites, and chlorite and/or talc are often found together. The white minerals are quartz, K-feldspar and plagioclase. Seen in PPL. (D) Biotite, epidote, titanite, chlorite and/or talk, K-feldspar, plagioclase, and quartz in XPL. Carlsbad twinning are often seen. (E) Feldspar augen with perthitic unmixing. (F) Augen with several K-feldspar and plagioclase where the plagioclase shows sericitization.

The zircons from this sample are mostly subhedral and consist of relatively stubby grains and a few elongated grains. They vary between 100-250 µm in length with an aspect ratio ranging between 2-5, dominating at around 2.3. The crystals are either clear, light brown or dark brown. There are inclusions in most of the zircons, some are fractures, and a few appear as fragments. In CL- imaging, oscillatory zoning dominates (Fig.5.2.15A), including some with zones parallel to c-axis (spot 9.1). A large portion of the zircons shows thin, irregular, highly luminescent rims. Convolute zoning is shown partly in the core of few zircons (spot 15.1 and 10.1). There is a large contrast between high and low luminescent domains represented in CL-imaging. Seventeen spots were analyzed on sixteen different zircons, all from oscillatory zoned domains. The U concentrations range between 15-394ppm (average=113ppm) but dominates between 40-130ppm (Appendix 1). The Th/U ratios vary between 0.93 and 1.76 (Average=1.28). Nine analyses (spot 1.1, 2.1, 4.1, 5.1, 7.1, 8.2, 12.1 and 16.1) were excluded from further calculation due to reverse discordance (>5%), while one analyzed (spot 10.1) was excluded from further calculations due to Pb loss. A total of seven analyses give a common Concordia age of 942±9 Ma (Fig. 5.2.15B) and a weighted mean $^{206}Pb/^{238}U$ age at 945±10 Ma (Fig.5.2.15C). The individual analyses are identical within the error limits and are interpreted as the best estimated igneous crystallization age of the protolith to this granitic gneiss.

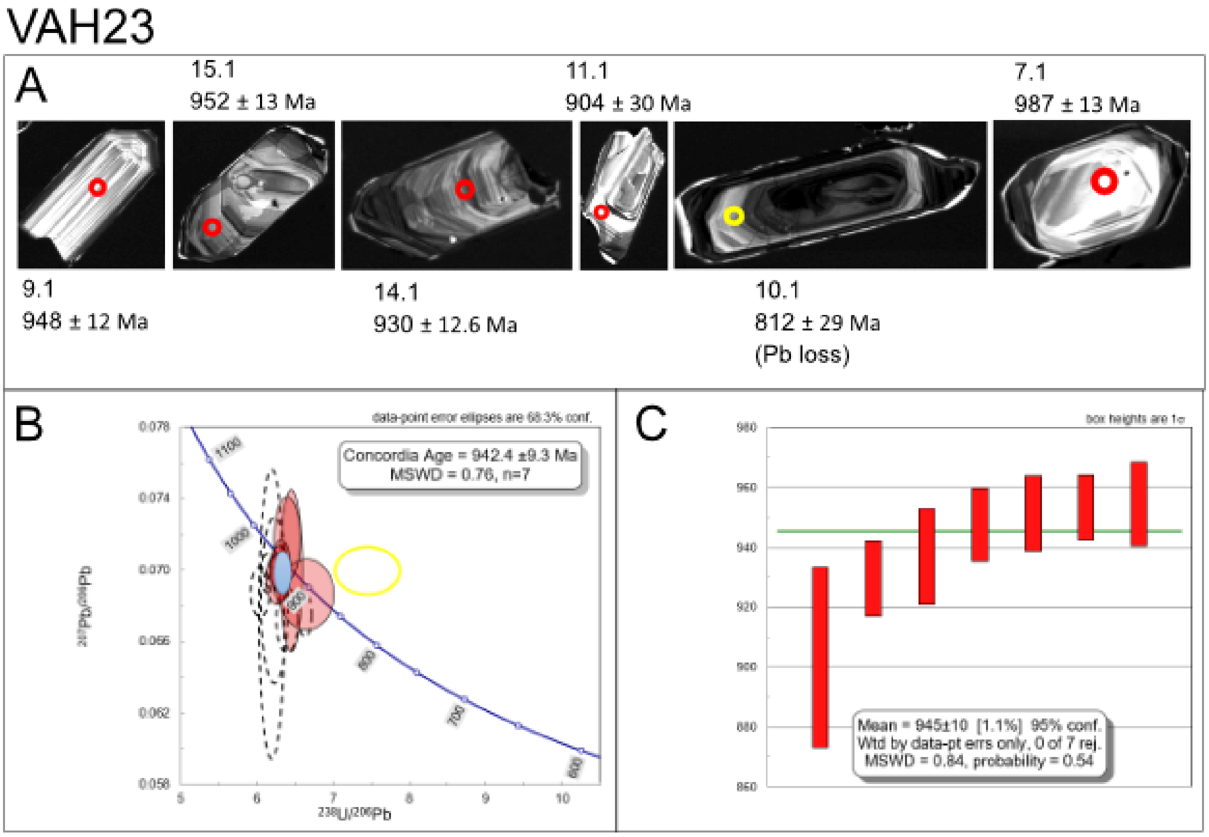

Figure 5.2.15: Results of sample VAH23: (A) Representative CL-images with ^{206}Pb/^{238}U ages of the analyzed zircons. Analyses without description are concordant analyses. Red circles mark the analyzed spot with a diameter of ca. 20 µm. (B)Terra-Wasserburg plot of all the analyses, except for two analyses (spot 12.1 and 16.1), which were excluded due to large analytical error (> 70% and 27% respectively). All analyses are corrected data, error ellipses plotted at 1σ level. The Concordia age (blue) is given with 2σ errors. (C) Weighted mean 206Pb/238U of the concordant ages (n=7). Box hight at 1σ.

5.2.8 Sample VAH31, muscovite-granitic gneiss, Hyen

This granitic gneiss (Fig.5.2.16A-B) was sampled at Hyen, at a small peninsula in the fjord (Fig.5.2.1). The rock is highly fractured and strongly deformed. Medium K-feldspar eyes are surrounded by a fine-grained matrix dominated by quartz, muscovite, epidote, plagioclase, biotite, K-feldspar, and chlorite (Fig.5.2.16C-D). Accessory minerals are titanite, clinozoizite[1], zircons, and apatite (Fig.5.2.16E-F). Some of the K-feldspar are characterized by cross-hatch twinning, indicating microcline. Albite twinning occurs in some of the plagioclase. Perthitic unmixing is seen in some feldspars. Mineral x, titanite and epidote are often found in clusters (Fig.5.2.16E-F). The quartz shows lobate grain boundaries and undulose extinction and partly appears as ribbon quartz (Fig.5.2.16G). The feldspars show saussuritization and sericitization and are often found as smaller, recrystallized grains. Several biotites have regressed to chlorite.

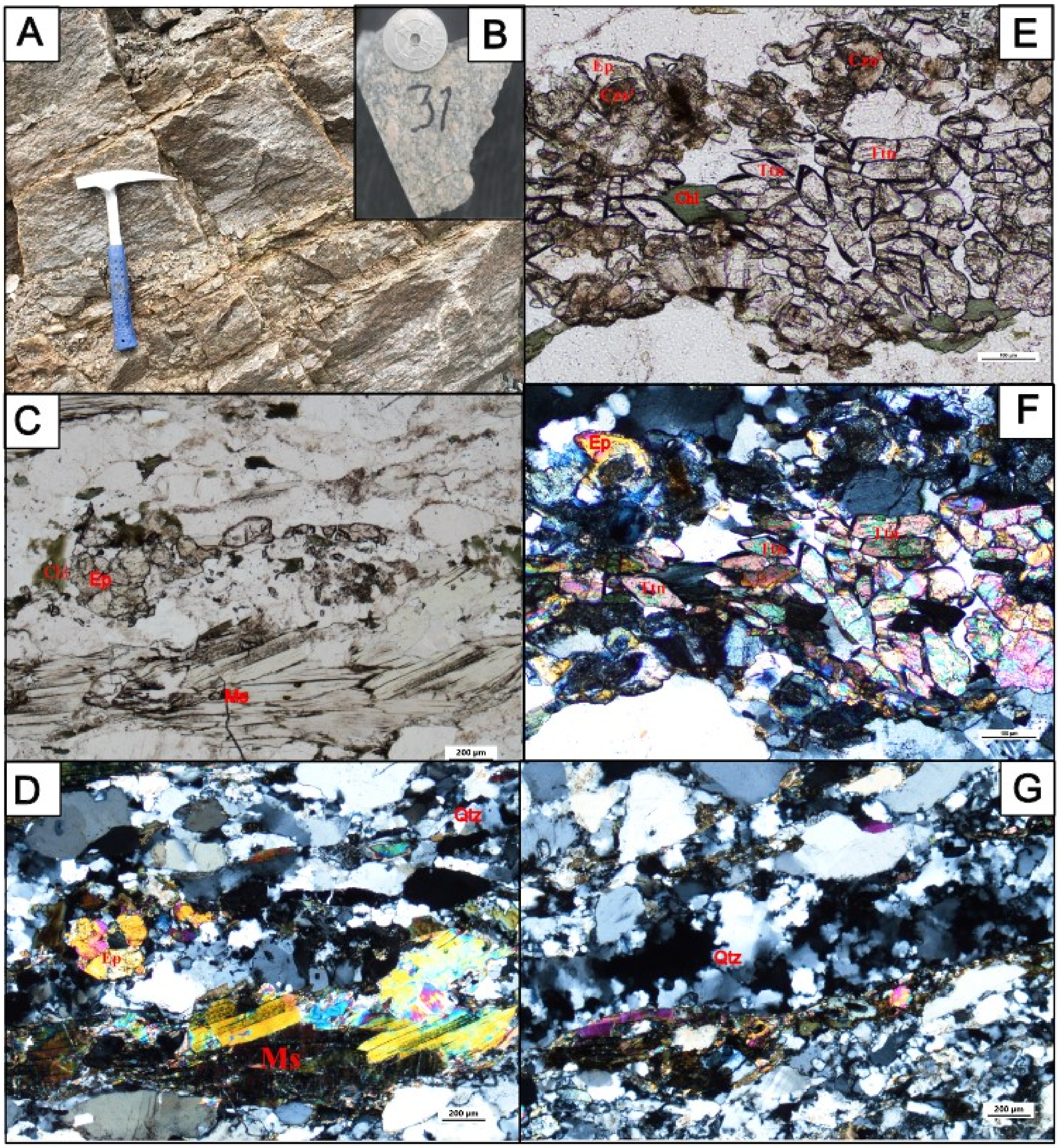

Figure 5.2.16: (A) Field photograph from locality VAH31. (B) Sample VAH31. (C) Muscovite, chlorite, epidote, and titanite in PPL. White minerals are quartz and feldspars. (D) Muscovite, quartz, chlorite, epidote, titanite, and feldspar in XPL. (E) Clusters of clinozoizite[1], titanite together with some epidote and chlorite in PPL. Clinozoizite[1] shows strong alteration and are often surrounded by epidote rims. (F) Clusters of clinozoizite[1], titanite together with some epidote and chlorite in XPL. (G) Ribbon quartz.

The zircons from this sample are subhedral to euhedral with rounded edges and consist of both stubby and more elongated grains. They are between 100-200 µm in length with an aspect ratio ranging between 2.3 and 5.6. Most of the crystals are medium to dark brown, and a few are clear. Inclusions are common, some show fracturing, and a few occur as fragments. In CL imaging, oscillatory zoning is dominating the zircons (Fig.5.2.17A). Some of the zircon cores are metamict and show mottled texture in CL (spot 1.1, Fig.5.2.17A). Texture-less cores of both high and low luminescence are also observed. Some show tendencies to convolute zoning. Thin, irregular, highly luminescent rims are common. Twelve spots were analyzed on twelve different grains, all oscillatory zoned domains. The U concentration range between 244-982 ppm (average=657 ppm) (appendix 1), and the Th/U ratios vary between 0.44 and 2.59 (average=1.16). Two analysis (spot 10.1 and 3.1) were excluded due to significant high analytical error. The ten remaining analyses give a Discordia line with an upper intercept age at 928 ± 44 Ma when anchored at 400 ± 10 Ma (Fig.5.2.17B). Two analyses (spot 6.1 and 7.1) are concordant but do not reflect the crystallization age of this protolith. They are interpreted to have undergone concealed lead loss (e.g. Andersen et al., 2019). The upper intercept age is the best estimated for the igneous crystallization age for this granitic augen-gneiss protolith, while the lower intercept age is interpreted as the age of a metamorphic overprint.

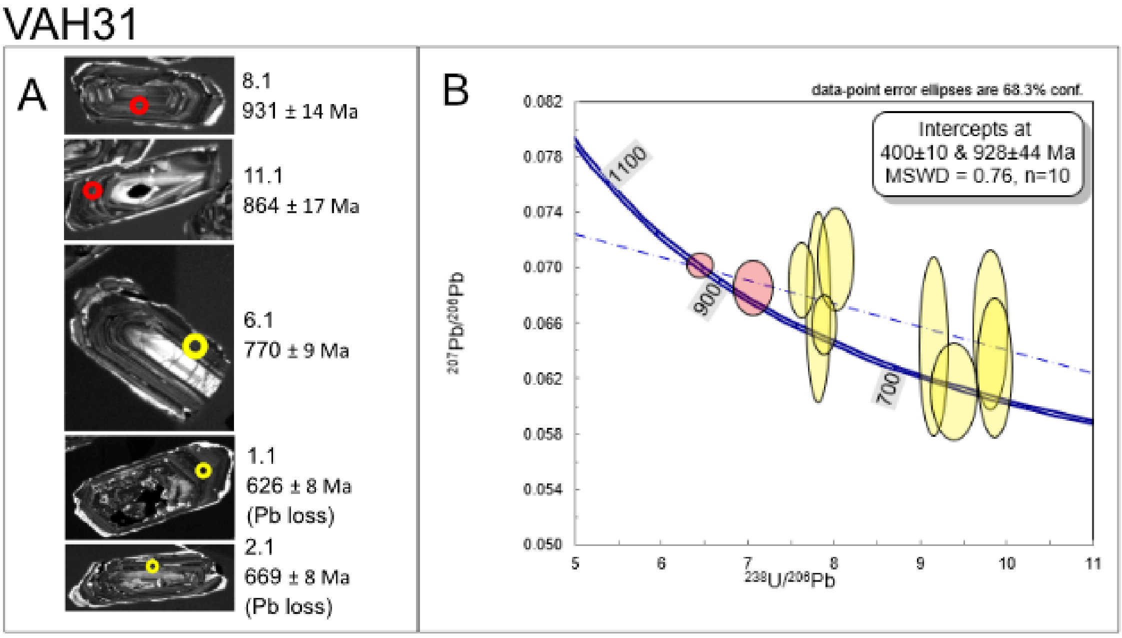

Figure 5.2.17: Results of sample VAH31: (A) Representative CL-images with 206Pb/238U ages of the analyzed zircons. Analyses without description are concordant analyses. Red/yellow circles mark the analyzed spot with a diameter of ca. 20µm. (B) A Terra-Wasserburg plot of all the analysis, except for two analysis (spot 10.1 and 3.1) which were excluded due to high analytical errors. All analyses are corrected data, and the error ellipses are plotted at 1σ level.

5.2.7 Sample VAH44, granitic augen gneiss, Maurstad

This granitic augen gneiss (Fig.5.2.19A) was sampled at Maurstad, Bruggja (Fig.5.2.1), at a well exposed, heterogenous outcrop along a sharp curve by the main road. The outcrop can generally be described as a banded gneiss with a dioritic composition with amphibolite lenses (Fig.5.2.18). One pegmatitic dike is present with diffuse transition to the surrounding rock, and a anorthosite body with amphibolitic boudinage is seen. In some places the texture is more augen gneiss, and the K-feldspar content varies. Sample VAH44 is taken from the most K-feldspar rich zone in this outcrop, making it more granitic in composition.

The sampled granitic augen gneiss shows a porphyritic texture with K-feldspar augen and bands, surrounded by a fine-grained matrix. Quartz, brown-beige biotite, K-feldspar, plagioclase and chlorite dominate the matrix (Fig.5.2.19B-D). Smaller amounts of muscovite also occur. Accessory minerals are titanites, zircons, opaques, and apatite (Fig.5.2.19B,D). The dominating portion of the K-feldspars is characterized by cross-hatch twinning, indicating microcline. Albite twinning is shown in the plagioclase. Myrmekitic texture is common in the smaller feldspar grains, and some of the larger K-feldspar also show perthitic texture. Biotite, muscovite, and titanite are usually found together. Some of the titanites show the characteristic diamond shape (Fig.5.2.19C). The chlorite is found typically found together with biotite and opaques and form an eye shape (Fig.5.2.19C-D). The quartz shows polygonal to lobate grain boundaries and undulose extinction, and partly appears as ribbon quartz (Fig.5.2.19B). Some of the feldspars show saussuritization and sericitization.

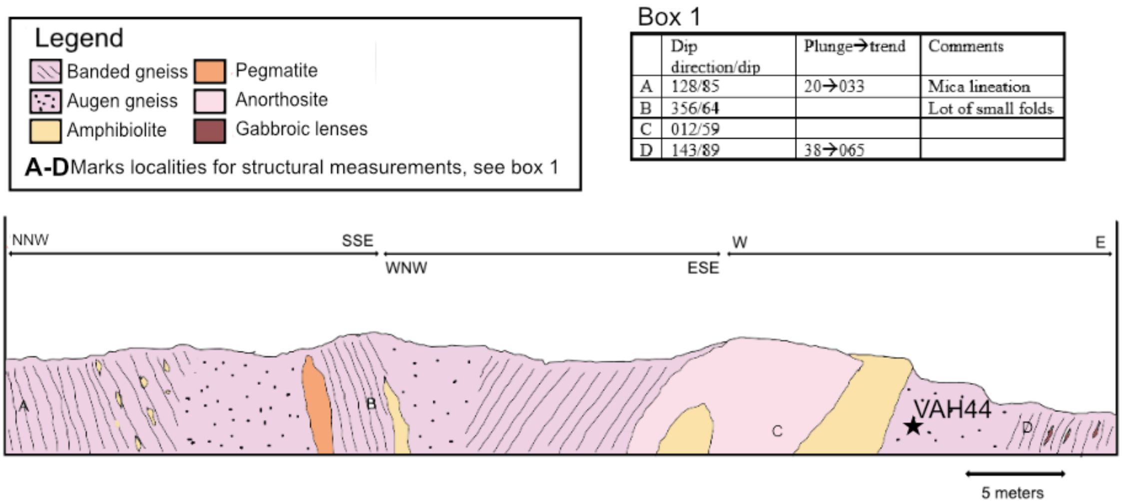

Box 1

	Dip direction/dip	Plunge→trend	Comments
A	128/85	20→033	Mica lineation
B	356/64		Lot of small folds
C	012/59		
D	143/89	38→065	

Figure 5.2.18: Simplified cross section of the heterogenous outcrop at Maurstad. The outcrop shows banded gneiss with a dioritic composition intercalated with amphibolite lenses. Sample VAH44 (marked with a star symbol) is from this outcrop where the K-feldspar content is higher compared to the rest of the outcrop.

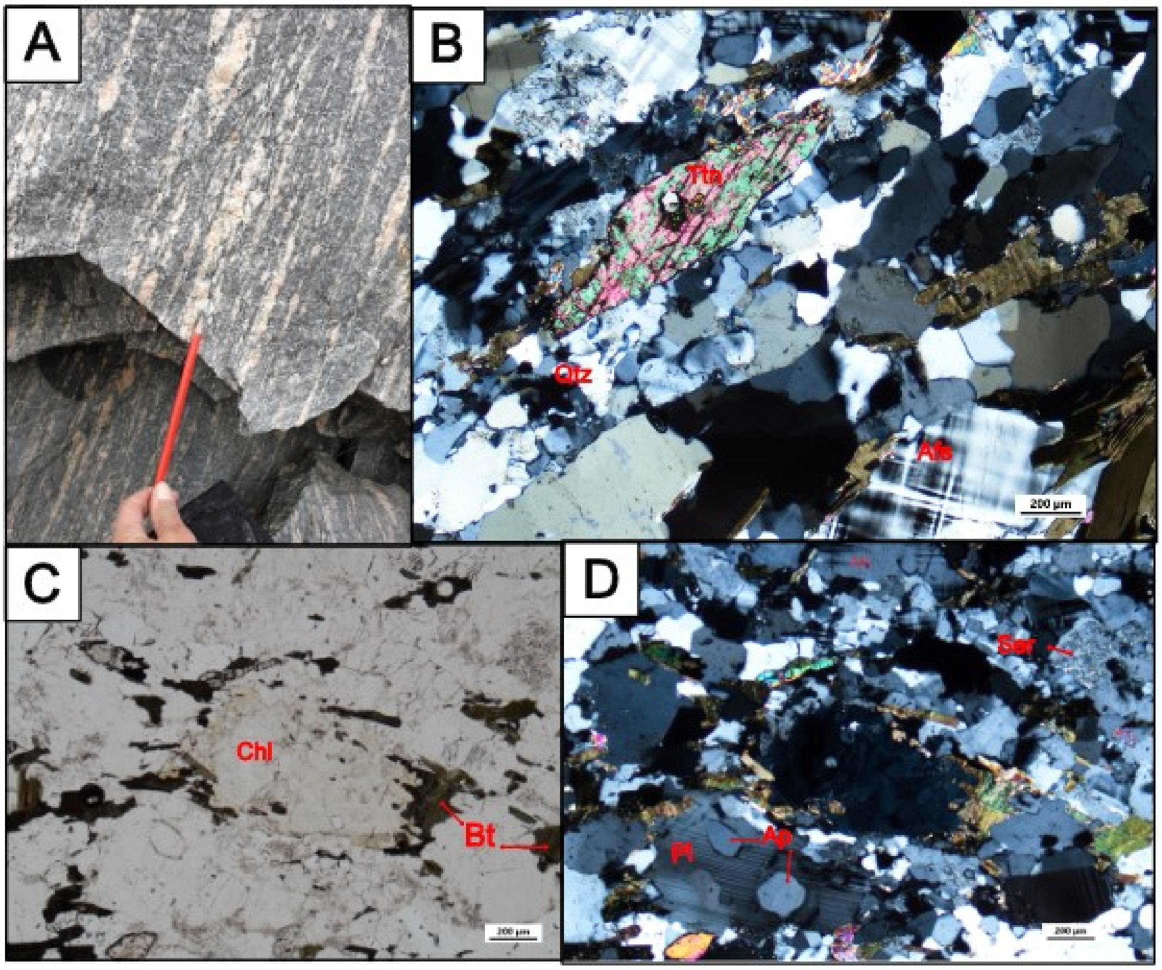

Figure 5.2.19: (A) Field photograph from locality VAH44. (B) Quartz, biotite, K-feldspar, and titanite in XPL. Muscovite show typically cross-hatch twinning. (C) Chlorite is shaped like an eye together with biotite in PPL. (D) The chlorite eye in XPL. Large apatite grains and albite twinning in plagioclase in XPL. Sericitization occurs.

The zircons from this sample are subhedral to euhedral, and both elongated and stubby grains occur. The length of the zircons ranges from 100-300µm with an aspect ratio between 1.8 and 4. The crystals are light and dark brown. Many of the zircons have inclusions, and some are fractured. In CL imaging, the zircons are dominated by a highly luminescent cores surrounded by low luminescent overgrowths (Fig.5.2.20A). Both these domains vary between weak oscillatory zoning and structureless textures. Some of the zircons only have low luminescent domains. Another characteristic is the thin, irregular, highly luminescent rims. Nineteen spots were analyzed on sixteen different grains. Ten of these are core analyses, six from the low luminescent domains, and three are from the thin, irregular highly luminescent rims. The cores have U concentration range between 42-687 ppm (average=407ppm) (Appendix 1), and the Th/U ratios vary from 0.50 and 1.05 (average=0.68). Three analyses (spots 9.1, 8.1 and 3.1) from this domain reveals Pb-loss. For the dark luminescence domains, the U concentration range between 872-4561 ppm (average=2219), and the Th/U ratios vary from 0.004 and 0.01 with one analysis (spot 14.1) with a Th/U ratio at 0.31. For the white rims, the U concentrations range between 277-2535 ppm (average= 1360), and Th/U ratios vary from 0.002 and 0.01. Five analyses (spot 6.1, 6.2, 11.1, 5.1, and 13.1) were removed from further calculations due to high reverse discordance. A total of five analyses, from low luminescent domains and high luminescent rims, give a common Concordia age at 412±4 Ma (Fig.5.2.20B) and a weighted mean $^{206}Pb/^{238}U$ age at 413±4 Ma (Fig.5.2.20C). A total of fourteen analyses from all domains give a Discordia line, anchored at 412±4 Ma, with an upper intercept age at 904±21Ma (Fig.5.2.20D). The common Concordia age and weighted mean $^{206}Pb/^{238}U$ age are identical within the error limits and are interpreted as the best estimated metamorphic overprint age for this granitic gneiss. The upper intercept age is interpreted as the best estimate for the igneous crystallization age of the protolith to this granitic gneiss.

VAH44

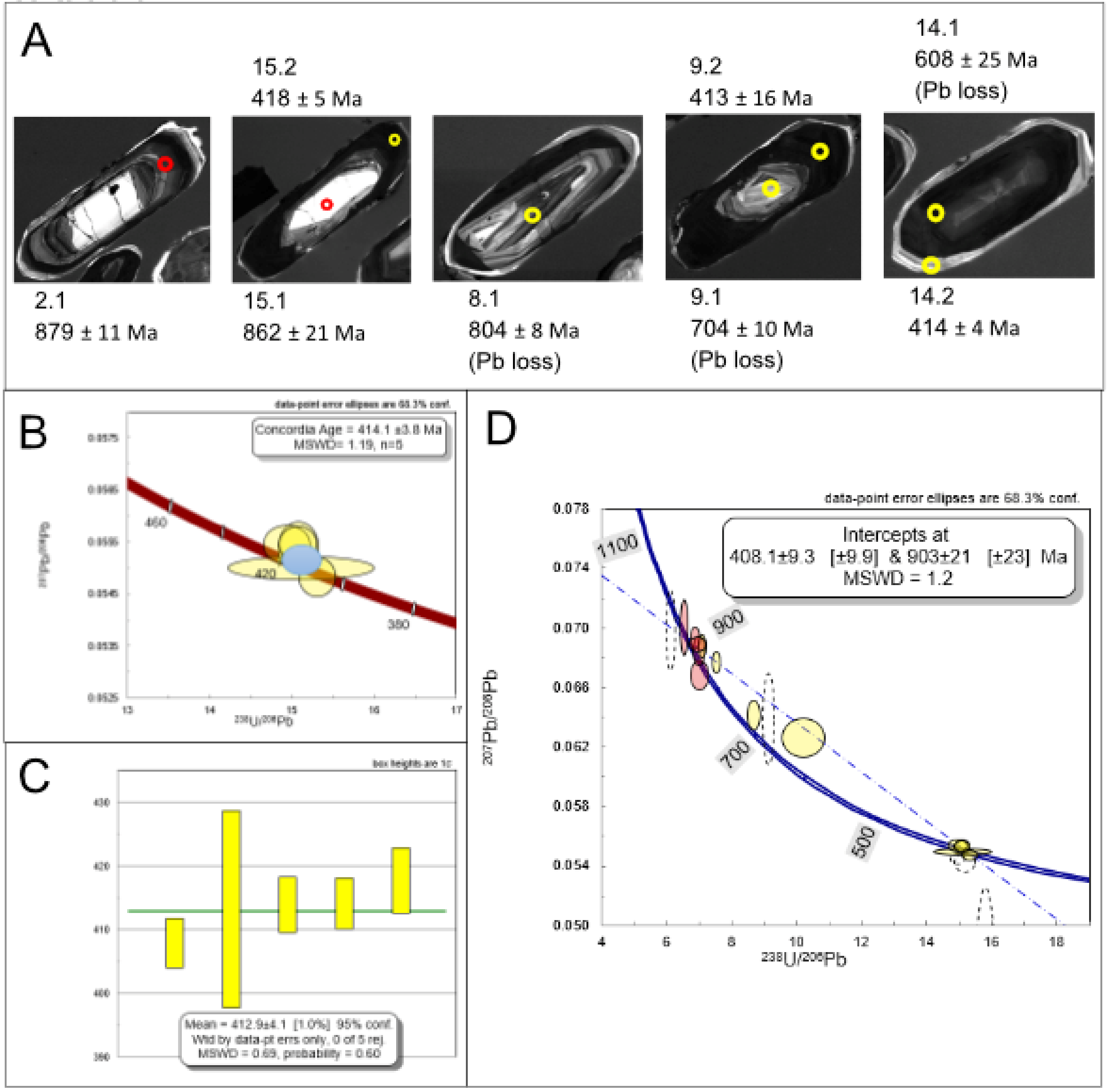

Figure 5.2.20: Results of sample VAH44: (A)Representative CL-images with $^{206}Pb/^{238}U$ ages of the analyzed zircons. Analyses without description are concordant analyses. Red and yellow circles mark the analyzed spot with a diameter of ca. 20µm. (B) Terra-Wasserburg plot of five concordant analyses. The error ellipses are plotted at the 1σ level. The Concordia age (blue) are given with 2σ error. (C) Weighted mean $^{206}Pb/^{238}U$ of the five concordant ages in (B). Box hight is at 1σ. (D) A Terra-Wasserburg plot of all the analyses with a Discordia line. All analyses are corrected data, and the error ellipses are plotted at the 1σ level.

Summary

The U-Pb geochronological data are summarized in Fig.5.2.21. The three oldest concordant ages were calculated at 1651±7 Ma, 1627±18 Ma and, 1625±16 Ma, while the younger concordant ages were calculated at 963±7 Ma, 958±7 Ma, 942±9 Ma, 928±44 Ma and, 903±21 Ma. The observed textures and U/Th ratios are typically for magmatic zircons and the ages are therefore interpreted as the igneous crystallization ages for these protoliths. One sample, VAH78 gave a concordant age at 1687±6 Ma, representing a possible inherited age. Four of the samples gave lower intercept ages at 1050±110 Ma, 1032±100 Ma, 400±10 Ma and, 408±9 M, representing possible metamorphic overprint. The two older, lower intercept ages are represented with a higher uncertainty compared to the two younger ones.

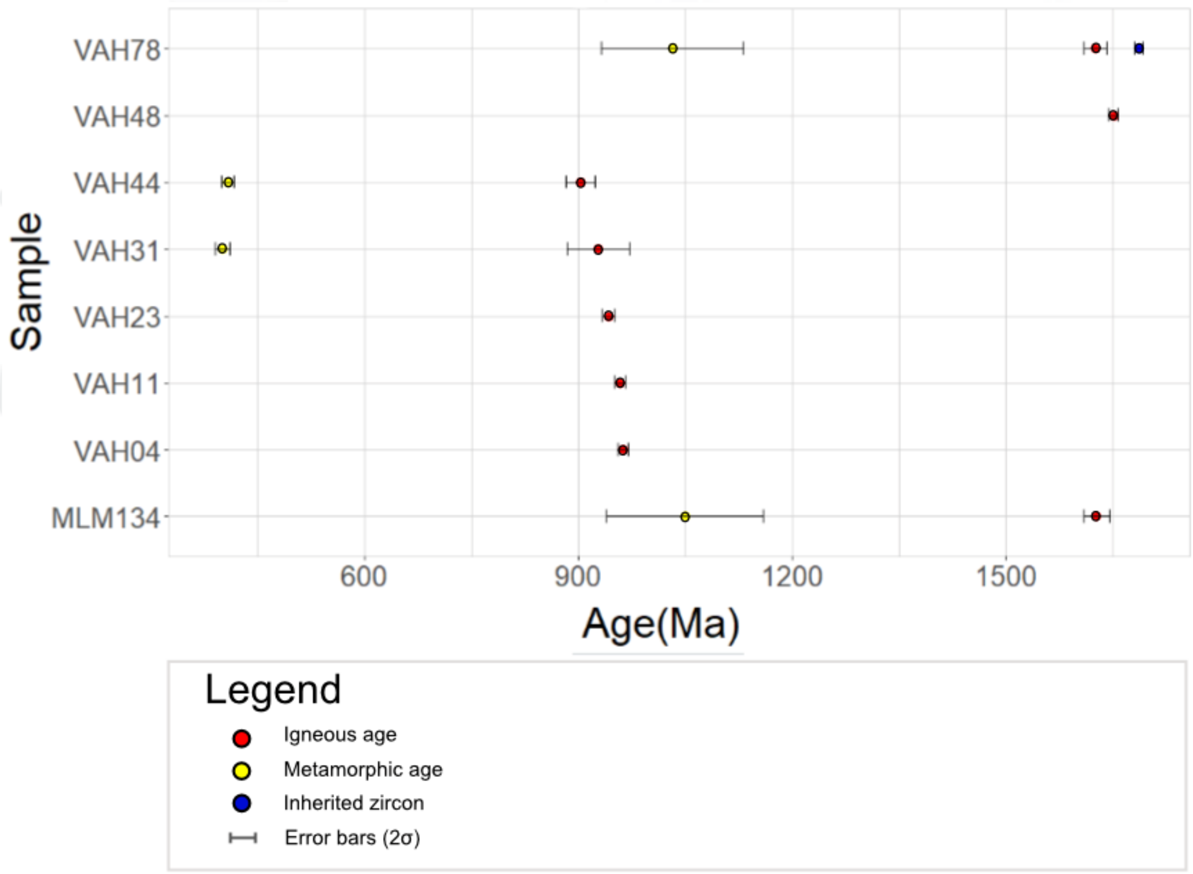

Fig.5.2.21: Summary of geochronological data. The data falls into three main groups.

Chapter 6: Discussion

In this chapter, the results will be discussed. First, the U-Pb zircon geochronology and petrological results for the eight studied samples will be compared to each other and grouped based on their ages. The ages correlate to either Gothian crystallization ages, Sveconorwegian metamorphic ages, Sveconorwegian crystallization ages, and Caledonian metamorphic ages. Second, each group's data will be discussed together with previous work and the regional geological development. Thirdly, the monzonitic unit's development on Måløy will be addressed. That will be based on previous studies and the new geochronological dating from this study. Lastly, the Sveconorwegian orogeny and how the findings in this study support the different developments for the Sveconorwegian orogeny will be addressed.

6.1 Comparing the U-Pb datasets and samples to each other

The study (Fig.1) aimed to investigate if the Sveconorwegian magmatism could be traced further north into the Nordfjord region, western Norway. The data reveals U-Pb ages that can be correlated to all three major orogenic events that have affected Norway's development. Gothian-age magmatism is reported in three samples, VAH48, MLM134, and VAH78. Two of these samples, MLM134 and VAH78, show evidence of a metamorphic overprint that correlates to the Sveconorwegian orogeny. The metamorphic related ages from these two samples are constrained with high uncertainty. The remaining five samples, VAH04, VAH11, VAH23, VAH31, and VAH44, reveal Sveconorwegian-age magmatism. The Sveconorwegian magmatic ages somewhat correlate with the Sveconorwegian metamorphic ages but show a slightly younger trend. VAH31 and VAH44 show a high 2σ error but overlap the Sveconorwegian magmatic ages within the uncertainty. These two samples show lower intercept ages, interpreted as metamorphic overprints, that correlates to the Caledonian orogeny. A higher certainty is demonstrated in these two Caledonian metamorphic ages compared to the Sveconorwegian metamorphic ages. The strong Caledonian overprint in sample VAH31 and VAH44 can explain the relative higher uncertainty of their igneous crystallization ages than the other Sveconorwegian samples that don't show strong evidence for this metamorphic overprint.

All samples show a granitic to monzonitic composition comprising of K-feldspar, quartz, and plagioclase. Biotite, epidote, titanite, and zircon occur in all samples at varying degrees. Some also contain muscovite. The clinozoisite[1]occur in the oldest rocks and the two youngest rocks, highly affected by a Caledonian overprint, indicating a possible metamorphic relevance. The degree of quartz recrystallization varies in the different samples. Perthitic and myrmekitic textures are seen in the Sveconorwegian protolith-aged samples. A variable amount of sericite and saussuritizite, and chlorite appear in all samples and reflect a retrogression in hydrothermal environments.

Besides sample MLM134, a similar texture with K-feldspar augen surrounded by a granoblastic textured matrix represents all samples. Together with the mineral assemblage, that indicates at least amphibolite facies metamorphism. Sample MLM134 shows a more mylonitic deformation texture. The mylonitic texture is due to high-T shearing represented at the tectonic contact located only half a meter from were the sample is taken. Sample MLM134 also reveals a more complex zircon texture that may indicate a more complex deformation history. The garnet content can also represent residues of a previous granulite facies metamorphism (see below for a discussion of Måløy¨s development). In addition, sample VAH48 contains large scapolite that is not observed in any of the other samples. Scapolite is associated with granitic pegmatites and regional metamorphism (Deer et al., 2013).

6.1.1 Gothian magmatism

The three oldest samples, VAH48, MLM134, and VAH78, are interpreted to reflect Gothian crustal growth. VAH48 shows a slightly higher crystallization age at 1651±7 compared to MLM134 and VAH78 with crystallization ages of 1627±18 and 1625±16, respectively, that falls within each other's error limits. The protolith ages constrained from these three samples show strong similarities with the existing literature of Gothian protolith ages for the basement in both the study area and the whole WGR (Tucker et al., 1990; Skar et al., 1994, Skar 2000; Austrheim et al., 2003; Corfu et al., 2014b) (Fig.2.7, Fig.2.10). All three samples, VAH48, VAH134, VAH78, are strongly deformed and have probably undergone several deformational events. The geochronological data for sample MLM134 and VAH78 give information about the timing for one of the possible metamorphic events.

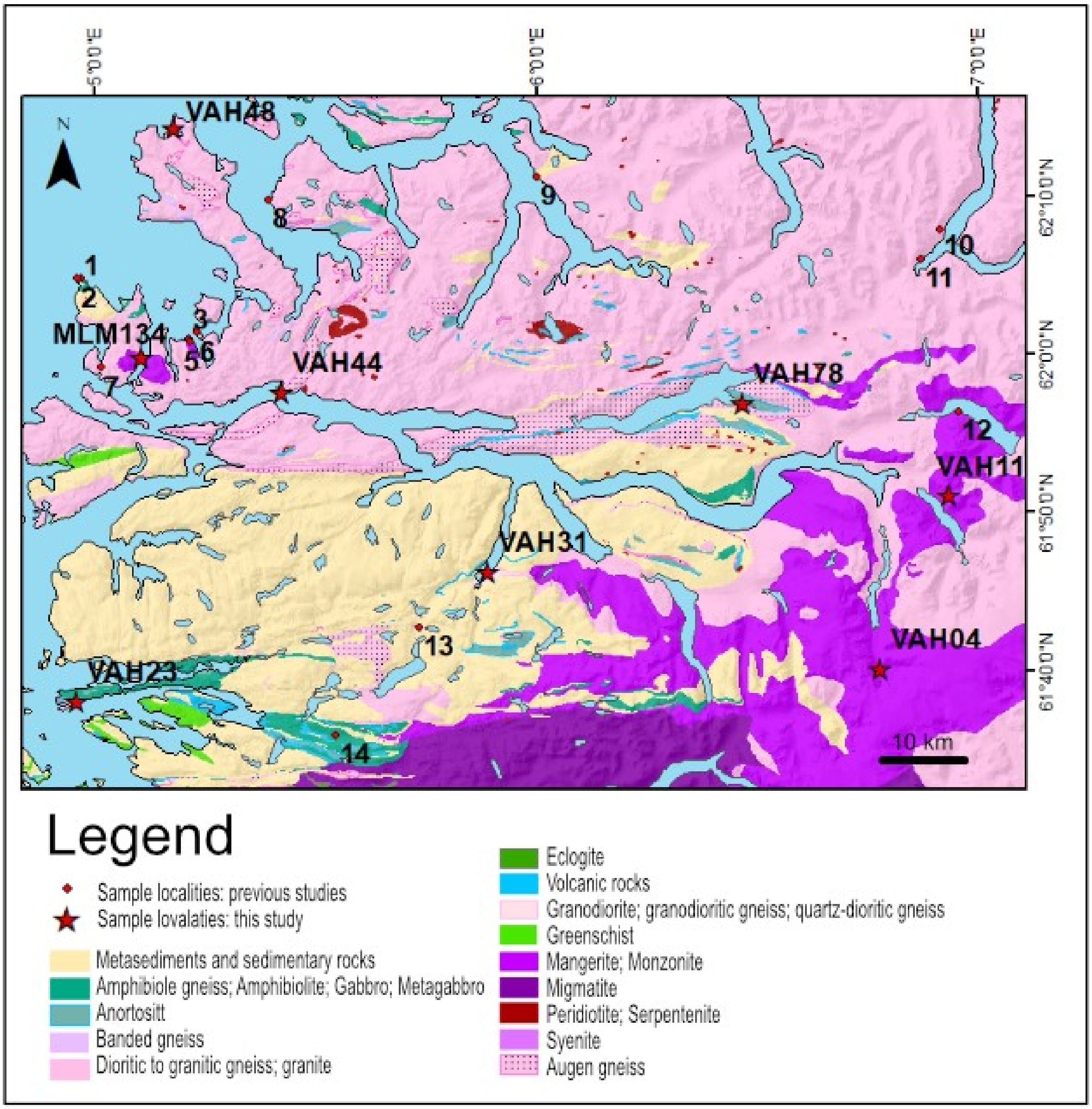

Figure 6.1: Simplified geological map with the previous U-Pb dated sample localities (see figure 2.10) and the sample localities from this study.

6.1.2 Sveconorwegian metamorphism

The lower intercept ages of the two samples MLM134 and VAH78, at 1050±110 Ma and 1032±100 Ma respectively, are interpreted to reflect a metamorphic overprint related to the Sveconorwegian orogeny (1.15-0.9 Ga). The presence of ribbon quartz indicates at least amphibolite facies metamorphic conditions. A high 2σ error represented in the ages makes is possible to correlate them to a number of representative metamorphic overprint ages in the study area. The metamorphic overprint represented in the Flaktraket monzonite (1093±8 Ma), Flaktraket granulite (1108± 12 Ma), Kråkeneset granite (ca 1100 Ma) (Corfu et al., 2014b), one pegmatitic dike (962±9 Ma) (Skar and Slagstad, 2003), and an amphibolite gneiss (990±3Ma) (Corfu and Andersen, 2016) correlates with the Sveconorwegian metamorphic overprint in this study (Fig.2.10). Corfu et al. (2014b) interpret the metamorphic event as a localized granulite facies metamorphism. Due to no evidence for significant plutonism to correlate to this metamorphic event, either at Flaktraket or the entire WGR, the localized granulite metamorphism was thought to be caused by CO_2- and S-bearing fluid (Corfu et al., 2014b).

6.1.3 Sveconorwegian magmatism

A total of five samples show igneous protolith ages that overlap with the known range of Sveconorwegian magmatism summarized by Slagstad et al. (2018), (Fig.6.2). All five samples correlate with the HBG magmatism (Fig.6.2). Three of the samples, VAH04, VAH11, and VAH23, also can be associated with the major peak of the HBG magmatism (Fig.6.2), where sample VAH23 also correlates to the peak magmatism in the Rogaland Igneous Complex (RIC). Sample VAH31 and VAH44 can be related to both the end of the HBG magmatism, but also to the RIC magmatism (Fig.6.2).

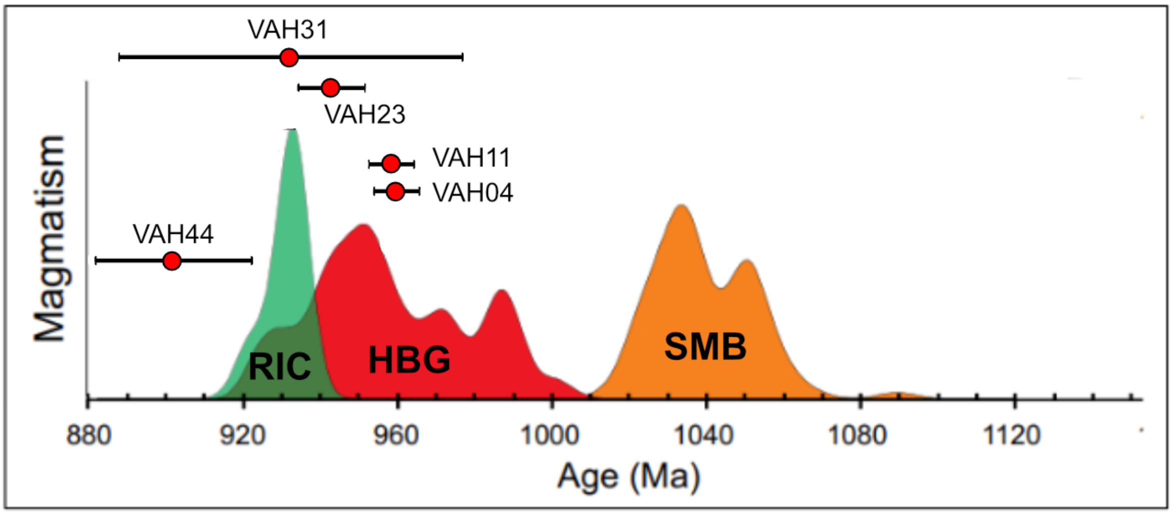

Figure 6.2: The main magmatic events reflecting the magmatic development for the Sveconorwegian orogeny after Slagstad et al. (2018), together with the new geochronological data presented in this study. The ages show 2σ errors.

In the SE part of the study area (Fig.6.1), a sizeable monzonitic body is mapped. Sample VAH04 (963±7 Ma) and VAH11(958±7 Ma) are from different parts of this body (Fig.6.1). The monzonitic body stretches further south from the study area were the Jølster granite dated at 966±2 Ma is located (Skar and Pedersen, 2003). The Jølster granite dated is a coarse-grained porphyritic quartz syenite (Skar and Pedersen, 2003). The similar composition for the two samples, VAH04 and VAH11, correlates with the sample dated by Skar and Pedersen (2003). All three ages, sample VAH04, VAH11(this study) and the Jølster granite (dated by Skar and Pedersen, 2003) falls within each other's error limits and give a relatively precise age of about 960 Ma for this monzonitic body. It can therefore be interpreted as one large pluton.

The crystallization age for the sizeable monzonitic body can be associated with the HBG suite (Fig.6.2). The ferroan HBG suite represents widespread magmatism of a monzodioritic/quartz-monzodioritc to granitic composition (Auwera et al., 2008; Slagstad et al., 2018). The magmatic activity for the HBG suite reveals a prominent peak around 950 Ma (Slagstad et a., 2018) (Fig.6.2). The monzonitic pluton appears to have crystallized shortly before the HBG magmatism peaked (Fig.6.2). The monzonitic pluton is the largest mapped in the WGR (Skar and Pedersen, 2003) and exceeds any of the mapped HBG plutons in southern Norway (Slagstad et al., 2018) in size.

The crystallization age of sample VAH23 also shows similarities to the HBG suite, but the sample also correlates in age to the Rogaland igneous complex magmatism. The Rogaland igneous complex is separated into two different units, the Rogaland Anorthosite Province and the Bjerkreim-Sokndal layered intrusion, which both are interpreted to have the same age (Slagstad et al., 2018). The complex is placed far SSW in Norway and is, in whole, described as an anorthosite-mangerite-charnockite suite (Auwere et al., 2003). The granitic composition of VAH23 better correlates with the HBG suite.

The two youngest samples, VAH31 and VAH44, also show crystallization ages that correlate to both the HBG suite and the Rogaland igneous complex (Fig.6.2). Both have the same granitic composition as sample VAH23, an indication that a correlation with the HBG suite is the better fit. The large error in VAH31 makes it possible to correlate the crystallization age to both the main magmatic activity and the end of the HBG period with less magmatic activity. Sample VAH44 represents the end of the HBG magmatic period (Fig.6.2).

None of the five samples with HBG-like ages contain hornblende that is characteristic of the HBG suite. This indicates a variation in composition compared to the HBG plutons located in southern Norway. The Sveconorwegian protoliths from this study also reveal a change in composition, of monzonitic to granitic from E to W as well as a younging towards the W. Slagstad et al. (2018) report an east to west change in composition for the HBG rock, regarding the absence of hornblende in the eastern part, signified several groups within the HBG suite. The lack of hornblende is seen in all the samples in this study, which may indicate a different source. The results in this study indicate both a younging towards the west and several groups of HBG magmatic provinces in the Nordfjord area.

6.1.4 Caledonian metamorphism

The two youngest samples with Sveconorwegian protolith ages, described above, are strongly affected by a Caledonian overprint. The two lower intercept ages for VAH31 (400±10 Ma) and VAH44 (408±9 Ma), interpreted to represent a Caledonian metamorphic overprint, falls within each other's error limits. They can possibly be correlated to either the 425-400 Ma UHP-HP event or the 400-380 Ma amphibolite-facies event, both occurring in the Scandian phase of the Caledonian orogeny development (Fig. 2.8) (Hacker et al., 2010). The presence of ribbon quartz and the mineral assemblage in the samples, support at least amphibolite- facies metamorphism. The sample VAH44 falls within the Nordfjord UHP domains (Fig.2.9). Sample VAH44 may therefore best correlate to the UHP-HP event. VAH31 is found outside the UHP-HP domains, but is found in a basement window surrounded by the Devonian basin. This sedimentary basin was deposited during the rapid exhumation of the WGR that resulted in amphibolite-facies metamorphic conditions (Corfu et al., 2014a; Fossen, 2010; Kylander-Clark et al., 2007; Hacker et al., 2010). Sample VAH31 may therefore best correlate to the amphibolite-facies event.

6.2 Age relations on Måløy

The petrological and structural findings on Måløy in this study correspond with previous research on both Måløy and similar monzonitic bodies in the Nordfjord area (Bryhni, 1966; Corfu et al., 2014b; Krabbendam et al., 2000). There is a clear petrological and structural difference between the Måløy monzonite and the surrounding gneiss. In general, the monzonitic body show a different recrystallization, of the mineral assemblage, compared to the granitic to granodioritic gneiss surrounding the monzonitic body.

The monzonitic unit shows strongly recrystalized plagioclase, amphibole and biotite, recrystalized quartz that partly appear as ribbons. This together with small lenses/phorphyroblasts of K-feldspar grains are represented in the unit. Recrystalized quartz without any ribbons present can be seen in the surrounding gneiss. Here, the K-feldspar appear as partly stretched out and as small sigma clasts. The granitic to granodioritic gneiss show a typically gneiss banded deformation with sigma clasts (representing a top to the W/NW movement) presented throughout the rock. The monzonitic unit shows stronger deformation close to the boundary, including some banding and K-feldspar augen (without any clear indicators of movement), but are more massive close to the centre of the unit.

All previous studies agree on granulite-facies metamorphic conditions followed by amphibolite-facies metamorphism (Bryhni, 1966; Corfu et al., 2014b; Krabbendam et al., 2000; This study). Relics of the granulite-facies metamorphism is based on the mineral assemblage of garnet, clinopyroxene, plagioclase, and K-feldspar (Bryhni, 1966). The clinopyroxene is only found in the metagabbro and the eclogite bodies, and not in the monzonitic body in this study. Krabbendam et al. (2000) explain the lack of pyroxene by retrogression to amphibole during the younger amphibolite metamorphism. In contrast the surrounding gneisses show no indications for a previous granulite-facies metamorphism (Bryhni, 1966; Corfu et al., 2014b; Krabbendam et al., 2000; this study). Different interpretations to explain the petrological and structural differences in the two main lithologies and how the monzonitic bodies were emplaced have been given.

Bryhni (1966) correlated the monzonitic body on Måløy and Flaktraket and described them as one originally large body. He explained the differences between the monzonitic body and the surrounding gneisses by interpreting the monzonitic body as an exotic unit that got thrusted on top of the gneisses. The exotic monzonitic body and the event of thrusting was linked to the Jotun nappe (Bryhni, 1966).

In later studies, the monzonitic bodies are interpreted to have intruded the surrounding gneisses (Corfu et al, 2014b; Krabbendam et al., 2000). Krabbendam et al. (2000) Proposed the following development for both the Flaktraket monzonite, the Måløy monzonite (referred to as Ulvesund body by Krabbendam) body and a third body in the area of similar type (Fig.6.3):

1) The intrusion of the monzonitic rocks followed by mafic and intermediate intrusions.
2) A pre-Caledonian granulite facies metamorphism.
3) A peak in Caledonian eclogite facies metamorphism
4) Late Caledonian exhumation with complete retrogression locally preserved in shear zones.

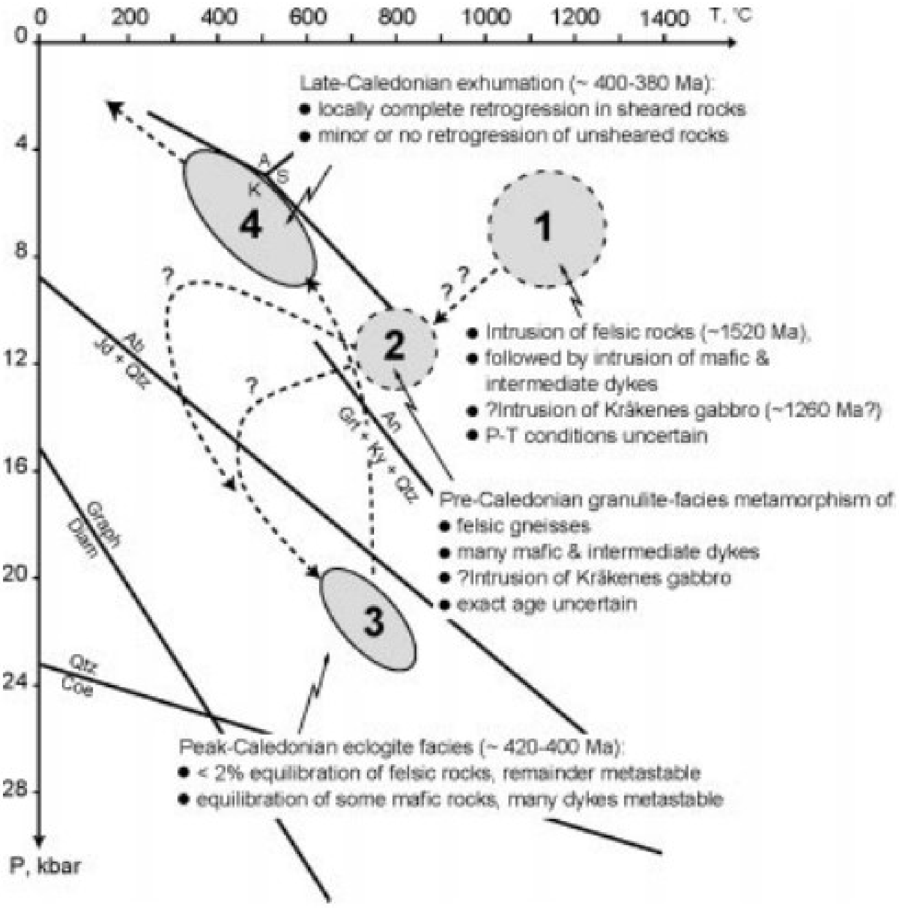

Figure 6.3: A proposed development for the monzonitic bodies at Måløy and Flaktraket and the surroundings by Krabbendam et al. (2000).

The intrusion timing at ca. 1520 Ma is based on the crystallization age for the Flaktraket monzonite dated by Lappin et al. (1979). Later studies showed a much older crystallization age (at 1641±5 Ma) for the Flaktraket monzonite and revealed a lower intercept age interpreted to reflect the timing of the granulite-facies event at 1093±8 Ma (Corfu et al., 2014b).

The Måløy monzonite, represented by MLM134 in this study, reveal an igneous crystallization age of 1627±18 Ma and lower intercept age, interpreted to represent a metamorphic overprint, at 1050±110 Ma. The ages correlate with the crystallization age and timing of granulite-facies event by Corfu et al. (2014b). This correlation strengthens the already correlation between these two monzonitic bodies done by Bryhni (1966) and Krabbendam et al. (2000).

By interpreting the monzonitic bodies as magmatic intrusions, we need another way to explain the differences between these bodies and the surrounding gneiss. Krabbendam et al. (2000) explained this by the robustness of the bodies: the monzonitic bodies are stiffer and show higher resistance to deformation. This robustness can explain the granulite-facies residues. It can also explain why the Måløy monzonite is more strongly deformed and show stronger amphibolite-facies retrogressions close to the margin (weakness zone).

The boundary between the Måløy monzonite and the surrounding gneisses is key to confirm or unconfirm any of the theories. The boundary between the two units was only observed two places in this study. In the southern part, a high-angles fault was found between the metagabbro and the granitic to granodioritic gneiss. This boundary is interpreted as a fault and does not relate to any of the theories. On the northern side, a low angled tectonic contact is found. The mylonitic texture observed in the monzonitic body so close to the boundary (see MLM134) indicate high-T shear deformation. The foliation measured close to the boundary show a steep inclination which is not unlikely within a thrusting environment. The sheared contact is sharp, indicating a previously primary contact. This sheared contact correlates to similar contacts described by Krabbendam et al. (2000).

Krabbendam et al. (2000) linked the observed shear indicators in their studies to the amphibolite facies metamorphism during the Caledonian orogeny's exhumation. The stronger amphibolite retrogression of the monzonitic body closes to the boundary, and the top to the W/NW movement indicators in the granitic to granodioritic gneiss observed in this study, agrees with that correlation.

6.3 Implications for the Sveconorwegian orogeny

This study reveals high-T related Sveconorwegian metamorphism as well as widespread Sveconorwegian magmatism partly affected by a Caledonian overprint in The Nordfjord region.

The granulite-facies metamorphic conditions shown in sample MLM134 and the amphibolite-facies metamorphic conditions represented from VAH78 represent the same event, even though the granulite-facies conditions may only have affected Måløy and the surrounding area. The ages are of high uncertainty, making them difficult to correlate to a specific event. All the metamorphic phases described by Bingen et al. (2008c): Arendal phase (1140-1080 Ma), Agder phase (1050-980 Ma), Falkenberg phase (980-970 Ma), and Dalene phase (970-900 Ma) fall within the error limits for both MLM34 (1050±100 Ma) and VAH78 (1032±110 Ma). Amphibolite-granulite-facies metamorphic conditions are explained for all phases.

Coint et al. (2015) describe a local amphibolite-granulite facies metamorphic event at ca. 1020 Ma. The timing of this correlates well with the Sveconorwegian metamorphic ages from this study. Metamorphic evidence, based on this study and previous dated Sveconorwegian metamorphic overprints, are mostly located at Vågsvåg and Flaktraket, making it very localized. If other Gothian protoliths have experienced the same Sveconorwegian metamorphic overprint as observed in Vågsvåg and Flaktraket can be speculated. But if they have, they only show evidence for the later amphibolite-facies conditions during the Caledonian orogeny.

The source for the metamorphic event represented in sample MLM134 and VAH78 is also difficult to determine based on the high error of the ages. A possibility is to correlate the metamorphic event to the widespread magmatism observed in this study. If so, the metamorphic ages appear to have occurred somewhat previous to the magmatic event in the area. Another possibility is that the metamorphic event can be presumed to have been caused by CO_2- and S-bearing fluid, as previously proposed by Corfu et al. (2014b).

The widespread magmatism correlates to the HBG rocks that are commonly described to represent a re-melting of the lower SMB, as a result of mafic underplating (Slagstad et al., 2018). The revealed variations between the studied HBG related rocks, the absence of the typical hornblende, and these rocks' location compared to the SMB, however reflect a different source.

Skar and Pedersen (2003) interpreted the ca 960 Ma lower interception ages of their studied migmatites and gneisses to reflect a thermal event that resulted in new zircons growth. This can be correlated to the lower intercept Sveconorwegian ages in this study that shows similar age as the widespread magmatism occurring in the area. The source for the high-T Sveconorwegian metamorphism in the Nordfjord area can now be correlated to the widespread magmatism described in this study.

The uncertainty of the Sveconorwegian metamorphic event and its effect on the WGR makes it difficult to support either the high metamorphic continent-continent collision model proposed by Bingen et al. (2008b) nor the all accretionary tectonic model proposed by Slagstad et al. (2013). Regardless, the Sveconorwegian magmatism has also affected the Nordfjord area to a significant degree.

Chapter 7: Conclusion

Based on the U-Pb geochronological and petrological results obtained from this study, I propose the following evolution and implication for the Nordfjord area:

- The oldest rocks show Gothian protolith ages with granitic composition. On Måløy and the surrounding area, monzonitic plutonism with a slightly younger Gothian protolith ages intruded the granitic-granodioritic gneisses.
- A Sveconorwegian metamorphic event overprinted the Gothian protoliths at around 1040±100 Ma under amphibolite-granulite-facies conditons. The extent of how much of the study area was affected by this event is unsure.
- A widespread magmatism, with a composition change from monzonitic in the east to granitic in the west and a younging towards the west, correlates with the Sveconorwegian HBG-rocks in southern Norway. The lack of hornblende in the samples from this study may imply a different source.
- A Caledonian metamophic overprint has affected the rocks to different degrees. The amphibiolite-facies metamophic conditions, related to the Caledonian exhumation, have affetcted all samples. One sample, VAH44 correlates to the Nordfjord UHP-HP domain.

Reference list:

Andersen, T., Elburgb, M. A. & Magwaza, B. N. (2019) Sources of bias in detrital zircon geochronology: Discordance, concealed lead loss and common lead correction. *Earth-Science Reviews.* v.197, 1-15.

Austrheim, H. (1987). Eclogitization of lower crustal granulites by fluid migration through shear zones. *Earth and Planetary Science Letters*. v.81, pp.221–232.

Austrheim, H., Corfu. F., Bryhni, I., and Andersen, T, B. (2003). The Proterozoic Hustad igneous complex: a low strain enclave with a key to the history of the Western Gneiss Region of Norway. *Precambrian Research*. v.120, pp.149-175.

Austrheim, H. and Corfu, F. (2009). Formation of planar deformation features (PDFs) in zircon during coseismic faulting and an evaluation of potential effects on U–Pb systematics. *Chemical Geology*. v. 261, pp. 25-31.

Bingen, B., Andersson, J., Soderlund, U., Moller, C. (2008a). The Mesoproterozoic in the Nordic countries. *Episodes 31*. v.1, pp. 6.

Bingen, B., Austrheim, H., Whitehouse, M. J., and Davis, W. J. (2004). Trace element signature and U–Pb geochronology of eclogite-facies zircon, Bergen Arcs, Caledonides of W Norway. *Contributions to Mineralogy and Petrology*. v. 147, pp. 671–683.

Bingen, B., Davis, W. J., Hamilton, M. A., Engvik, A. K., Stein, H. J., Skar, O., and Nordgulen, O. (2008b). Geochronology of high-grade metamorphism in the Sveconorwegian belt, S. Norway: U-Pb, Th-Pb and Re-Os data. *Norsk Geologisk Tidsskrift.* v. 88, pp. 13.

Bingen, B., Nordgulen, O., and Viola, G. (2008c). A four-phase model for the Sveconorwegian orogeny, SW Scandinavia. *Norsk Geologisk Tidsskrift.* v. 88, pp. 43.

Bingen, B., Skår, Ø., Marker, M., Sigmond, E. M., Nordgulen, Ø., Ragnhildstveit, J., Mansfeld, J., Tucker, R. D., and Liégeois, J.-P. (2005). Timing of continental building in the Sveconorwegian orogen, SW Scandinavia. *Norwegian Journal of Geology.* v. 85, pp. 87–116.

Bingen, B. and Solli, A. (2009). Geochronology of magmatism in the Caledonian and Sveconorwegian belts of Baltica: synopsis for detrital zircon provenance studies. *Norwegian Journal of Geology.* v. 89.

Bogdanova, S.V., Bingen, B., Gorbatschev, R., Kheraskova, T. N., Kozlov, V.I., Puchkov, V.N., and Volozh, Y.A. (2008). The East European Craton (Baltica) before and during the assembly of Rodinia: *Precambrian Research*, v. 160, pp.23–45.

Brewer, T.S., Daly, J. S, Åhall, K-I. (1998). Contrasting magmatic arcs in the Paleoproterozoic of the south-western Baltic Shield: *Precambrian Research.* v. 92, pp. 297-315.

Bryhni, l. 1966: Reconnaissance studies of gneisses, ultra -basites, eclogites and anorthosites in outer Nordfjord, western Norway. *Norges geologiske undersøkelse*. v. 241, pp. 1-68.

Cocks, L.R.M. and Torsvik, T.H. (2002). Earth geography from 500 to 400 million years ago: a faunal and palaeomagnetic review: *Journal of the Geological Society, London*, v. 159, pp.631-644

Coint, N., Slagstad, T., Roberts, N., Marker, M., Røhr, T., and Sørensen, B. E. (2015). The Late Mesoproterozoic Sirdal Magmatic Belt, SW Norway: Relationships between magmatism and metamorphism and implications for Sveconorwegian orogenesis. *Precambrian Research.* v. 265, pp. 57-77.

Corfu, F. and Andersen, T.B. (2016). Proterozoic magmatism in the southern Scandinavian Caledonides, with special reference to the occurrences in the Eikefjord Nappe. *GFF.* v.138, pp.102-114

Corfu, F., Andersen, T.B., and Gasser, D. (2014a). The Scandinavian Caledonides: main features, conceptual advances and critical questions. *Geological Society, London, Special Publications.* v. 390, pp. 9–43.

Corfu, F., Austrheim, H., Ganzhorn, A-C. (2014b). Localized granulite and eclogite facies metamorhisme at Flaktraket and Kråkeneset, Western Gneiss Region: U-Pb data and tectonic implications. *Geological Society, London, Special Publications*. V. 390, pp.425-442.

Corfu, F., Hanchar, J. M., Hoskin, P. W. & Kinny, P. (2003). Atlas of zircon textures. *Reviews in mineralogy and geochemistry*. v. 53, p. 469-500.

Dickin, A. (2005). *Radiogenic isotope geology*. 2nd ed. United States of America, New York: Cambrigde University Press, pp.101-113.

Deer, W. A., Howie, R. A. and Zussman, J. (2013). An introduction to the Rock-Forming Minerals. 3rd ed. London: *The Mineralogical Society*. v. 549.

Fossen, H. (2010). Extensional tectonics in the North Atlantic Caledonides: a regional view. *Geological Society, London, Special Publications.* v. 335, pp. 767–793.

Gee, D. G., Fossen, H., Henriksen, N., and Higgins, A. K. (2008). From the early Paleozoic platforms of Baltica and Laurentia to the Caledonide Orogen of Scandinavia and Greenland. *Episodes. v.* 31, pp. 44–51.

Corfu, F., Hanchar, J. M., Hoskin, P. W. & Kinny, P. 2003. Atlas of zircon textures. *Reviews in mineralogy and geochemistry*, v. 53, p. 469-500.

Gee, D. G., Juhlin, C., Pascal, C. and Robinson, P. 2010. Collisional Orogeny in the Scandinavian Caledonides. *Geologiska Föreningens i Stockholm Förhandlingar*. v. 132, pp. 29-44.

Gjelsvik, T. (1951). Oversikt over bergartene i Sunnmøre og tilgrensende deler av Nordfjord. Med geologisk oversiktskart av Tore Gjelsvik og Chr. C. Gleditsch. *Norges geologiske Undersøkelse*. v. 179.

Guo, S-L, Chen, B-L and Durrani, S.A (2012). Handbook of Radioactivity Analysis. 3rd ed. *Academic Press*. pp. 233-298.

Hacker, B. R., Andersen, T. B., Johnston, S., Kylander-Clark, A. R., Peterman, E. M., Walsh, E. O., and Young, D. (2010). High-temperature deformation during continental-margin subduction & exhumation: The ultrahigh-pressure Western Gneiss Region of Norway. *Tectonophysics.* v. 480, pp. 149–171.

Hogdahl, K., Andersson, U.B., and Eklund, O. (2004). The Transscandinavian Igneous Belt (TIB) in Sweden: A Review of its Character and Evolution: *Geological Survey of Finland Special Paper*. v. 37, pp. 1–125.

Jolivet, L., et al. (2005). Softening trigerred by eclogitization, the first step toward exhumation during continental subduction. *Earth and Planetary Science Letters*. v. 237, pp.532–547.

Kullerud, L., Torudbakken, B.O. and Ilebekk, S. (1986). A compilation of radiometric age determinations from the Western Gneiss Region, South Norway. *Norges geologiske undersokelse Bulletin*. v. 406, pp.17-42.

Kylander-Clark, A.R.C. and Hacker, B.R. (2014). Age and significance of felsic dikes from the UHP western gneiss region. *Tectonics*. v.33, pp. 2342-2360.

Kylander-Clark, A.R.C., Hacker, B.R., Johnson, C.M., Beard, B.L., Mahlen, N.J., Lapen, T.J. (2007). Coupled Lu–Hf and Sm–Nd geochronology constrains prograde and exhumation histories of high- and ultrahigh-pressure eclogites from western Norway: *Chemical Geology*. v. 242, pp. 137-154.

Kylander-Clark, A.R.C., Hacker, B.R., Mattinson, J.M. (2008). Slow exhumation of UHP terranes: Titanite and rutile ages of the Western Gneiss Region, Norway. *Earth and Planetary Science Letters*. v. 272, pp. 531-540.

Krabbendam, M., Wain, A., and Andersen, T.B. (2000). Pre-Caledonian granulite and gabbro enclaves in the Western Gneiss Region, Norway: indications of incomplete transition at high pressure. *Geol. Mag*. V 137, pp. 235-255.

Lappin, M. A , Pidgeon, R.T. and van Breemen, 0 . (1979). Geochronology of basal gneisses and mangerite syenites of Stadtlandet, west Norway. *Norsk Geologisk Tidskrift*. v. 59, pp. 161-181.

Li, Z.X., Bogdanova, S.V., Collins, A.S, Davidson, A., Waele, B.D., Ernst, R.E., Fritzsimons., I.C.W., Fuck, R.A., Gladkochub, D.P., Jacobs, J., Karlstrom, K.E., Lu, S., Natapov, L.M., Pease, V., Pisarevsky, S.A., Thrane, K., Vernikovsky, V. (2008). Assembly, configuration, and break-up history of Rodinia: A synthesis. *Precambrian Research*. v. 160, pp. 179-210.

Rino, S., Kon, Y., Sato, W., Maruyama, S., Santosh, M., and Zhao, D. (2008). The Grenvillian and Pan-African orogens: world's largest orogenies through geologic time, and their implications on the origin of superplume. *Gondwana Research.* v. 14, pp. 51–72

Roberts, D. (2003). The Scandinavian Caledonides: event chronology, palaeogeographic settings and likely modern analogues. *Tectonophysics*. v. 365, pp. 283–299.

Roberts, N. M. and Slagstad, T. (2015). Continental growth and reworking on the edge of the Columbia and Rodinia supercontinents; 1.86–0.9 Ga accretionary orogeny in southwest Fennoscandia. *International Geology Review*, pp. 1–25.

Roffeis, C. and Corfu, F. (2014). Caledonian nappes of southern Norway and their correlation with Sveconorwegian basement domains. *Geological Society, London, Special Publications*. v. 390, pp. 193–221.

Skår, Ø. (2000). Field relations and geochemical evolution of the Gothian rocks in the Kvams0Y area, southern Western Gneiss Complex, Norway. *NGU-BULL. v.* 437, pp. 5.

Skår, Ø ., Furnes, H. & Claesson, S. 1994: Middle Proterozoic magmatism within the Western Gneiss Region, Sunnfjord, Norway. *Norsk Geologisk Tidsskrift.*. v. 74, pp. 114- 126.

Skår, Ø. and Pedersen, R.B. (2003). Relations between granitoid magmatism and migmatization: U–Pb geochronological evidence from the Western Gneiss Complex, Norway. *Journal of the Geological Society, London*. v. 160, pp. 935-946.

Skilbrei, J.R. and Kihle, O. (1998). Gravity modeling and petrophysical data from western Norway. *Geological survey of Norway*.

Slagstad, T., Henderson, I. H. C., Marker, M., Coint, N., Skår, Ø., Røhr, T. S., Høy, I., Sauer, S., Stormoen, M. A., Roberts, N. M. W., Kirkland, C. L., Sørensen, B. E. and Bybee. G. (2018). Magma-driven, high-grade metamorphism in the Sveconorwegian Province, 69 southwest Norway, during the termal stages of the Fennoscandian Shield evolution. *Geophere.* V. 14, pp. 2.

Slagstad, T., Pin, C., Roberts, D., Kirkland, C. L., Grenne, T., Dunning, G., Sauer, S. and Andersen, T. (2014). Tectonomagmatic evolution of the Early Ordovician suprasubduction-zone ophiolites of the Trondheim Region, Mid-Norwegian Caledonides. Geological Society, London, Special Publications. v. 390, pp.541-561.

Slagstad, T., Roberts, N. M., Marker, M., Røhr, T. S., and Schiellerup, H. (2013). A noncollisional, accretionary Sveconorwegian orogen. *Terra Nova*. v. 25, pp. 30–37.

Torsvik, T. H. and Cocks, L. R. M. (2005). Norway in space and time: a centennial cavalcade. *Norwegian Journal of Geology,* v 85, pp. 73–86.

Tucker, R.D., Krogh ,T.E.& Raheim, A. (1990). Proterozoic evolution and age province boundaries in the central part of the Western Gneiss Region, Norway: results of U-Pb dating of accessory minerals from Trondheimsfjord to Geiranger. In: Gower, C F., Rivers, T. & Ryan, B. (eds.) Mid-Proterozoic Geology of the Southern Margin of Proto Laurentia-Baltica. *Geological Association of Canada*. v. 38, pp. 149-173.

Vander Auwera, J., Bogaerts, M., Bolle.,O., Longhi.,J (2008). Genesis of intermediate igneous rocks at the end of the Sveconorwegian (Grenvillian) orogeny (S Norway) and their contribution to intracrustal differentiation. Contributions to Mineralogy and Petrology 156, .pp. 721-743.

Vander Auwera, J., Bogaerts, M., Liegeois, J-P., Demaiffe, D., Wilmart, E., Bolle, O., and Duchesne, J.C. (2003). Derivation of the 1.0–0.9 Ga ferro-potassic A-type granitoids of southern Norway by extreme differentiation from basic magmas. *Precambrian Research.*v.124, pp.107.148.

Wiest, J.D. (2016). *Mesoproterozoic to Early Devonian Evolution of the Lyderhorn Gneiss (Øygarden Complex, SW Norway)*. Master of Science Thesis, University of Bergen.

Wiest, J., Jacobs, J., Ksienzyk, A. and Fossen, H. (2018). Sveconorwegian vs. Caledonian orogenesis in the eastern Øygarden Complex, SW Norway – Geochronology, structural constraints and tectonic implications. *Precambrian Research*. v. 305, pp. 1-18.

Whitehouse, M. J. & Kamber, B. S. 2005. Assigning dates to thin gneissic veins in high-grade metamorphic terranes: a cautionary tale from Akilia, southwest Greenland. Journal of Petrology, v. 46, pp. 291-318.

Whitehouse, M. J., Kamber, B. S. & Moorbath, S. 1999. Age significance of U–Th–Pb zircon data from early Archaean rocks of west Greenland—a reassessment based on combined ion-microprobe and imaging studies. Chemical geology, v. 160, pp. 201-224.

Åhall, K.-I., and Connelly, J.N. (2008) Long-term convergence along SW Fennoscandia: 330 m.y. of Proterozoic crustal growth: *Precambrian Research.* v. 163, pp. 402–421.

Åhall, K.-I., Larson, S. Å. (2000). Growth-related 1.85–1.55 Ga magmatism in the Baltic Shield; a review addressing the tectonic characteristics of Svecofennian, TIB 1-related and Gothian events. *GFF* v. 122, pp. 193–206.

Schaltegger, U., Schmitt, A. and Horstwood, M. (2015). U–Th–Pb zircon geochronology by ID-TIMS, SIMS, and laser ablation ICP-MS: Recipes, interpretations, and opportunities. *Chemical Geology*. v.402, pp.89-110.

Schoene, B., Cottle, J. and Eddy, M. (2017). *U-Th-Pb Geo/Thermochronology*. [online] Usu.edu. Available at: https://www.usu.edu/geo/luminlab/UThPb.pdf [Accessed 2 May 2019].

Appendix 1: U-Pb geochronological results

			Concentration (ppm)							Total (uncorrected) ratio				Radiogenic (corrected) ratio[5]				Calculated age ± σ (Ma)			
Sample ID	Grain characteristics	Comment	U	Th	Pb	Th/U_{meas}[2]	$^{206}Pb/^{204}Pb$	f_{206} (%)[3]	Disc.(%)conv.[4]	$^{206}Pb/^{238}U$	± σ (%)	$^{207}Pb/^{206}Pb$	± σ (%)	$^{206}Pb/^{238}U$	± σ (%)	$^{207}Pb/^{206}Pb$	± σ (%)	$^{207}Pb/^{206}Pb$	$^{206}Pb/^{238}U$	207-corr age[6]	Conc (%)[7]
VAH48, Granitic augen gneiss, Honningsvåg																					
N6149-VAH48-9-2	CL-B, rim, UZ	Concordant	285.1	49.5	97.2	0.17	24795	0.08	4.8	3.3596	1.76	0.099840	0.43	3.3621	1.76	0.099285	0.45	1611±8	1679±26	>1200	96.0
N6149-VAH48-10-1	CL-B, rim, UZ	>5% Rev. discordance	603.2	120.0	209.2	0.20	872599	0.00	6.0	3.3191	1.55	0.099371	0.58	3.3191	1.55	0.099355	0.58	1612±11	1698±23	>1200	95.0
N6149-VAH48-4-1	CL-M, weakly Z	Pb-loss	106.0	59.5	35.4	0.56	29341	0.06	-7.3	3.7950	2.00	0.099834	0.83	3.7974	2.00	0.099365	0.85	1612±16	1507±27	>1200	107.0
N6149-VAH48-9-1	CL-M, Z?	>5% Rev. discordance	177.6	167.4	75.3	0.94	20153	0.09	8.8	3.2155	1.68	0.100464	0.45	3.2185	1.68	0.099781	0.47	1620±9	1744±26	>1200	92.9
N6149-VAH48-5-1	CL-M, Z	Concordant	265.8	160.5	97.1	0.60	85544	0.02	-0.1	3.4891	1.29	0.100213	0.42	3.4899	1.29	0.100052	0.42	1625±8	1624±19	>1200	100.1
N6149-VAH48-2-1	CL-M, Z?	Concordant	266.4	42.1	90.3	0.16	72204	0.03	3.1	3.3782	0.90	0.100347	0.81	3.3790	0.90	0.100157	0.81	1627±15	1671±13	>1200	97.4
N6149-VAH48-8-1	CL-M, Z	Concordant	135.2	37.0	47.4	0.27	186203	0.01	2.6	3.3680	1.52	0.100836	0.97	3.3683	1.52	0.100762	0.97	1638±18	1676±23	>1200	97.8
N6149-VAH48-6-1	CL-M, Z	Pb-loss	167.6	127.0	60.3	0.76	114390	0.02	-6.3	3.6879	3.02	0.100892	0.74	3.6885	3.02	0.100772	0.74	1638±14	1546±42	>1200	105.9
N6149-VAH48-12-1	CL-M, Z	Concordant	315.4	263.5	123.1	0.84	46764	0.04	-0.8	3.4578	1.24	0.101635	0.52	3.4592	1.24	0.101341	0.53	1649±10	1637±18	>1200	100.7
N6149-VAH48-7-1	CL-M, Z	Concordant	179.5	129.1	69.0	0.72	49452	0.04	0.3	3.4147	1.13	0.101735	0.47	3.4160	1.13	0.101457	0.48	1651±9	1655±17	>1200	99.7
N6149-VAH48-11-1	CL-M, weakly Z	Concordant	227.4	95.6	82.3	0.42	135594	0.01	1.2	3.3841	1.33	0.101614	0.45	3.3846	1.33	0.101513	0.46	1652±8	1669±20	>1200	99.0
N6149-VAH48-1-1	CL-M, Z	Concordant	164.3	125.2	62.6	0.76	93608	0.02	-1.3	3.4659	1.80	0.101736	0.49	3.4666	1.80	0.101590	0.50	1653±9	1634±26	>1200	101.2
N6149-VAH48-3-1	CL-M, Z	Concordant	251.1	153.4	93.6	0.61	128843	0.01	-0.9	3.4328	1.31	0.102133	0.39	3.4333	1.31	0.102027	0.40	1661±7	1648±19	>1200	100.8
N6149-VAH48-13-1	CL-M, Z	Concordant	245.2	147.8	92.7	0.60	64701	0.03	-0.1	3.3840	1.21	0.102716	0.68	3.3850	1.21	0.102504	0.68	1670±13	1669±18	>1200	100.1
MLM134, Quartz-monzonitic augen gneiss, Måløy																					
N6152-MLM134-15-1	CL-B, Z?	Pb-loss	132.8	93.8	37.5	0.71	45107	0.04	-7.7	4.6140	1.26	0.087277	1.30	4.6159	1.26	0.086967	1.32	1360±25	1264±15	>1200	107.6
N6152-MLM134-10-1	CL-M, Z	Pb-loss	241.5	107.0	69.6	0.44	75540	0.02	-5.6	4.2556	3.29	0.090527	1.82	4.2567	3.29	0.090342	1.83	1433±35	1360±41	>1200	105.3
N6152-MLM134-13-1	CL-M, weakly Z	Pb-loss	583.8	330.8	188.9	0.57	222848	0.01	-5.9	3.9241	1.10	0.095903	0.35	3.9245	1.10	0.095840	0.35	1545±7	1463±14	>1200	105.6
N6152-MLM134-6-1	CL-M, Z	Concordant	383.0	126.3	126.4	0.33	112209	0.02	0.9	3.6168	1.36	0.096829	0.48	3.6174	1.36	0.096706	0.49	1562±9	1573±19	>1200	99.2
N6152-MLM134-1-1	CL-M, Z	Concordant	199.8	71.2	64.5	0.36	27300	0.07	-3.1	3.7192	2.79	0.098043	1.50	3.7218	2.79	0.097537	1.52	1578±28	1534±38	>1200	102.8
N6152-MLM134-8-1	CL-D, UZ	Concordant, high U	1152.7	34.7	361.0	0.03	28680	0.07	0.3	3.5350	1.24	0.099202	0.52	3.5373	1.25	0.098722	0.54	1600±10	1605±18	>1200	99.7
N6152-MLM134-5-1	CL-D, Z	Concordant	463.4	72.6	150.4	0.16	62752	0.03	-1.2	3.5287	1.09	0.100279	0.64	3.5298	1.09	0.100060	0.65	1625±12	1608±16	>1200	101.1
N6152-MLM134-11-1	CL-D, Z?	Concordant	274.0	82.8	91.2	0.30	73450	0.03	-2.2	3.5663	1.47	0.100248	0.95	3.5673	1.47	0.100061	0.95	1625±18	1593±21	>1200	102.0
N6152-MLM134-2-1	CL-M, Z	Concordant	118.4	65.0	44.1	0.55	87942	0.02	3.0	3.3802	1.70	0.100368	0.96	3.3809	1.70	0.100212	0.96	1628±18	1670±25	>1200	97.5
N6152-MLM134-4-1	CL-D, Z	Concordant	571.5	419.5	212.6	0.73	335287	0.01	-1.6	3.5385	1.75	0.100261	0.28	3.5386	1.75	0.100220	0.28	1628±5	1604±25	>1200	101.5
N6152-MLM134-3-1	CL-B, Z?	>5% Rev. discordance	287.3	256.0	122.7	0.89	90006	0.02	8.8	3.1965	1.37	0.100435	0.95	3.1972	1.37	0.100282	0.95	1629±18	1754±21	>1200	92.9
N6152-MLM134-7-1	CL-M, Z	Concordant	213.2	105.9	76.5	0.50	147829	0.01	-0.3	3.4846	1.03	0.100429	0.45	3.4850	1.03	0.100336	0.45	1630±8	1626±15	>1200	100.3
N6152-MLM134-14-1	CL-M, Z	Concordant	331.3	122.7	120.6	0.37	95088	0.02	4.1	3.3199	1.18	0.100863	0.46	3.3206	1.18	0.100719	0.46	1637±9	1697±18	>1200	96.5
N6152-MLM134-12-1	CL-B, weakly Z	Concordant	139.6	102.9	54.9	0.74	97032	0.02	1.2	3.3541	1.26	0.102354	0.91	3.3547	1.26	0.102213	0.92	1665±17	1682±19	>1200	99.0
N6152-MLM134-9-1	CL-M, Z	Concordant	520.0	281.5	201.7	0.54	246657	0.01	2.2	3.2574	1.07	0.103825	0.46	3.2577	1.07	0.103769	0.46	1693±9	1726±16	>1200	98.1
VAH78, Granitic augen gneiss, Hornindal																					
N6148-VAH78-8-2	CL-D, rim, UZ	Concordant	665.7	45.2	154.3	0.07	90178	0.02	3.2	4.7471	1.15	0.080152	0.32	4.7481	1.15	0.079995	0.33	1197±6	1232±13	>1200	97.1
N6148-VAH78-10-1	CL-M, Z	Pb-loss	296.0	145.7	76.7	0.49	11305	0.17	-7.3	4.7692	1.55	0.086102	0.87	4.7771	1.55	0.084860	1.01	1312±20	1225±17	>1200	107.1
N6148-VAH78-4-2	CL-B, rim, UZ	Pb-loss	185.5	23.6	44.8	0.13	23815	0.08	-9.6	4.6421	2.94	0.088340	1.90	4.6457	2.94	0.087752	1.93	1377±37	1257±34	>1200	109.6
N6148-VAH78-3-2	CL-B, rim, UZ	Pb-loss	265.5	25.7	68.2	0.10	199042	0.01	-12.9	4.3718	3.81	0.093808	2.90	4.3723	3.81	0.093739	2.90	1503±55	1328±46	>1200	113.2
N6148-VAH78-4-1	CL-D, Z	Concordant	346.1	112.8	112.1	0.33	59644	0.03	-0.7	3.6671	1.34	0.097022	0.73	3.6682	1.34	0.096790	0.74	1563±14	1554±19	>1200	100.6
N6148-VAH78-11-2	CL-B, rim, UZ	>5% Rev. Discordance, high U	1053.7	37.5	337.8	0.04	131678	0.01	5.4	3.4512	1.37	0.097004	0.32	3.4517	1.37	0.096899	0.32	1565±6	1640±20	>1200	95.4
N6148-VAH78-2-1	CL-D, Z	Concordant	406.3	111.6	131.9	0.27	57548	0.03	-2.4	3.6292	1.90	0.099107	1.00	3.6304	1.90	0.098868	1.00	1603±19	1568±27	>1200	102.2
N6148-VAH78-14-1	CL-D, Z	Concordant	453.9	156.9	149.4	0.35	114969	0.02	-3.0	3.6238	1.15	0.099583	0.34	3.6244	1.15	0.099463	0.34	1614±6	1571±16	>1200	102.8
N6148-VAH78-15-1	CL-D, Z	Concordant	422.7	485.9	174.6	1.15	55809	0.03	0.7	3.4843	0.98	0.099805	0.43	3.4855	0.98	0.099558	0.43	1616±8	1626±14	>1200	99.4
N6148-VAH78-6-1	CL-D, Z	>10% Rev. discordance.	805.3	649.4	342.8	0.81	186711	0.01	12.7	3.1113	1.38	0.099735	0.35	3.1116	1.38	0.099661	0.35	1618±7	1796±22	>1200	90.1
N6148-VAH78-5-1	CL-M, Z	Concordant	155.6	111.3	59.8	0.72	59195	0.03	1.8	3.4008	1.92	0.100862	0.69	3.4018	1.92	0.100629	0.70	1636±13	1661±28	>1200	98.5
N6148-VAH78-14-2	Cl-B, rim, UZ	Concordant	626.4	240.0	228.4	0.38	119462	0.02	3.2	3.3326	0.87	0.101221	0.41	3.3332	0.87	0.101106	0.41	1645±8	1691±13	>1200	97.2
N6148-VAH78-11-1	CL-D, Z	Concordant, high U	1380.7	3515.9	760.9	2.55	372566	0.01	2.7	3.3423	0.96	0.101314	0.25	3.3425	0.96	0.101278	0.25	1648±5	1687±14	>1200	97.7
N6148-VAH78-3-1	CL-D, Z	Concordant	567.4	84.5	187.5	0.15	132761	0.01	-0.8	3.4612	2.43	0.101388	0.43	3.4617	2.43	0.101284	0.43	1648±8	1636±35	>1200	100.7
N6148-VAH78-9-1	CL-M, Z	Concordant	219.8	133.9	82.8	0.61	80169	0.02	1.0	3.3954	1.36	0.101536	0.67	3.3961	1.36	0.101365	0.68	1649±13	1664±20	>1200	99.1
N6148-VAH78-12-1	CL-M, Z	Concordant	383.9	158.6	139.2	0.41	99187	0.02	1.3	3.3782	1.75	0.101695	0.82	3.3788	1.75	0.101556	0.82	1653±15	1671±26	>1200	98.9
N6148-VAH78-1-1	CL-D, Z	Concordant	280.8	84.4	96.5	0.30	64838	0.03	-1.2	3.4453	2.71	0.102169	0.78	3.4463	2.71	0.101957	0.79	1660±15	1642±39	>1200	101.1
N6148-VAH78-8-1	CL-D, Partly Z	Concordant	430.9	180.4	149.8	0.42	44323	0.04	-3.7	3.5165	1.94	0.102694	0.51	3.5179	1.94	0.102384	0.52	1668±10	1613±28	>1200	103.4
N6148-VAH78-13-1	CL-D, Core, Z	Concordant	546.5	347.7	217.4	0.64	294195	0.01	3.1	3.2407	1.08	0.103512	0.33	3.2409	1.08	0.103465	0.33	1687±6	1734±16	>1200	97.3
VAH04, Monzonitic augen gneiss, Oldedalen																					
N6151-VAH04-9-1	CL-M, Z	Pb-loss	194.4	168.2	39.7	0.87	8172	0.23	-4.8	6.5959	1.21	0.072518	0.72	6.6110	1.22	0.070768	0.98	951±20	908±10	906±11	104.7
N6151-VAH04-1-1	CL-B, Z	>5% Rev. discordance.	62.4	64.1	13.5	1.03	5825	0.32	6.0	6.3529	1.32	0.071170	1.27	6.3734	1.32	0.068708	1.58	890±32	940±12	942±12	94.7
N6151-VAH04-10-1	CL-M, Z	>5% Rev. discordance.	63.9	107.1	16.2	1.68	8906	0.21	6.2	6.2538	1.97	0.070732	1.31	6.2670	1.97	0.069122	1.53	902±32	954±18	957±18	94.6
N6151-VAH04-6-1	CL-M, Z	>10% Rev. discordance.	194.4	236.8	44.2	1.22	3372	0.55	14.5	6.2276	1.24	0.071397	0.75	6.2623	1.24	0.067134	1.09	842±23	955±11	960±12	88.2
N6151-VAH04-7-1	CL-B, Z	Concordant	76.9	131.9	19.5	1.71	25620	0.07	0.8	6.2476	1.08	0.071291	1.96	6.2522	1.08	0.070733	2.01	950±41	956±10	957±10	99.3
N6151-VAH04-12-1	CL-M, Z	Concordant	91.4	111.1	21.2	1.21	25769	0.07	3.4	6.2381	1.13	0.070571	1.05	6.2426	1.13	0.070016	1.11	929±23	958±10	959±11	97.0
N6151-VAH04-2-1	CL-M, Z?	Concordant	109.5	165.3	27.2	1.51	25148	0.07	4.9	6.1878	2.83	0.070392	1.48	6.1924	2.83	0.069823	1.52	923±31	965±25	967±26	95.7
N6151-VAH04-4-1	CL-M, Z	>5% Rev. discordance.	89.6	96.7	20.1	1.08	29445	0.06	5.5	6.1855	1.17	0.070145	1.04	6.1894	1.17	0.069659	1.10	918±23	965±11	967±11	95.1
N6151-VAH04-3-1	CL-M, Z	Concordant	104.4	118.7	23.9	1.14	60439	0.03	-1.7	6.1817	1.41	0.072092	0.96	6.1836	1.41	0.071855	0.98	982±20	966±13	966±13	101.6
N6151-VAH04-5-1	CL-M, Z	Concordant	129.1	233.7	34.0	1.81	13973	0.13	2.4	6.1555	1.06	0.071705	0.87	6.1638	1.06	0.070681	0.96	948±20	969±10	970±10	97.8
N6151-VAH04-11-1	CL-M, weakly Z	Concordant	178.2	147.4	38.4	0.83	83465	0.02	2.7	6.1484	1.21	0.070835	0.80	6.1497	1.21	0.070663	0.81	948±17	971±11	972±11	97.6
N6151-VAH04-8-1	CL-M, Z	>5% Rev. discordance.	89.2	158.8	23.4	1.78	16249	0.12	5.2	6.1321	1.12	0.070880	1.05	6.1392	1.12	0.069999	1.15	928±24	973±10	975±11	95.4

VAH11, Monzonitic augen gneiss, Loen																					
N6147-VAH11-4-1	CL-M, partly Z	Pb-loss	87.3	186.8	21.2	2.14	23328	0.08	-5.0	7.0580	1.41	0.069503	1.24	7.0637	1.41	0.068888	1.30	895±27	854±11	852±12	95.3
N6147-VAH11-4-2	CL-B, rim, UZ	Pb-loss	196.9	190.7	40.0	0.97	18379	0.10	-4.0	6.7134	1.04	0.070788	1.05	6.7203	1.04	0.070009	1.09	928±22	894±9	893±9	96.3
N6147-VAH11-9-1	CL-B, partly Z	>5% Rev. discordance.	47.2	67.1	10.8	1.42	7909	0.24	6.3	6.4969	4.03	0.069850	1.50	6.5123	4.04	0.068035	1.82	870±38	921±35	923±36	105.9
N6147-VAH11-12-1	CL-B, UZ?	Concordant	74.7	133.5	18.9	1.79	16586	0.11	1.4	6.4639	3.78	0.070376	1.05	6.4712	3.79	0.069512	1.15	914±24	926±33	927±34	101.4
N6147-VAH11-11-1	CL-M, Z	Concordant	119.5	178.4	28.7	1.49	37492	0.05	3.1	6.3889	1.71	0.069787	0.90	6.3920	1.71	0.069404	0.94	911±19	937±15	938±16	102.9
N6147-VAH11-8-1	CL-M, Z	Concordant	119.5	93.3	24.8	0.78	2374	0.79	1.6	6.2183	0.95	0.076448	1.26	6.2677	0.95	0.070419	1.80	941±37	954±8	955±9	101.5
N6147-VAH11-6-1	CL-M, Z	Concordant	106.3	157.2	25.8	1.48	19555	0.10	1.5	6.2381	1.08	0.071280	0.96	6.2440	1.08	0.070548	1.03	944±21	958±10	958±10	101.4
N6147-VAH11-10-1	CL-M, Z	Concordant	128.7	139.4	29.0	1.08	12847	0.15	-0.4	6.2064	1.03	0.072403	0.89	6.2155	1.03	0.071290	0.97	966±20	962±9	962±10	99.6
N6147-VAH11-13-1	CL-M, Z	Concordant	162.1	165.6	36.2	1.02	>1e6	0.00	-1.1	6.1971	1.30	0.071595	1.14	6.1971	1.30	0.071595	1.14	974±23	964±12	964±12	99.0
N6147-VAH11-15-1	CL-M, Z	Concordant	78.5	68.8	16.9	0.88	30289	0.06	-0.7	6.1882	1.30	0.071952	1.68	6.1920	1.30	0.071480	1.75	971±36	965±12	965±12	99.4
N6147-VAH11-5-1	CL-M, Z	Concordant	105.5	107.0	23.6	1.01	24685	0.08	2.7	6.1621	1.10	0.071159	0.96	6.1667	1.10	0.070580	1.02	945±21	969±10	970±10	102.5
N6147-VAH11-1-1	CL-M, Z	Concordant	70.4	105.3	17.4	1.50	19317	0.10	1.7	6.1290	1.18	0.071768	1.16	6.1349	1.18	0.071027	1.36	958±28	973±11	974±11	101.6
N6147-VAH11-3-1	CL-M, Z	>5% Rev. discordance	137.4	160.7	31.9	1.17	32777	0.06	5.5	6.0864	0.88	0.070569	0.99	6.0899	0.88	0.070132	1.03	932±21	980±8	982±8	105.1
N6147-VAH11-7-1	CL-M, Z	>5% Rev. discordance	111.7	125.5	25.9	1.12	23246	0.08	6.4	6.0451	1.39	0.070697	0.93	6.0499	1.39	0.070081	1.00	931±20	986±13	989±13	106.0
N6147-VAH11-2-1	CL-M, Z	>10% Rev. discordance	108.2	125.2	25.2	1.16	16632	0.11	10.6	6.0084	1.16	0.070000	0.93	6.0151	1.17	0.069138	1.02	903±21	991±11	995±11	109.8
N6147-VAH11-14-1	CL-D, UZ	>5% Rev. Discordance	170.5	262.7	43.3	1.54	40605	0.05	9.6	5.8985	1.81	0.070304	0.71	5.9012	1.81	0.069951	0.74	927±15	1009±17	1013±18	108.9
VAH23, Granitic, banded augen gneiss, Florø																					
N6153-VAH23-10-1	CL-M, Z	Pb-loss	343.2	324.2	61.3	0.94	4394	0.43	-13.1	7.4141	3.72	0.073209	1.09	7.4458	3.74	0.069950	1.25	927±26	812±29	809±29	87.6
N6153-VAH23-16-1	CL-M, Z?	Extreme high rev. discordance, extreme age error	138.3	128.9	28.5	0.93	732	2.56	27.9	6.4822	3.38	0.082980	6.79	6.6522	3.46	0.063241	21.06	716±459	903±29	910±31	126.0
N6153-VAH23-11-1	CL-B, Z	Concordant	43.5	62.0	9.9	1.43	5772	0.32	1.8	6.6243	3.55	0.071156	1.53	6.6458	3.56	0.068671	1.90	889±39	904±30	904±31	101.7
N6153-VAH23-2-1	CL-B, Z	>5% Rev. discordance	117.1	155.2	25.7	1.33	12520	0.15	6.6	6.6200	0.94	0.068631	1.07	6.6299	0.94	0.067484	1.21	853±25	906±8	908±8	106.2
N6153-VAH23-14-1	CL-M, Z	Concordant, ekstreme age error.	98.4	107.0	21.4	1.09	2723	0.69	0.2	6.4003	1.45	0.075247	1.53	6.4445	1.46	0.069989	4.28	928.±88	930±13	930±13	100.2
N6153-VAH23-1-1	CL-M, Z	>5% Rev. discordance	68.6	82.3	15.3	1.20	4815	0.39	11.6	6.3715	1.43	0.070215	1.43	6.3963	1.44	0.067230	1.80	845±37	936±13	940±13	110.8
N6153-VAH23-3-1	CL-B, Z?	Pb-loss	34.4	58.4	8.6	1.70	7476	0.25	-4.7	6.3737	1.82	0.073700	1.75	6.3897	1.83	0.071789	2.15	980±44	937±16	936±17	95.6
N6153-VAH23-9-1	CL-B, Z	Concordant	48.7	77.9	12.0	1.60	19505	0.10	2.3	6.3077	1.39	0.070726	1.47	6.3137	1.39	0.069992	1.64	928±34	948±12	949±13	102.1
N6153-VAH23-15-1	CL-M, Z	Concordant	99.1	104.6	21.8	1.06	12416	0.15	2.4	6.2768	1.41	0.071235	1.03	6.2863	1.41	0.070081	1.22	931±25	952±13	953±13	102.2
N6153-VAH23-6-1	CL-M, Z	Concordant	132.6	83.9	26.8	0.63	49045	0.04	3.0	6.2696	1.22	0.070260	0.90	6.2720	1.22	0.069968	0.93	927±19	954±11	955±11	102.8
N6153-VAH23-8-1	CL-M, Z	Concordant	90.3	88.2	19.9	0.98	9632	0.19	4.8	6.2520	1.58	0.070995	1.09	6.2642	1.58	0.069508	1.34	914±28	955±14	956±15	104.5
N6153-VAH23-4-1	CL-D, UZ	>5% Rev. discordance	394.2	387.4	86.6	0.98	27334	0.07	5.3	6.2246	1.34	0.070053	0.53	6.2289	1.34	0.069529	0.56	914±11	960±12	962±12	105.0
N6153-VAH23-5-1	CL-B, UZ	>10% Rev. discordance, extreme age error.	15.0	20.7	3.6	1.37	4916	0.38	10.1	6.2010	1.90	0.071243	4.01	6.2247	1.91	0.068324	4.50	878±93	960±17	964±18	109.3
N6153-VAH23-13-1	CL-B, Z?	>10% Rev. discordance, extreme age error.	47.1	73.5	11.7	1.56	703	2.66	13.8	6.0326	1.75	0.087965	4.08	6.1974	1.79	0.067543	7.91	855±165	964±16	969±17	112.8
N6153-VAH23-8-2	CL-B, weakly Z	>5% Rev. discrodance	106.6	126.1	24.7	1.18	23044	0.08	5.4	6.1495	1.30	0.070474	1.00	6.1545	1.30	0.069852	1.06	924±22	971±12	973±12	105.0
N6153-VAH23-12-1	CL-B, Z	Extreme high Rev. Discordance, extreme age error	69.2	73.3	15.3	1.06	796	2.35	70.4	5.9791	3.34	0.077850	5.60	6.1229	3.41	0.059626	14.61	590±321	975±31	990±32	165.3
N6153-VAH23-7-1	CL-B, Z?	>10% Rev.discordance	70.2	123.8	18.6	1.76	15346	0.12	11.4	6.0340	1.39	0.069733	1.24	6.0414	1.39	0.068798	1.35	893±28	987±13	991±13	110.6
VAH31, Muscovite-granitic gneiss, Hyen																					
N6154-VAH31-10-1	CL-D, Z	Extreme high Rev. discordance.	878.3	500.7	99.8	0.57	215	8.68	32.8	9.8590	1.90	0.123270	3.98	10.7962	2.05	0.055552	16.33	435±370	571±11	574±13	131.4
N6154-VAH31-3-1	CL-D, Z	Extreme Pb-loss	887.8	582.1	114.1	0.66	167	11.17	-68.0	9.2789	7.14	0.185162	24.37	10.4453	8.03	0.103396	57.98	1686±1316	589±45	557±56	35.0
N6154-VAH31-5-1	CL-D, Z	Pb-loss	720.7	1620.0	131.0	2.25	462	4.05	-12.0	9.4480	1.35	0.094178	2.34	9.8470	1.38	0.062870	5.31	704±113	624±8	622±9	88.6
N6154-VAH31-1-1	CL-D, Z	Pb-loss	815.5	460.5	104.1	0.56	564	3.31	-22.2	9.4765	1.30	0.091149	2.74	9.8014	1.33	0.065625	5.81	794±122	626±8	622±9	78.8
N6154-VAH31-7-1	CL-D, Z	Concealed Pb-loss	982.1	436.7	124.6	0.44	511	3.66	1.4	9.0331	1.80	0.089492	2.15	9.3761	1.86	0.061158	3.82	645±82	653±12	653±12	101.3
N6154-VAH31-2-1	CL-D, Z	Pb-loss	808.3	700.4	119.7	0.87	952	1.96	-11.8	8.9606	1.19	0.079515	3.94	9.1402	1.20	0.064362	6.59	754±140	669±8	667±8	88.8
N6154-VAH31-12-1	CL-D, Z?	Pb-loss	749.7	1940.4	173.3	2.59	520	3.60	-21.2	7.7279	1.67	0.098185	2.08	8.0164	1.72	0.070656	3.49	947±72	758±12	752±13	80.0
N6154-VAH31-6-1	CL-D, Z	Concealed Pb-loss	301.6	329.4	54.4	1.09	779	2.40	-4.7	7.6951	1.18	0.084464	1.04	7.8845	1.20	0.065976	2.15	806±45	770±9	769±9	95.6
N6154-VAH31-9-1	CL-D, Z	Pb-loss	612.6	749.5	115.3	1.22	817	2.29	-8.5	7.6286	1.21	0.084813	3.32	7.8073	1.23	0.067223	6.77	845±141	777±9	775±10	92.0
N6154-VAH31-4-1	CL-M, Z	Pb-loss	244.8	198.8	43.2	0.81	1076	1.74	-12.7	7.4848	1.29	0.082486	1.93	7.6172	1.31	0.069159	2.63	903±54	795±10	792±10	88.0
N6154-VAH31-11-1	CL-D, Z	Concordant	483.7	397.5	91.1	0.82	3045	0.61	-4.0	7.0110	2.12	0.073337	1.28	7.0543	2.13	0.068627	1.87	888±39	855±17	853±18	96.3
N6154-VAH31-8-1	CL-D, Z	Concordant	407.6	856.4	108.8	2.10	3208	0.58	-0.6	6.4023	1.59	0.074716	0.59	6.4398	1.60	0.070254	0.80	936±16	931±14	930±14	99.4
VAH44, Granitic augen gneiss, Maurstad																					
~~N6150-VAH44-6-2~~	~~CL-B, rim, UZ~~	~~Analytical problem~~	~~277.66~~	~~0.69~~	~~[18]~~	~~0.00~~	~~1549.54~~	~~1.21~~	~~816.82~~	~~15.63~~	~~1.32~~	~~0.05~~	~~1.11~~	~~15.82~~	~~1.33~~	~~0.04~~	~~11.11~~	~~(-)57±273~~	~~395±5~~	~~400±5~~	~~-692.00~~
N6150-VAH44-16-1	CL-B, rim, UZ	Concordant	2535.8	25.1	175.1	0.01	39467	0.05	0.7	15.2992	0.97	0.055199	0.44	15.3064	0.97	0.054829	0.46	405±10	408±4	408±4	100.7
N6150-VAH44-11-1	CL-D, core, UZ	>5% Rev. discordance	872.8	4.2	60.7	0.00	69943	0.03	8.8	15.1770	1.41	0.054402	0.70	15.1811	1.41	0.054193	0.72	379±16	411±6	412±6	108.5
N6150-VAH44-9-2	CL-D, UZ	Conocrdant	4561.3	47.9	319.6	0.01	279443	0.01	0.3	15.1011	3.87	0.055053	0.26	15.1022	3.87	0.055001	0.26	412±6	413±15	413±16	100.3
N6150-VAH44-14-2	CL-B, rim, UZ	Concordant	1266.4	8.6	88.8	0.01	120979	0.02	-3.4	15.0738	1.09	0.055512	0.59	15.0761	1.09	0.055392	0.60	428±13	414±4	414±4	96.7
N6150-VAH44-13-2	CL-D, UZ	Concordant	1927.8	16.0	135.4	0.01	183747	0.01	-3.9	15.0661	1.01	0.055536	0.40	15.0676	1.01	0.055457	0.40	431±9	414±4	414±4	96.2
N6150-VAH44-5-1	CL-D, UZ	>5% Rev. discordance	2116.8	23.3	149.7	0.01	87511	0.02	6.9	14.9555	1.03	0.054650	0.40	14.9587	1.03	0.054483	0.41	391±9	417±4	417±4	106.7
N6150-VAH44-15-2	CL-D, UZ	Concordant	2414.8	23.3	171.1	0.01	367822	0.01	-3.1	14.9331	1.26	0.055495	0.44	14.9339	1.26	0.055455	0.44	431±10	418±5	418±5	97.0
N6150-VAH44-14-1	CL-D, UZ	Pb-loss	1422.6	442.5	166.4	0.31	76968	0.02	-14.1	10.1640	4.26	0.062908	1.37	10.1665	4.26	0.062720	1.37	699±29	605±25	603±25	86.6
N6150-VAH44-6-1	CL-M, core, Z?	Pb-loss	580.1	289.1	79.5	0.50	3067	0.61	-9.4	9.0646	1.26	0.068552	2.05	9.1203	1.26	0.063845	3.18	737±67	671±8	669±8	91.1
N6150-VAH44-9-1	CL-M, core, Z	Pb-loss	442.1	234.2	63.7	0.53	10422	0.18	-6.3	8.6560	1.47	0.065581	0.96	8.6716	1.48	0.064197	1.03	748±22	704±10	702±10	94.0
N6150-VAH44-8-1	CL-M, core, Z	Pb-loss	439.4	294.5	75.2	0.67	36325	0.05	-7.1	7.5236	1.05	0.068163	0.71	7.5275	1.05	0.067768	0.73	861±15	804±8	802±8	93.3
N6150-VAH44-3-1	CL-M, core, Z	Pb-loss	612.3	385.7	109.8	0.63	17954	0.10	-5.1	7.0770	1.16	0.069627	0.70	7.0844	1.16	0.068828	0.75	894±15	851±9	850±10	95.3
N6150-VAH44-15-1	CL-B, core, UZ	Concordant	456.7	350.5	86.4	0.77	21460	0.09	3.6	6.9842	2.61	0.067542	0.94	6.9903	2.61	0.066872	0.98	834±20	862±21	863±22	13.4
N6150-VAH44-10-1	CL-M, core, Z	Concordant	167.4	115.4	31.0	0.69	8941	0.21	-2.6	6.9620	1.65	0.070158	0.83	6.9766	1.65	0.068553	0.97	885±20	863±13	863±14	97.5
N6150-VAH44-4-1	CL-M/D, core, Z	Concordant	558.5	369.7	103.1	0.66	66652	0.03	-3.8	6.9502	2.45	0.069203	0.44	6.9522	2.45	0.068988	0.46	898±9	866±20	865±21	96.4
N6150-VAH44-2-1	CL-M, core, Z	Concordant	687.2	395.3	125.6	0.58	21890	0.09	-3.7	6.8382	1.39	0.070053	0.71	6.8440	1.39	0.069399	0.73	911±15	879±11	878±12	96.5
N6150-VAH44-1-1	CL-B, core, UZ	Concordant	42.8	45.1	9.2	1.05	9389	0.20	-1.3	6.5088	1.06	0.071602	1.57	6.5218	1.06	0.070077	1.76	931±36	920±9	919±10	98.8
N6150-VAH44-13-1	CL-B, core, Z?	>5% Rev. discordance	84.5	60.3	17.7	0.71	17674	0.11	5.9	6.1152	1.38	0.070682	2.50	6.1217	1.38	0.069872	2.57	925±53	975±13	978±13	105.5
1) CL=Cathodoluminiescence, B=Bright, M=Moderate, D=Dark, Z=Zoned (oscilliatory zoned), UZ=Unzoned																					
2) Based on measured Th and U signals																					
3) f$_{206}$ is the percentage of common Pb estimated from 204Pb counts; in parentheses where these are insignificant;																					
4) % discordance. Positive numers represents reverse discordance																					
5) Ratios after subtraction of common Pb (if detected)																					
6) Age based on projecting a line in inverse concordia diagram from assumed common Pb through the total (uncorrected) ratios into concordia (Ludwig, 2012)																					
7) Concordance in %. Measured from calculating (^{206}Pb/^{238}U ages / ^{207}Pb/^{206}Pb ages)*100.																					

Appendix 2: List of outcrops

Nr.	UTM 32		Lithology	Comments	Foliation		Lineation		Fold Axis	
	Easting	Northing			Dip dir.	Dip	Trend	Plunge	Trend	Plunge
1	297718.4	6875869.6	Granitic to granodioritic gneiss		84	26	82	18		
2	297712.8	6875814	Granitic to granodioritic gneiss	Top to NW movment			125	28		
3	297718.3	6875806.1	Granitic to granodioritic gneiss							
5	297712.1	6875733.8	Granitic to granodioritic gneiss	With amp. lenses						
6	297725.9	6875660.2	Granitic to granodioritic gneiss	With amp. lenses						
7	297727.8	6875548.2	Granitic to granodioritic gneiss	With amp. lenses						
8	297719.4	6875458.6	Granitic to granodioritic gneiss	With amp. lenses					55	2
9	297762.5	6875382.2	Granitic to granodioritic gneiss						70	2
10	297734.1	6875338.4	Amphibiolite							
11	297653.6	6875248.1	Granitic to granodioritic gneiss		190	28	158	19		
12	297620.6	6875215.5	Garnet- bearing monzonitic gneiss		193	28	130	17		
13	297595.8	6875184.3	Garnet- bearing monzonitic gneiss		190	30				
14	297578.3	6875163	Garnet- bearing monzonitic gneiss							
15	297529.7	6875077.1	Garnet- bearing monzonitic gneiss		216	28				
16	297511.1	6874942.2	Garnet- bearing monzonitic gneiss	With dioritic lense						
17	297485.4	6874897.7	Garnet- bearing monzonitic gneiss	With dioritic lense						
19	297232.3	6874571	Dioritic lense		114	25	156	15		
20.1	297140.8	6874427.8	Garnet- bearing monzonitic gneiss							
20.2	297135.8	6874422	Dioritic lense							
21.1	296962.6	6874153.7	Metagabbro							
21.2	296940	6874100	Metagabbro		205	20				
21.3	296933	6874075	Metagabbro		232	45				
21.4	296931	6874065	Metagabbro		226	29				
22	296922.5	6874049.8	Metagabbro						156	9
23	296898.5	6873904.4	Granitic to granodioritic gneiss							
24	296884	6873871	Granitic to granodioritic gneiss		98	25				
25.1	296862	6873845	Granitic to granodioritic gneiss		45	38				
25.2	296848	6873831	Granitic to granodioritic gneiss		80	20				
26	296825	6873811	Shear zone	Top to W movment	88	25	78	26		
26.2	296804	6873790	Granitic to granodioritic gneiss		90	38				
27	296768	6873760	Shear zone	Top to NW movment	48	28	122	20		
28	295573	6873259	Granitic to granodioritic gneiss		45	51	114	21		
29	295619	6873391	Granitic to granodioritic gneiss		25	60				
30	295643	6873429	Granitic to granodioritic gneiss		26	39				
31	295710	6873467	Granitic to granodioritic gneiss		35	37				
32	295763	6873566	Granitic to granodioritic gneiss		336	51				
33	295764	6873588	Granitic to granodioritic gneiss							
34	295741	6873662	Amphibiolite/eclogite		11	60				
35	295707	6873718	Granitic to granodioritic gneiss	Top to W movment	41	8	117	12		
36	295707	6873738	Granitic to granodioritic gneiss		304	17				
37	295697	687375	Granitic to granodioritic gneiss		67	25				
38	295590	6873812	Granitic to granodioritic gneiss							
39	295626	6873819	Granitic to granodioritic gneiss		43	26				
40	295555	6873858	Granitic to granodioritic gneiss							
41	295566	6873847	Dioritic lense							
42	295558	6873880	Dioritic lense							
43	295555.9	6874012	Dioritic lense							
44	295563	6874110	Garnet-bearing monzonitic gneiss							
45	295572	6874202	Garnet-bearing monzonitic gneiss		246	65				
46	295591	6874375	Dioritic lense							
47	295598	6874419	Garnet-bearing monzonitic gneiss							
48	295607	6874446	Garnet-bearing monzonitic gneiss	With feldspar lense	170	25				
49	295609	6874503	Dioritic lense							
50	295614	6874528	Garnet-bearing monzonitic gneiss		224	34				
51	295601	6874528	Garnet-bearing monzonitic gneiss	With feldspar lense						
52	295592	6874632	Garnet-bearing monzonitic gneiss		130	15				
53	295612	6874648	Garnet-bearing monzonitic gneiss		164	24	190	14		
54.1	295632	6874623	Garnet-bearing monzonitic gneiss							
54.2	295655	6874651	Garnet-bearing monzonitic gneiss							
55	295601	6874662	Garnet-bearing monzonitic gneiss		146	26	180	25		
56	295511	6874871	Garnet-bearing monzonitic gneiss							
57.1	295516	6874884	Garnet-bearing monzonitic gneiss						264	80
57.2	295606	6874434	Garnet-bearing monzonitic gneiss		186	27	190	30		

58	295503	6874855	Eclogite							
59	295519	6874890	Eclogite							
60	295529	6874909	Eclogite							
61	295539	6874914	Eclogite							
62	295470	6875042	Garnet-bearing monzonitic gneiss							
63	295488	6875103	Garnet-bearing monzonitic gneiss		137	30				
64	295503	6875108	Eclogite							
65	295456	6875108	Eclogite							
66	295439	6875215	Eclogite							
67	295424	6875187	Amphibole?eclogite?							
68.1	295229	6875159	Eclogite							
68.2	295234	6875159	Eclogite							
68.3	295245	6875151	Eclogite							
68.4	295219	6875157	Eclogite							
68.5	295223	6875150	Eclogite							
69	295201	6875151	Eclogite	Partly retrogressed						
70	295189	6875134	Garnet-bearing monzonitic gneiss							
71	295177	6875071	Garnet-bearing monzonitic gneiss							
72	295178	6875034	Garnet-bearing monzonitic gneiss							
73	295152	6874957	Garnet-bearing monzonitic gneiss		115	47				
74	295130	6874839	Garnet-bearing monzonitic gneiss		198	30				
75	295095	6874799	Garnet-bearing monzonitic gneiss							
76	295040	6874659	Garnet-bearing monzonitic gneiss							
77	295069	6874529	Garnet-bearing monzonitic gneiss							
78	295095	6874506	Garnet-bearing monzonitic gneiss		187	45				
79	295288	6874268	Garnet-bearing monzonitic gneiss							
80	295364	6874152	Garnet-bearing monzonitic gneiss							
81	295364	6874061	Garnet-bearing monzonitic gneiss		70	69				
82	295552	6873868	Garnet-bearing monzonitic gneiss		47	62				
83	295329	6873115	Granitic to granodioritic gneiss	Top to W movment	42	25	82	15		
84	295296	6873185	Granitic to granodioritic gneiss							
85	295189	6873222	Granitic to granodioritic gneiss							
86	294993	6873296	Granitic to granodioritic gneiss							
87	294779	6873412	Granitic to granodioritic gneiss							
88	294777	6873439	Granitic to granodioritic gneiss		75	36				
89	294744	6873439	Granitic to granodioritic gneiss							
90	294693	6873440	Granitic to granodioritic gneiss							
91	294673	6873441	Granitic to granodioritic gneiss							
92	294658	6873441	Granitic to granodioritic gneiss							
93	294542	6873476	Granitic to granodioritic gneiss							
94	294514	6873535	Amphibole?eclogite?							
96	294475	6873639	Granitic to granodioritic gneiss		60	50				
97	294450	6873745	Granitic to granodioritic gneiss							
98	294416	6873890	Granitic to granodioritic gneiss							
99	294371	6874029	Granitic to granodioritic gneiss							
100	294335	6874075	Amphibole?eclogite?		78	42				
101	294287	6874094	Amphibole?eclogite?							
102	294281	6874095	Granitic to granodioritic gneiss							
103	294268	6874105	Granitic to granodioritic gneiss							
104	294229	6874158	Granitic to granodioritic gneiss							
105	294249	6874186	Granitic to granodioritic gneiss		70	45				
107	294278	6874212	Granitic to granodioritic gneiss		50	50				
108	294319	6874258	Granitic to granodioritic gneiss							
109	294364	6874284	Granitic to granodioritic gneiss							
110	294381	6874288	Granitic to granodioritic gneiss							
111	294410	6874289	Granitic to granodioritic gneiss							
112	294485	6874345	Granitic to granodioritic gneiss							
113	294512	6874452	Granitic to granodioritic gneiss							
114	294509	6874507	Granitic to granodioritic gneiss							
115	294516	6874532	Granitic to granodioritic gneiss		66	39				
116	294519	6874651	Granitic to granodioritic gneiss							
117	294531	6874815	Granitic to granodioritic gneiss							
118	294537	6874868	Granitic to granodioritic gneiss							
119	294588	6874983	Granitic to granodioritic gneiss							

120	294639	6875048	Granitic to granodioritic gneiss							
121	294714	6875131	Granitic to granodioritic gneiss							
122	294684	6879192	Granitic to granodioritic gneiss							
123	294569	6875110	Granitic to granodioritic gneiss							
124	294542	6874381	Granitic to granodioritic gneiss							
125	294802	6873904	Granitic to granodioritic gneiss		55	30				
126	294830	6873864	Granitic to granodioritic gneiss							
127	294881	6873813	Granitic to granodioritic gneiss							
129	297540	6875104	Garnet-bearing monzonitic gneiss							
132	297726	6875331	Granitic to granodioritic gneiss							
134	297655	6875252	Garnet-bearing monzonitic gneiss	Mylonitic shear zone			160	18		
136	296927	6874055	Metagabbro							
137	296932	6874061	Metagabbro							
138	296924	6874038	Metagabbro							
150	295549.5	6874106.3	Eclogite							
151	295587.6	6874380.6	Garnet-bearing monzonitic gneiss							
152	295595.5	6874424.4	Garnet-bearing monzonitic gneiss							
153	295603.7	6874456.9	Garnet-bearing monzonitic gneiss	With feldspar lense						
154	295591.7	6874591.2	Garnet-bearing monzonitic gneiss	With feldspar lense						
155	295675.9	6874573.9	Garnet-bearing monzonitic gneiss							
156	295757.5	6874833.8	Garnet-bearing monzonitic gneiss	With feldspar lense						
157	295808.5	6874888.2	Garnet-bearing monzonitic gneiss							
159	296015.1	6875036.2	Garnet-bearing monzonitic gneiss							
160	295938.8	6875499.1	Garnet-bearing monzonitic gneiss							
161	295558.1	6874212.6	Amphibiolite							
162	295542	6874004.3	Garnet- bearing monzonitic gneiss							
165	296736.5	6873742.5	Granitic to granodioritic gneiss							
166	296915.8	6874050.6	Boundary							
167	297117.7	6874399.7	Dioritic lense							

Appendix 3: Map of outcrops

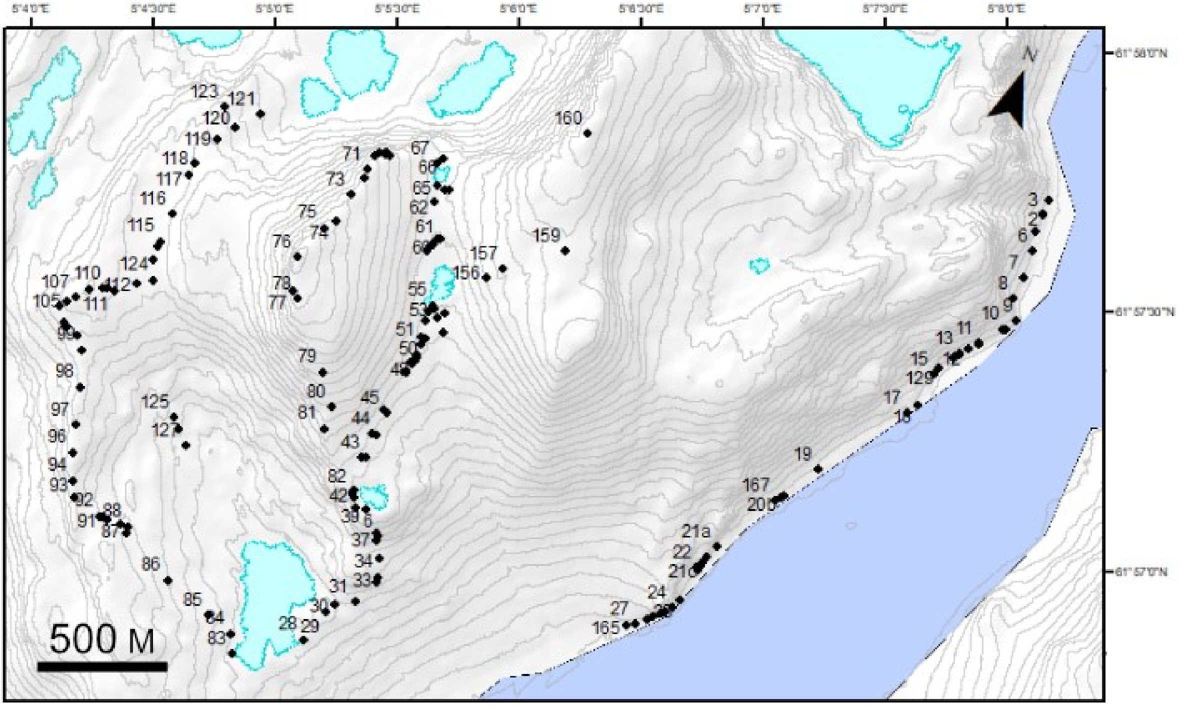

Appendix4: SEM EDS analysis

MLM37

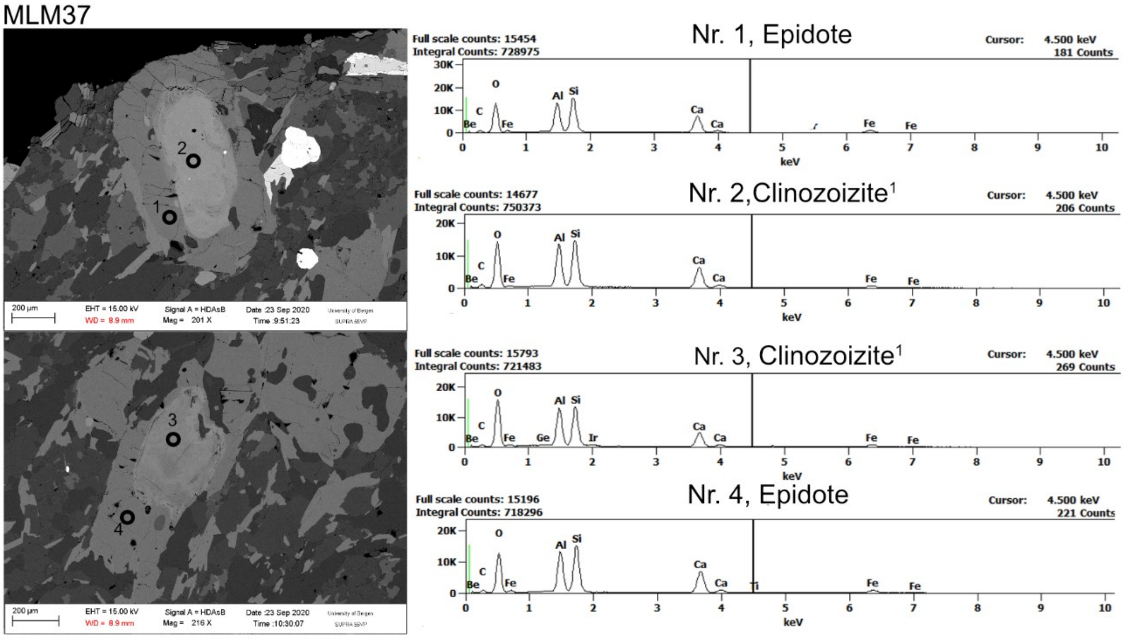

MLM138

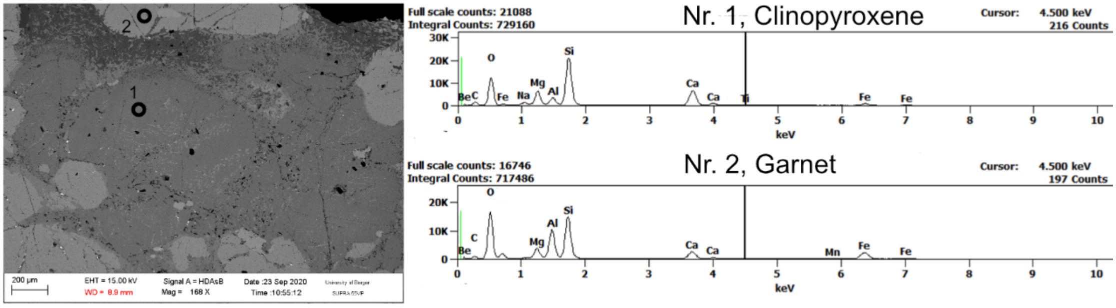

MLM59

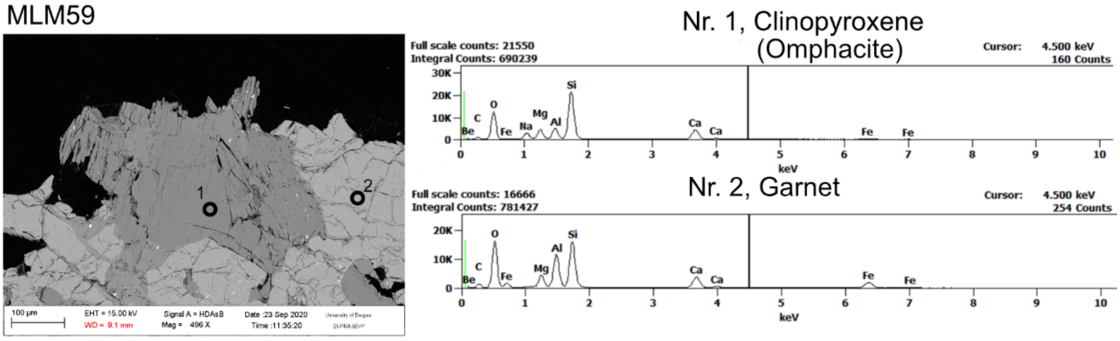

VAH48